UC Riverside
UC Riverside Electronic Theses and Dissertations

Title
An Investigation of Spin and Charge Transport in Doped and Defected Graphene

Permalink
https://escholarship.org/uc/item/63g0v03s

Author
McCreary, Kathleen M.

Publication Date
2012

Peer reviewed|Thesis/dissertation

eScholarship.org Powered by the California Digital Library
University of California

UNIVERSITY OF CALIFORNIA
RIVERSIDE

An Investigation of Spin and Charge Transport in Doped and Defected Graphene

A Dissertation submitted in partial satisfaction
of the requirements for the degree of

Doctor of Philosophy

in

Physics

by

Kathleen Michelle McCreary

March 2012

Dissertation Committee:
Dr. Roland K. Kawakami, Chairperson
Dr. Shan-Wen Tsai
Dr. Chun Ning (Jeanie) Lau

Copyright by
Kathleen Michelle McCreary
2012

The Dissertation of Kathleen Michelle McCreary is approved:

____

____

____
Committee Chairperson

University of California, Riverside

Acknowledgement

I would like to thank the many people who have helped me along the way. To my advisor, Dr. Roland Kawakami, your passion and energy is absolutely infectious and I have learned so much from you during my time at University of California, Riverside. Kyle Pi and Yan: you were great mentors and great friends. I miss walking into lab and hearing “Kathy!!” from Kyle every morning, and am so glad you are both doing well. Adrian, Jared, Jairo, Kyle, and Wei: We’ve had many lunches, dinners, and drinks together where we often end up talking about physics, no matter how hard we try not too. It’s been great working with you in lab, going through classes with you, and hanging out and relaxing outside of work. I’m so lucky that I have gotten to know you all and I’ll miss you guys terribly.

Matt, I’m so glad we went through this together. You made everything so much better. You listened to all my complaints and woes with sympathy and understanding, and in those extremely stressful times, you took care of everything else so I could focus on physics. Without you, at times I would have been a raggedy, malnourished graduate student, living in a pigsty.

Thank you mom, dad, Sandy, Jim, and grandma. You have always supported my decisions in life and I love you.

ABSTRACT OF THE DISSERTATION

An Investigation of Spin and Charge Transport in
Doped and Defected Graphene

by

Kathleen Michelle McCreary

Doctor of Philosophy, Graduate Program in Physics
University of California, Riverside, March 2012
Dr. Roland Kawakami, Chairperson

Graphene has proven to be an interesting and exciting material for experimental and theoretical researcher. The unique properties have motivated proposed applications including high frequency transistors, flexible touch screens, sensors, and spin logic gates, all of which will require integration of graphene with other materials. Additionally, exotic theoretical predictions involving magnetic phenomena in doped and defected graphene provide a new area of physics to explore. A central issue for both fundamental and applied physics involves understanding how charge and spin transport properties are affected by the presence of foreign materials or defects, a topic investigated here by intentionally introducing the graphene surface to transition metals, insulators, water, atomic hydrogen and lattice vacancies.

The first portion of this thesis provides the reader with a general introduction to graphene, the field of spintronics, device fabrication, measurement techniques, and sample characterization methods. Included are basic theoretical concepts of charge and

spin transport in graphene. Details of the unique ultra high vacuum system (UHV) that combines *in situ* variable temperature electrical measurement, molecular beam epitaxy, hydrogen doping, and sputtering capabilities are provided.

The second portion discusses experimental results. Firstly, all transition metals (Ti, Fe, Pt, Au) investigated result in *n-type* doping for sub monolayer coverage. This behavior provides evidence for the presence of a strong interfacial dipole. Secondly, metallic and insulating dopants are directly compared by *in situ* oxidation of Ti. Monitoring the charge transport properties throughout oxidation provides evidence of short range scattering due to insulating titanium dioxide impurities. Thirdly, the spatial distribution of impurities is found to strongly affect charge transport. Using a fixed amount of gold impurities, the formation of clusters from point like charged impurities reduces the electronic doping and scattering. Fourthly, in regards to spin transport in graphene, exposure to water is found to result in a substantial enhancement of spin signal, providing a simple method by which researchers can improve graphene spin valve device performance. Finally, spin scattering experiments provide direct evidence for the formation of paramagnetic moments in graphene exposed to atomic hydrogen or lattice vacancies, resolving a long standing controversy in the field.

Table of Contents

Chapter 1 Introduction to graphene……………..…………………………………....1

1.1 Carbon Materials…………………………………………………………...2

1.2 The existence of graphene……………………………………………………3

1.3 The graphene lattice………………………………………………………...5

Chapter 2 Charge transport in graphene……………......……….………………..…12

2.1 Introduction……………………………………………………………..13

2.2 The effect of contacts………………………………………………………..17

2.3 The effect of various substrates and dielectrics………………………………...20

2.4 The effect of adsorbates, dopants, and defects………………………...…….23

2.5 Magnetic phenomena in graphene……………………………………………30

Chapter 3 Spin transport in graphene………………………......…………………38

3.1 Local and non-local spin valve.......……………………………………………39

3.2 Hanle spin precession……………………………………………………..42

3.3 Spin transport in graphene……………………………………………………...43

Chapter 4 Device Fabrication and Measurement………….....……………………..53

4.1 Device Fabrication……………..……………………………………………..54

4.3 Ultra high vacuum system………………………………………………...60

4.3 Small MBE chamber…………………………………………………………63

4.3 Electrical measurements……………………………………………………..64

Chapter 5 Electronic Doping and Scattering by Transition Metals on Graphene ...66

5.1 Introduction………………………………………………………………67

5.2 Sample Description……………………………………………………………..68

5.3 Results…………………………………………………………………….69

5.4 Summary…………………………………………………………………..77

Chapter 6 Metallic and Insulating Adsorbates on Graphene ………………………81

6.1 Introduction……………………………………………………………….82

6.2 Sample Preparation………………………………………………………..83

6.3 Results…………………………………………………………………….83

6.4 Conclusion………………………………………………………………...89

Chapter 7 The Effect of Cluster Formation on Graphene Mobility………………...92

7.1 Introduction……………………………………………………………….93

7.2 Sample preparation………………………………………………………..94

7.3 Results…………………………………………………………………….94

7.4 Conclusion……………...………………………...………………………103

Chapter 8 Enhancement of Spin Injection into Graphene by Water Dipping …..107

8.1 Introduction………………………………………………...…………….108

8.2 Sample preparation………………………………………………………108

8.3 Conclusion……………………………………………………………….115

Chapter 9 Direct Detection of Magnetic Moment Formation in Graphene ...……119

9.1 Introduction…………………...………………………………………….120

9.2 Results…...……………………………………………………………….120

9.3 Conclusion……………………………………………………………….142

Appendix Tight binding approximation……………………………........……147

List of Figures

Fig 1-1 The graphene lattice……………………………………………………….….…....3

Fig 1-2 Optical image of graphene on Si/SiO_2..……………………………………...5

Fig 1-3 The formation of sp^2 orbitals...……….………………………………………...6

Fig 1-4 Constructing the graphene lattice in real and reciprocal space…...……………...7

Fig 1-5 Energy dispersion of graphene…………………………………………………..8

Fig 2-1 Charge transport measurements in graphene…………………………………...13

Fig 2-2 Disorder in graphene……………………………………………………………15

Fig 2-3 Minimum conductivity values in graphene……………………………………...19

Fig 2-4 Effect of metallic contacts on graphene transport………………………………19

Fig 2-5 Effect of various substrates and dielectric environments on graphene….………20

Fig 2-6 Effect of ice on graphene…….…………………………………………………22

Fig 2-7 Graphene on h-BN………………………………………………………………22

Fig 2-8 Graphene exposed to NO_2 gas……………………………………………….…24

Fig 2-9 Graphene exposed to potassium…………………………….…………………..25

Fig 2-10 Graphene with lattice vacancies……………………………………………….27

Fig 2-11 Graphene exposed to atomic hydrogen………………………………………..28

Fig 2-12 Universal Kondo behavior in graphene with lattice defects…………………..30

Fig 3-1 Lateral spin valve devices………………………………………………………39

Fig 3-2 Spin density……………………………………………………………………...40

Fig 3-3 First demonstration of spin transport in graphene………………………………43

Fig 3-4 Surface Chemical Doping of graphene…………………………………………45

Fig 3-5 Tunneling spin injection into graphene……………………………………………47

Fig 4-1 Alignment mark matrix written using electron beam lithography……..………57

Fig 4-2 Fabrication of transparent contact spin valves………………………………..58

Fig 4-3 Device structures…………………………………………………………...…59

Fig 4-4 Fabrication of tunnel barrier spin valves…………………………………...…60

Fig 4-5 Top view of the ultra high vacuum system…………………………………..61

Fig 4-6 Sample pocket and sample paddle……………………………………………63

Fig 4-7 Sample measurement in the small MBE chamber……………………………64

Fig 4-8 Schematic of electrical measurement…………………………………………65

Fig 5-1 Graphene doped with transition metal adsorbates…………………………....69

Fig 5-2 Dirac point shift vs coverage for nine separate samples……………………..70

Fig 5-3 Comparing conductivity, mobility, normalized mobility, and $-V_{D,shift}$ for graphene samples doped with Ti, Fe, and Pt……………………………………………..72

Fig 5-4 Pt-doped graphene at high coverage…………………………………………75

Fig 6-1 Ti-doped graphene……………………………………………………………84

Fig 6-2 Effect of cluster formation and oxygen exposure on Ti-doped graphene……….86

Fig 6-3 A comparison of the gate dependent conductivity curves…………………….87

Fig 6-4 The mobility and minimum conductivity, respectively, as a function of Dirac point voltage ………………………………………………………………...89

Fig 7-1 Graphene exposed to Au at 18 K……………………………………………95

Fig 7-2 Transport properties as a function of temperature……………………………98

Fig 7-3 The distribution of Au on graphene at room temperature…………...………100

Fig 8-1 Non-local spin transport in graphene……………………………………………..109

Fig 8-2 Spin transport following water exposure………………………………………111

Fig 8-3 Nonlocal magnetoresistance……………………………………………………112

Fig 8-4 Investigating the source of the observed magnetoresistance enhancement……114

Fig 9-1 The effect of hydrogen exposure on charge and spin transport in SLG………..122

Fig 9-2 Investigating the source of the dip measured in R_{NL}…..………………………..127

Fig 9-3 Test of nuclear spin effects……………………………………………………..129

Fig 9-4 Analysis of spin transport following atomic hydrogen exposure………………136

Fig 9-5 The effect of lattice vacancies on charge and spin transport in SLG at 15 K….141

Fig A-1 The graphene lattice in real space and in reciprocal space……………………147

Chapter 1: Introduction to Graphene

Abstract:

In this section, I introduce the reader to graphene- a recently discovered allotrope of carbon that has received immense attention from scientists among a wide variety of backgrounds. The methods used to produce and identify graphene are discussed, as well as several reasons why graphene is such a hot topic in the physics community.

1.1 Carbon Materials

While many people may not ponder the importance of carbon on a daily basis, life in the absence of this element is unimaginable. Carbon is present in the sun, stars, and the atmosphere of earth. It is the fifteenth most abundant element in the Earth's crust, and the fourth most abundant element in the universe. The wide variety of technologies and applications utilizing carbon, in the allotropic forms of graphite or diamond, are numerous and ever expanding. Graphite, one of the softest materials, is used as a lubricant for machinery, is an essential component for the manufacture of brake linings, and can also be mixed with clays to produce pencil "lead". On the other hand, diamond is the hardest known natural substance. Industrial grade diamonds are used to cut, grind, drill, and polish metals and stone while gem diamonds, treasured for their beauty, clarity, and durability, are often used in jewelry and are one of the most desired gemstones in the world.

In 2004 the two dimensional allotrope of carbon, referred to as graphene, was experimentally isolated by the Geim group at the University of Manchester (*1*). As shown below in Figure 1-1, graphene is composed of a single layer of carbon atoms arranged in a honeycomb lattice. The graphene lattice is the basic structure for several other allotropes of carbon and can be wrapped to form 0-D fullerenes, rolled into 1-D nanotubes, or stacked to produce 3-D graphite (*2*). Graphene adds to the wide variety of electronic properties exhibited among the allotropes of carbon. While diamond is an insulator and graphite a semiconductor, graphene is a semi-metal, with the valence and conduction bands touching at the Dirac points. The charge carriers behave as relativistic

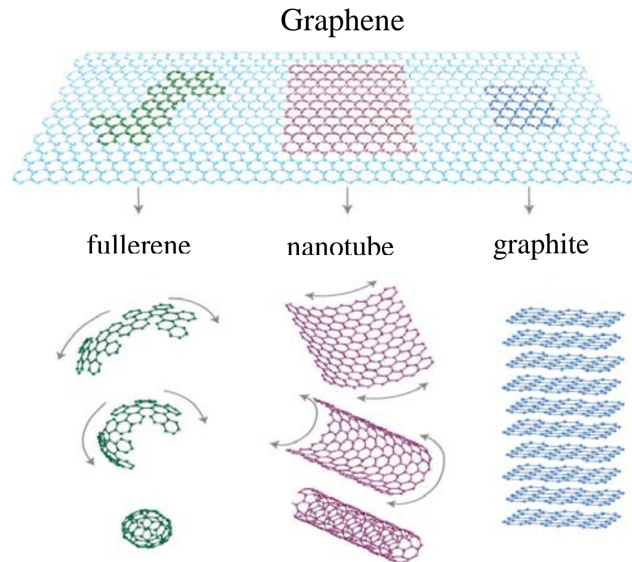

Fig 1-1 The graphene lattice. Graphene can be wrapped into fullerenes, rolled into nanotubes, and stacked into graphite**.** Image from reference (*2*).

massless dirac fermions (*3, 4*) as a result of the interaction between the graphene electrons and the periodic honeycomb lattice. The unique nature of the quasiparticles has interested both theorists and experimentalists. Furthermore, the excellent electronic properties (*5*), exceptional crystalline quality (*6*), high thermal conductivity (*7*), and flexibility (*8*) exhibited by graphene holds great potential for future applications and may make graphene an important contributor to the various carbon-based technologies used on a daily basis.

1.2 The existence of graphene

Prior to the discovery of graphene, many scientists were convinced that truly two dimensional materials could not exist. Theoretically, 2-D materials, such as graphene, were investigated to provide insight into the common 3-D bulk form, graphite (*9*), but it

was generally accepted that the thermodynamic instability would prevent the free-standing existence of such low-dimensional crystals (*10-12*). Furthermore, this idea was supported by numerous experimental observations, as the melting temperature of thin films decreased dramatically with decreasing thickness leading to the eventual separation of the film into islands at thicknesses below tens of atomic layers. At the time, atomic monolayers of material were known only to exist as a part of a larger 3-D structure, generally attained by epitaxial growth of the single layer on a substrate having matching crystal lattice (*13, 14*).

Through the process of mechanical exfoliation, a single layer of carbon was peeled away from bulk graphite and transferred to an Si/SiO_2 substrate, experimentally producing graphene and also proving the existence of 2-D materials. The Si/SiO_2 substrate is not necessary for the stability of graphene, as is can also be obtained on top of a wide variety of substrates (such as SiC (*15*), mica (*16*), BN (*17*), high-k dielectrics (*18-20*), and ferroelectrics (*21*) to name a few), in liquid suspension (*22*), and in the absence of a substrate as a suspended structure (*5, 6, 23*). Even though the SiO_2 substrate clearly isn't necessary, it was a key component in the discovery of graphene. When placed upon a ≈ 300 nm thick SiO_2 layer on Si, graphene becomes visible in an optical microscope due to optical interference (*2*), as seen below in Figure 1-2. Furthermore single layer graphene (SLG), bilayer graphene (BLG), or multilayer graphene (MLG) can be distinguished based on their subtle variations in contrast. The ease of identification has prompted many experimental research groups to rely heavily on Si/SiO_2 substrates.

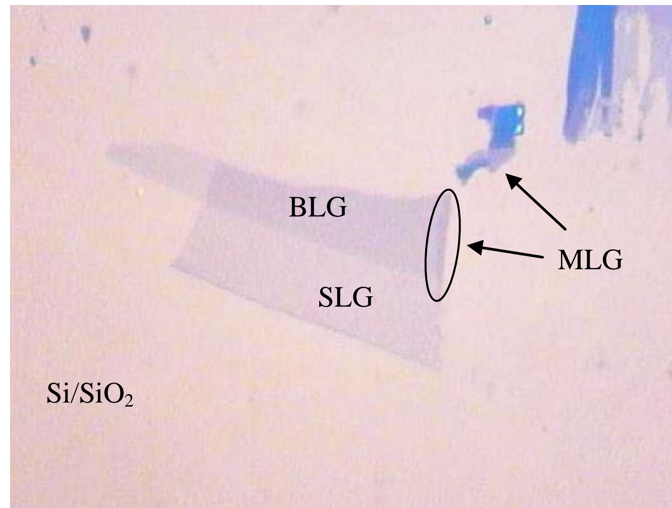

Fig 1-2 Optical image of graphene on Si/SiO$_2$. The single layer (SLG), bilayer (BLG), and multilayer graphene (MLG) is indicated to highlight the differences in contrast **.**

The mechanical exfoliation technique can also be used to produce two dimensional crystals of other materials. Simultaneously to the discovery of graphene, the Geim group was able to isolate single layers of boron nitride, MoS_2, $NbSe_2$, and $Bi_2Sr_2CaCu_2O_x$ (*24*). Thus far, graphene has received the most interest among the 2-D materials, namely due to the exceptional transport and unique nature of the charge carriers.

1.3 The graphene lattice

The honeycomb structure observed in graphene arises due to the hybridization of atomic orbitals. The p_x and p_y orbitals mix with a single *s* orbital resulting in 3 symmetric sp^2 orbitals as seen in Figure 1-3. The three sp^2 hybrids lie in the same plane and are separated by 120°, giving rise to the honeycomb shape. The overlap to neighboring sp^2 orbitals produces a σ band with filled electric shells, and will contribute little to electronic properties. The p_z orbital remains unchanged and is oriented at 90° to the plane

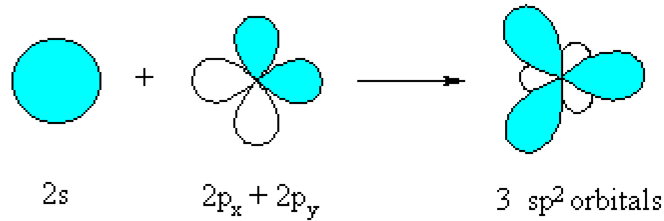

Fig 1-3 The formation of sp^2 orbitals. In graphene, the s, p_x, and p_y orbitals hybridize to form the sp^2 orbital. The p_z orbital remains unchanged

of the sp^2 hybrids. By covalently bonding to neighboring p_z orbitals, a half filled π band is formed, which dominates the electronic properties of graphene.

To investigate the electronic properties resulting from conduction in the π band, it is necessary to first examine the graphene lattice more closely. The honeycomb shape of the graphene lattice can be constructed from a triangular Bravais lattice having a basis of two carbon atoms, A and B as seen below in Figure 1-4. The lattice vectors are given by

$$\vec{a}_1 = \frac{a}{2}\left(3, \sqrt{3}\right) \quad \text{and} \quad \vec{a}_2 = \frac{a}{2}\left(3, -\sqrt{3}\right) \tag{1-1}$$

where a= 1.42 Å is the distance between two neighboring carbon atoms.

The symmetry of the graphene lattice results in a unique energy dispersion relation, which is derived using the tight-binding model (see appendix for more details). In this approach electrons are considered to be tightly bound to the atom to which they belong and have limited interaction with the surrounding atoms of the lattice. The resulting wave function is composed of a superposition of wave functions for isolated atoms located at each atomic site. Considering nearest-neighbor interactions accurately describes graphene's electronic properties and results in the dispersion relation

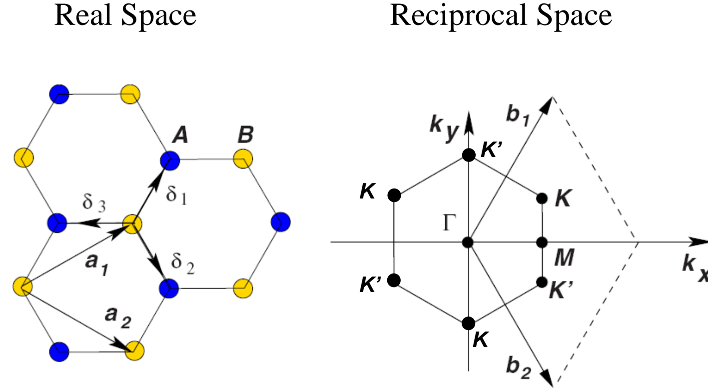

Fig 1-4 Constructing the graphene lattice in real and reciprocal space. The hexagonal structure in real space is described by a triangular bravais lattice with a basis of two carbon atoms (A and B). In reciprocal space the Dirac points (K and K') are positioned at the corners of the hexagonal Brilluoin zone.

$$E(\vec{k}) = \pm\hbar t\sqrt{3 + 2\cos\left(\sqrt{3}k_y a\right) + 4\cos\left(\frac{3}{2}k_x a\right)\cos\left(\frac{\sqrt{3}}{2}k_y a\right)} \qquad (1\text{-}2)$$

where $t \approx 2.8$ eV is the nearest neighbor hopping energy and + (-) signifies the energy of the conduction (valence) band. There are six points in reciprocal space where *E(k)* vanishes, indicating the conduction and valence bands meet. These points, labeled by *K* and *K'*, are referred to as the Dirac points and are positioned at the corners of the Brillouin zone. The dispersion relation can be expanded around the Dirac points to obtain

$$E(\vec{k}) = \hbar v_F \left|\vec{k}\right| \qquad (1\text{-}3)$$

where $v_F = \frac{3ta}{2} \cong 1\times 10^6$ m/s^2 and is referred to as the Fermi velocity and $\vec{k}$ now refers to the momentum measured relative to the Dirac point. The figure below shows the

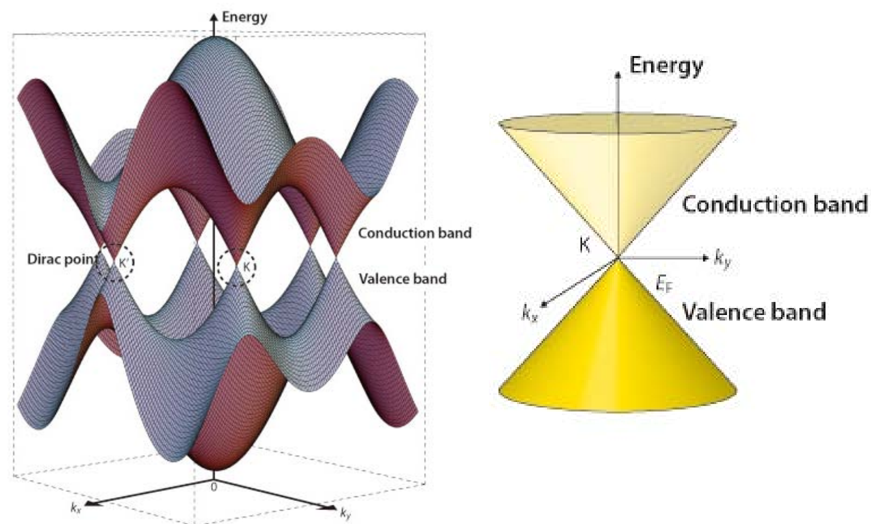

Fig 1-5 Energy dispersion of graphene

energy dispersion for the entire graphene lattice, zooming in on the linear energy dispersion near a Dirac point.

Notably, equation (1-3) does not depend on mass. The quasiparticles of graphene mimic relativistic, massless Dirac fermions. Many experimental investigations aim to uncover the consequences of the unique charge carriers present in graphene and thus far have reported phenomena such half integer quantum Hall (*25*), Klein tunneling (*26*), and minimum conductivity (*2, 27*).

References:

1. K. S. Novoselov *et al.*, Electrical field effect in atomically thin carbon films. *Science* **306**, 666 (2004).
2. A. K. Geim, K. S. Novoselov, The rise of graphene. *Nature Mater.* **6**, 183 (2007).
3. Y. Zhang, Y.-W. Tan, H. L. Stormer, P. Kim, Experimental observation of the quantum Hall effect and Berry's phase in graphene. *Nature* **438**, 201 (2005).
4. K. S. Novoselov *et al.*, Two-dimensional gas of massless Dirac fermions in graphene. *Nature* **438**, 197 (2005).
5. K. I. Bolotin *et al.*, Ultrahigh electron mobility in suspended graphene. *Solid State Comm.* **146**, 351 (2008).
6. J. C. Meyer *et al.*, The structure of suspended graphene sheets. *Nature* **446**, 60 (2007).
7. A. A. Balandin *et al.*, Superior thermal conductivity of single-layer graphene. *Nano Lett.* **8**, 902 (2008).
8. S. Bae *et al.*, Roll-to-roll production of 30-inch graphene films for transparent electrodes. *Nature Nanotech.* **5**, 574 (2010).
9. P. R. Wallace, The band theory of graphite. *Phys. Rev.* **71**, 622 (1947).
10. N. D. Mermin, Crystalline Order in Two Dimensions. *Phys. Rev.* **176**, 250 (1968).
11. L. D. Landau, Zur Theorie der phasenumwandlungen II. *Phys. Z. Sowjetunion* **11**, 26 (1937).
12. R. E. Peierls, Quelques proprietes typiques des corpses solides. *Ann. I. H. Poincare* **5**, 177 (1935).

13. J. A. Venables, G. D. T. Spiller, M. Hanbucken, Nucleation and growth of thin films. *Rep. Prog. Phys.* **47**, 399 (1984).

14. J. W. Evans, P. A. Thiel, M. C. Bartelt, Morphological evolution during epitaxial thin film growth: Formation of 2D islands and 3D mounds. *Sur. Sci. Rep.* **61**, 1 (2006).

15. C. Berger *et al.*, Ultrathin Epitaxial Graphite: 2D Electron Gas Properties and a Route toward Graphene-based Nanoelectronics. *J. Phys. Chem. B* **108**, 19912 (2004).

16. C. H. Lui, L. Liu, K. F. Mak, G. W. Flynn, T. F. Heinz, Ultraflat graphene. *Nature* **462**, 339 (2009).

17. C. R. Dean *et al.*, Boron nitride substrates for high-quality graphene electronics. *Nature Nanotech.* **5**, 722 (2010).

18. S. Seung Min, C. Byung Jin, Investigation of interaction between graphene and dielectrics. *Nanotechnology* **21**, 335706 (2010).

19. J. D. Caldwell *et al.*, Technique for the Dry Transfer of Epitaxial Graphene onto Arbitrary Substrates. *ACS Nano* **4**, 1108 (2010/02/23, 2010).

20. L. A. Ponomarenko *et al.*, Effect of a high-κ environment on charge carrier mobility in graphene. *Phys. Rev. Lett.* **102**, 206603 (2009).

21. X. Hong, A. Posadas, K. Zou, C. H. Ahn, J. Zhu, High-Mobility Few-Layer Graphene Field Effect Transistors Fabricated on Epitaxial Ferroelectric Gate Oxides. *Phys. Rev. Lett.* **102**, 136808 (2009).

22. S. Stankovich, Graphene-based composite materials. *Nature* **442**, 282 (2006).

23. W. Bao *et al.*, Controlled ripple texturing of suspended graphene and ultrathin graphite membranes. *Nature Nanotech.* **4**, 562 (2009).

24. K. S. Novoselov *et al.*, Two-dimensional atomic crystals. *PNAS* **102**, 10451 (2005).

25. Y. Zhang, J. W. Tan, H. L. Stormer, P. Kim, Experimental observation of the quantum Hall effect and Berry's phase in graphene. *Nature* **438**, 201 (2005).

26. S. N, B. Huard, D. Goldhaber-Gordon, Evidence for Klein tunneling in graphene p-n junctions. *Phys. Rev. Lett.* **102**, 026807 (2008).

27. Y.-W. Tan *et al.*, Measurement of scattering rate and minimum conductivity in graphene. *Phys. Rev. Lett.* **99**, 246803 (2007).

Chapter 2: Charge Transport in Graphene

Abstract

A direct result of being composed of a single atomic layer is that all electronic conduction takes place at the surface of graphene. For this reason, the charge transport properties such as mobility, Dirac point, and minimum conductivity are expected to be sensitive to the surrounding environment (including such factors as contacting metallic electrodes, dopants/defects present on the graphene surface, and the underlying substrate supporting the graphene). Numerous theoretical and experimental works have investigated the dependence of charge transport on such environmental factors and have also demonstrated graphene's properties can be tailored through intentional doping with adsorbates or lattice defects, and will be discussed in this chapter. The ability to control graphene's properties has motivated investigations in exotic new directions such as magnetic moment formation (*1-9*), gate tunable magnetism (*10*), the Kondo effect (*8, 11-13*), and superconductivity (*14*) in graphene.

2.1 Introduction

Typically, to investigate transport properties in graphene, a field-effect transistor type device is fabricated (Fig 2-1A). The graphene is placed on a SiO_2/Si substrate and is electrically contacted to probe transport properties by applying current (I) and measuring the resulting voltage (V). A gate voltage (V_g) applied between Si and graphene allows for the carrier concentration, n, to be tuned from electrons to holes. Modeling the graphene device as an ideal capacitor, the carrier concentration away from the Dirac point (V_D) is determined to be $n(V_g) = \frac{\varepsilon_0 \varepsilon (V_g - V_D)}{te}$, where $\varepsilon_0 = 8.854 \times 10^{-12}$ F/m is the permittivity of free space, ε is the dielectric constant (3.9 for SiO_2), t is the thickness of the dielectric, e is the charge of an electron, and V_D indicates the minimum carrier concentration and occurs at the maximum resistance in ρ (in Fig 2-1B V_D=0 V). This

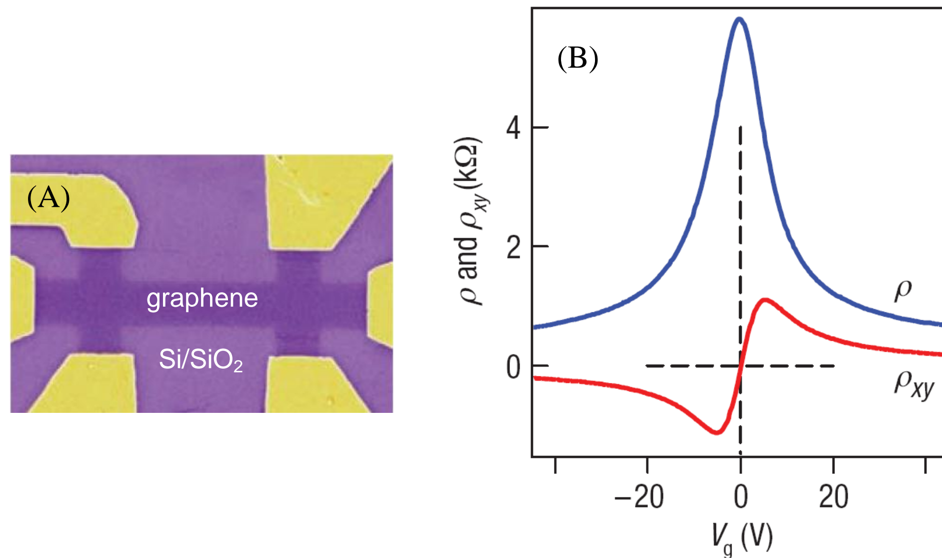

Fig 2-1 Charge transport measurements in graphene. (A) An optical image of a FET-type graphene device fabricated on a Si/SiO_2 substrate. (B) Typical scans of gate dependent longitudinal resistivity (ρ) and Hall resistivitivity (ρ_{xy}). Optical image and data are from Ref. (15).

simplifies to $n(V_G) \approx -7.2\times10^{10}(V_g - V_D)$ cm^{-2} for graphene on 300 nm SiO_2.

Representative scans of the gate dependent longitudinal resistivity (ρ) and Hall resistivity (ρ_{xy}) for a pristine graphene sample at room temperature (measured in ref (*15*)) are displayed in Figure 2-1B. Away from V_D and in a perpendicular magnetic field, $\rho_{xy} \propto \frac{1}{n}$, as expected for a single type of charge carrier (electrons or holes). On the other hand, near V_D both electrons and holes contribute to conduction (as will be discussed in more detail later) making $\rho_{xy} \propto \frac{n_e - n_h}{n_e + n_h}$, where n_e (n_h) is the electron (hole) concentration. While at first glance, the ρ and ρ_{xy} curves may appear rather unimpressive, there is much physics to be investigated in these basic charge transport measurements. Theoretically, the density of states in graphene is given by $\nu(\varepsilon) = \frac{g_s g_v 2\pi|\varepsilon|}{h^2 v_F{}^2}$, where $\nu_F=10^6$ m/s^2 is the Fermi velocity, g_s=2 is the spin degeneracy, and g_v=2 is the valley degeneracy. Naively following this relation, ν is expected to vanish at the Dirac point, where $\varepsilon = 0$, and would lead to a conductivity (resistivity) equal to zero (infinity). As demonstrated in gate dependent ρ (Fig 2-1B) as well as the first measurements of charge transport in graphene (*16*), the measured conductivity exhibits a finite value at V_D. The discrepancy has motivated theoretical and experimental investigations focusing on the minimum conductivity (σ_{min}) and has lead to a better understanding of charge transport near the Dirac point.

As with any physical system, the charge carriers in graphene are affected by disorder. Possible sources for disorder in graphene systems vary widely and could include charged impurities in the form of surface adsorbates or trapped charge in the supporting substrate, neutrally charged impurities, ripples, carbon vacancies, edges, topological Stone-Wales defects, and lattice strain, to name a few. The presence of disorder results in an inhomogeneous distribution of conducting electron and hole puddles at low carrier concentrations. While early investigations debated which type of disorder was most responsible for the formation of electron hole-puddles, it is now clear they are due to the presence of charged impurities. The presence of these electron-hole puddles leads to a residual carrier density, n^*, on the order of 10^{11} cm^{-2} for graphene on SiO_2 and prevents

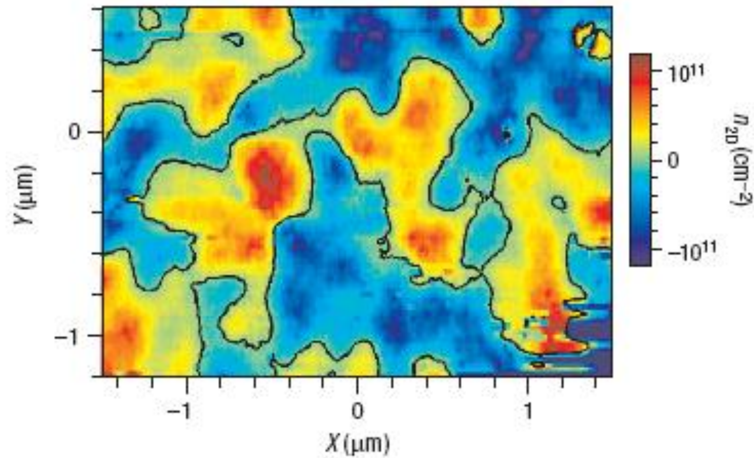

Fig 2-2 Disorder in graphene. Using a scanning single electron transistor the spatial density fluctuations in graphene are measured. The black line shows the contour between electron (red) and hole (blue) puddles at an average carrier density of zero. Image is from Ref. *(17)*.

truly probing Dirac point physics, where carrier concentration vanishes. The density fluctuations (electron-hole puddles) have been experimentally measured by Martin *et al* *(17)* using a scanning single electron transistor, as seen above in Figure 2-2. Even at an

average carrier density of zero (Dirac point) electronic conduction occurs locally through sections having electron and hole concentrations, represented by the blue and red regions respectively in Figure 2-2. These puddles qualitatively explain the presence of the observed minimum conductivity and indicate that the physics near the Dirac point is different than the physics at higher carrier densities.

Several theoretical works have investigated the behavior of massless dirac fermions (*18-21*), with many predicting a universal minimum conductivity value of $4e^2/\pi h$. Yet, experimental works performed by Geim *et al (22)* have reported σ_{min}~$4e^2/h$ (Fig 2-3A), and further studies completed by Tan *et al (23)* found a non-universal σ_{min} generally greater than $4e^2/h$ (Fig 2-3B). Investigations by Miao *et al* (*24*) focused on resolving the issue of the missing π between theoretical predictions and experimental values, and demonstrated that $4e^2/\pi h$ is accessible in the ballistic transport regime for samples where length is much shorter than width (Fig 2-3C). While the three experimental works discussed here *(22-24)* demonstrate a wide variety of measured values for σ_{min} a common feature in pristine graphene devices is a $\sigma_{min} \geq 4e^2/\pi h$.

Away from the Dirac point, disorder also plays a role in the measured transport properties through the mobility μ and gate dependent conductivity. The $\mu = \frac{\sigma}{ne}$ relates to the scattering of charge carriers and is an indication of the quality of electronic transport. While graphene devices supported by Si/SiO_2 have exhibited impressive μ~20,000 cm^2/Vs, it is still dramatically less than the predicted intrinsic limit of $\sim 2 \times 10^5$ cm^2/Vs (*25*). The large disparity is an indication of extrinsic sources of electronic scattering.

Additionally, the particular shape of gate dependent conductivity curve is governed by disorder in graphene. Experimental measurements show a roughly linear dependence between σ and n near the Dirac point, gradually becoming sublinear at higher carrier concentrations. In Boltzmann theory, the conductivity is related to the scattering time, τ, of charge carriers by $\sigma = \left(e^2/h\right)\left(2E_F\tau/\hbar\right)$(*26, 27*), where E_F is the Fermi energy. The various sources of disorder are associated with different scattering times, but all will contribute to the total τ of the charge carriers in graphene. Theoretical works have found that for long range charged impurities $\tau_c \propto \sqrt{n}$ and dominates at low n, while for short range impurities $\tau_s \propto \frac{1}{\sqrt{n}}$ and dominates at high concentrations. As $E_F \propto \sqrt{n}$, the conductivity is expected to be proportional to n for the case of charged impurities and independent of n for short range impurities. The experimentally observed sublinearity of σ at high carrier concentrations can be attributed to the competition between long and short range scatterers (*26, 27*). Other investigations find that scattering from ripples (*15, 28*) or resonant scatterers (*29*) can also produce conductivity proportional to n at low carrier concentration, and have suggested that ripples or resonant scattering may be the source of disorder limiting μ and defining the shape of σ. This has lead to a dichotomy in the field - those who believe the dominant scattering mechanism limiting μ is charged impurities and those who do not, and will be discussed further in the following sections.

2.2 The effect of contacts

As mentioned in the previous sections, transport properties are generally investigated by fabricating FET-type devices having metal electrodes in contact with the graphene

surface. It has been found that these electrodes can impact the measured transport properties. In the work performed by Huard *et al (30)* the properties of devices fabricated with invasive probes (extending across the full graphene strip width) were compared to external probes (connected to narrow graphene arms on the side of the strip) as seen in Figure 2-4A . The invasive probes (a,b,c,d,e, in Fig 2-4A) were found to pin the charge density in the graphene below the metal, creating a density step along the graphene strip, resulting in p-n, p-p, or n-n junctions close to the electrodes (depending on metal used and gate voltage applied to graphene). Also, a more pronounced sublinearity in σ vs. V_g was observed for samples with invasive probes and was attributed to the pinned charge density near electrodes, as opposed to short range scattering. The measured transport properties may also be sensitive to the type of contact material used. Devices having invasive Co contacts exhibit anomalous transport characteristics in gate dependent σ such as shoulders or plateaus due to band alterations of the graphene, but such anomalies are not observed for Cr/Au contacts (*31*). The charge transfer between graphene and metallic contacts has been imaged using a photocurrent microscopy technique, where the contact doping is found to extend into the graphene channel up to 0.5 μm (*32-34*), as shown in Figure 2-4B. The interactions at the graphene/electrode interface can also lead to interesting and important effects in the metal contact itself. Contrary to the general assumption that the contact resistivity ρ_c is constant and relatively small, Blake *et al* (*35*) demonstrated ρ_c is strongly gate dependent and can even become effectively negative near V_D due to doping induced by metal contacts in adjacent graphene regions, as seen in

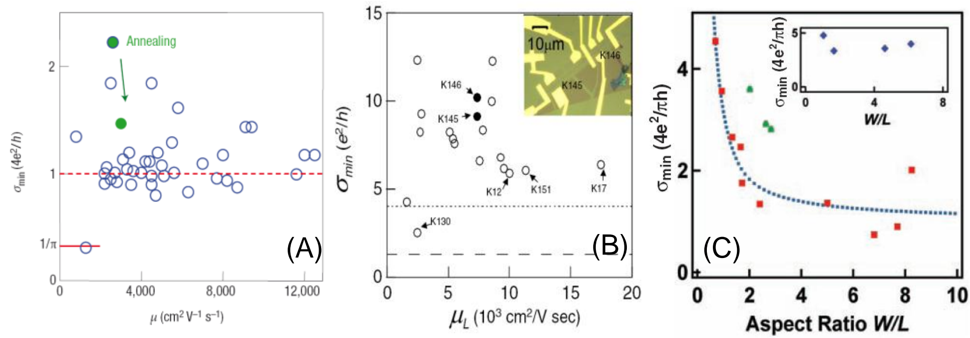

Fig 2-3 Minimum conductivity values in graphene. (A) Experimental results from Geim *et al (22)* suggesting a universal σ_{min}~$4e^2$/h. (B) Experimental results from Tan *et al (23)* suggesting a non-universal minimum conductivity value. Both experiments are at odds with theoretical predictions of σ_{min}~$4e^2/\pi h$. (C) Experimental results from Miao *et al (24)* demonstrate σ_{min}~$4e^2/\pi h$ can be reached in the ballistic limit.

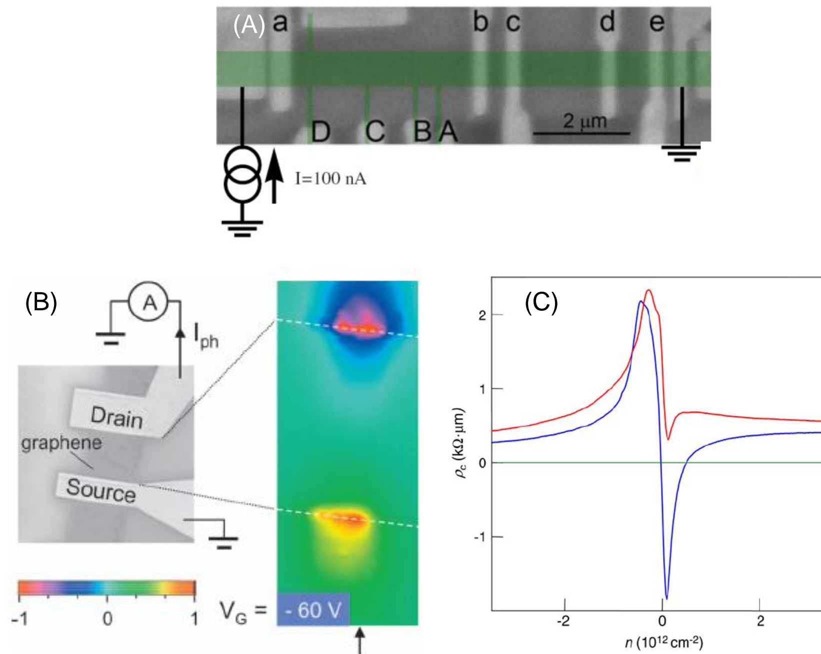

Fig 2-4 Effect of metallic contacts on graphene transport. (A) Image of graphene device used to investigate invasive (a,b,c,d,e) and external (A,B,C,D) probes from Ref. (*30*). (B) Photocurrent study showing the effect of electrodes on the graphene device from Ref. (*32*). (C) Measurements of the contact resistance from Ref. (*35*).

Figure 2-4C. As a result, two-probe measurements may be undervaluing σ_{min}. While the use of contacting electrodes can not be avoiding in transport studies, it is important to keep in mind the possible impacts they may have on measured properties.

2.3 The effect of various substrates and dielectrics

Commonly, Si/SiO_2 wafers are chosen as the supporting substrate for graphene, mainly out of convenience. Isolated graphene can be easily identified with an optical microscope due to differences in contrast related to the thickness of the SiO_2 layer. Also, Si/SiO_2 wafers are commercially available, provide gating capabilities, can be cleaved into the desired dimensions, and are also relatively inexpensive. Unfortunately, SiO_2 also exhibits large surface corrugations, contains trapped charges at the surface, and has a relatively low dielectric constant which may adversely affect graphene transport. These issues have motivated investigations into alternative substrates.

To investigate the importance of scattering from charged impurities located in the SiO_2 substrate, transport on several different substrates was compared in the work by

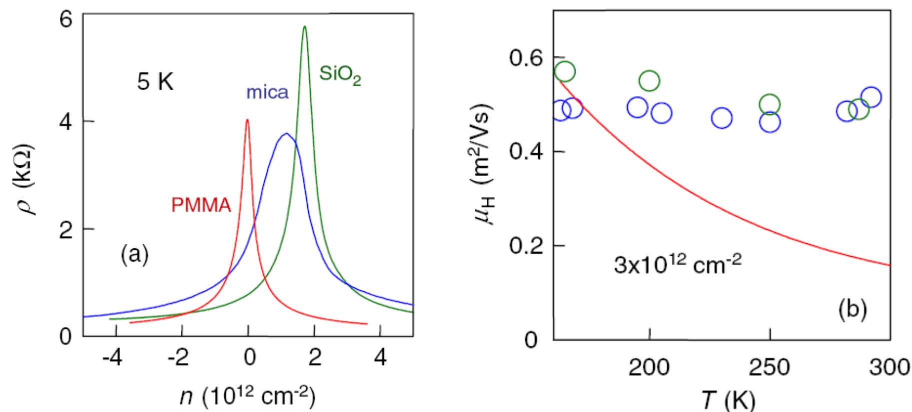

Fig 2-5 Effect of various substrates and dielectric environments on graphene. (A) Comparisons of various substrates result in similar μ values (B) Graphene in an ethanol. While the dielectric constant increases from ~25 to 55 with decreasing temperature, the μ (symbols) exhibits minimal change. The red line shows what is expected for coulomb scattering. Images are from Ref. *(36).*

Ponomarenko *et al* (*36*). The mobilities on mica, SiO_2, and PMMA were measured to be μ=2500, 4500, and 8000 cm^2/Vs respectively, as seen in Figure 2-5A. The similar μ values exhibited for the different substrates (which consequently have different amounts of charged impurities) suggest the low μ reported for graphene on SiO_2 is **not** due to charged impurities in the substrate, as often speculated. Additionally, Ponomarenko *et al*, investigated the importance of scattering from charged impurities on the *surface* of graphene. The device was coated in ethanol, whose dielectric constant κ increases from 25 to 55 with decreasing temperature. For the case where charged impurity scattering is dominant, the dielectric environment is expected to play an important role, providing increased screening from impurities for higher dielectric constants, consequently increasing μ. As shown in Fig 2-5B the μ of graphene in ethanol is independent of temperature (κ), suggesting charged impurity scatterers are not the impurities that limit μ.

Separate *in situ* studies involving the affects of varying the dielectric environment has produced contradictory results. Jang *et al (37)* modified the dielectric environment by depositing ice layers on the surface of graphene. The presence of ice layers increases κ from 1 (air) to ~3.2 (ice) and directly results in the enhancement of the mobility from 9000 to 12000 cm^2/Vs, as seen in Figure 2-6A and B due to the decreased interaction between charged impurities and carriers in the graphene layer.

Efforts to improve mobility in graphene by employing alternate substrates or coating graphene with high-k dielectrics have generally resulted in small (if any) enhancements. The most dramatic affect on transport properties has been achieved by placing graphene on hexagonal boron nitride crystals. Mechanical exfoliation techniques are used to obtain

high quality h-BN crystals on Si/SiO_2 wafers. Graphene is then position on top of the h-BN. Transport measurements of graphene on (h-BN) have exhibited extremely high mobilities of at least μ=60,000 cm^2/Vs (*38*) (Figure 2-7A). Mobility can be even further

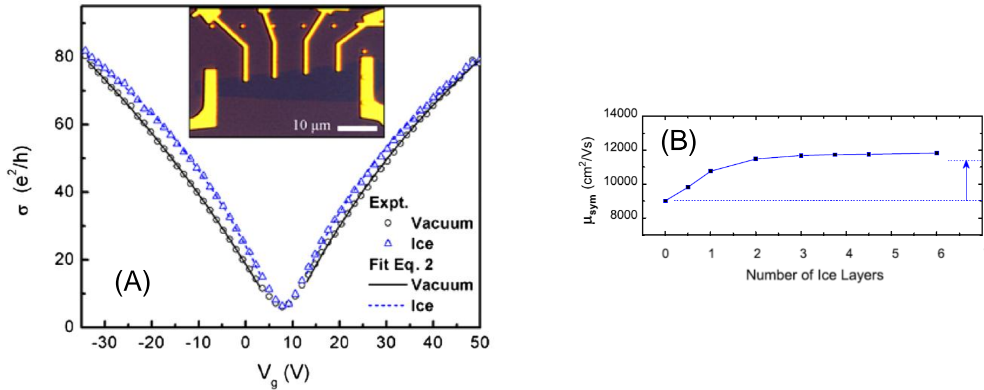

Fig 2-6 Effect of ice on graphene. (A) Gate dependent σ before and after deposition of ice. (B) Enhanced mobility due to the higher dielectric. Images are from Ref. *(37).*

increased to μ=120,000 cm^2/Vs (*39*) when sandwiched between two h-BN crystals. The improved transport is attributed to the excellent quality of the h-BN substrate. Like graphene, h-BN exhibits a honeycomb lattice structure, with boron and nitrogen

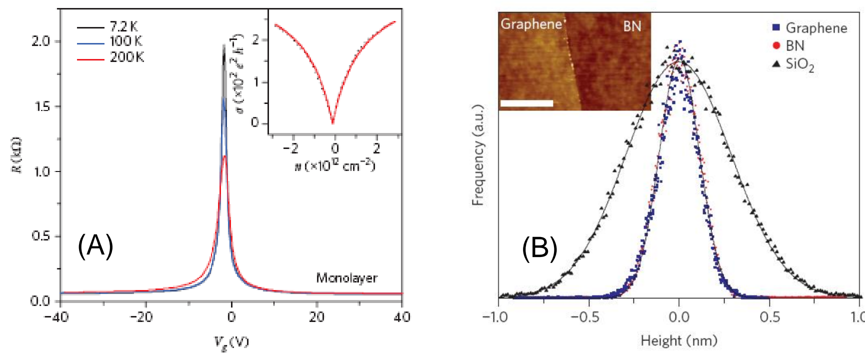

Fig 2-7 Graphene on h-BN. (A) Gate dependent ρ for graphene on h-BN at various temperatures. Inset: corresponding σ vs. $V_{g.}$ (B) Height distribution measured by AFM for SiO_2, h-BN and graphene on h-BN. Images are from Ref. *(38).*

alternating in the hexagonal ring. The different on-site energies of the boron and nitrogen atoms result in a large (5.97 eV) bandgap and a small (1.7%) lattice mismatch with graphite. Strong, in-plane, ionic bonding, is expected to prevent dangling bonds or surface charge traps and result in an atomically flat, chemically inert material. Transport measurements comparing graphene on h-BN and graphene on Si/SiO_2 exhibit a threefold decrease in the scattering rate due to charged impurities, providing strong evidence that charged impurities are the mechanism limiting μ in graphene supported by SiO_2. Additionally, the strong temperature dependence of σ_{min} indicates the disorder induced residual carrier density $n*$ (electron-hole puddles) are significantly reduced to 10^9 cm^{-2}. The σ_{min} is expected to vary with temperature for $k_B T > \hbar v_F \sqrt{\pi n*}$, and is not observed in SiO_2 supported graphene due to the large $n*$~10^{11} cm^{-2}.

2.4 The effect of adsorbates, dopants, and defects

The works highlighted in sections 2.2 and 2.3 have demonstrated the sensitivity of graphene to the surrounding environment as well as providing much insight into the graphene transport. Further information can be gained by the intentional doping of the graphene with adsorbates, dopants, and defects.

2.4.1 Graphene exposed to gaseous adsorbates

The experimental work performed by Schedin *et al* (*15*) has demonstrated the extreme sensitivity of graphene to gaseous adsorbates on the surface (*15*). Measurements of ρ_{xy} performed in a perpendicular magnetic field of 10 T near the Dirac point show discreet jumps during adsorption (blue) or desorption (red) of NO_2 (Figure 2-8A), with the observed values corresponding to the changes in ρ_{xy} caused by adding or removing

one electron charge. The demonstrated ability to detect individual events when a gas molecule attach to or detach from the surface suggests graphene may be a promising candidate for gas sensing applications. Additionally, easily detectable changes occur in ρ following the exposure of graphene to NO_2 (Figure 2-8B). The parallel shift to the right in

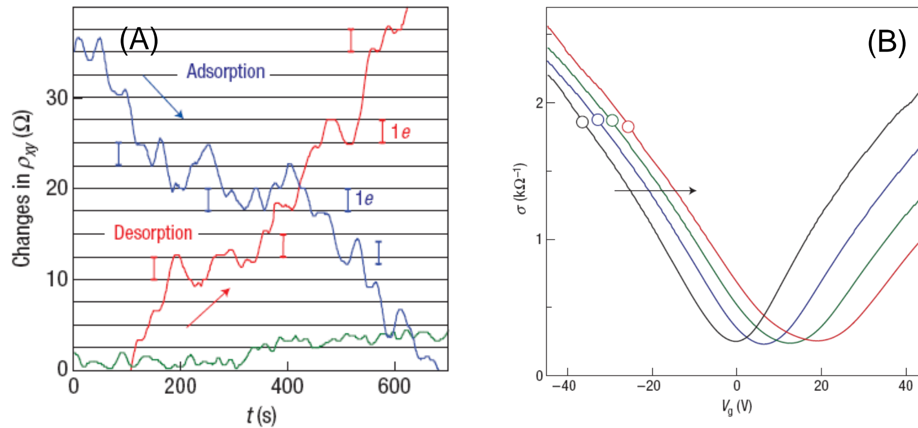

Fig 2-8 Graphene exposed to NO_2 gas. (A) Changes in ρ_{xy} near V_D caused by adsorption and desorption of individual gas molecules. The green curve serves as a control: the same device thoroughly exposed to pure. The grid lines correspond to changes in ρ_{xy} caused by adding one electron charge. (B) The effect of NO_2 on ρ. Images are from Ref. *(15)*.

conductivity curves signifies NO_2 transfers holes to the graphene. The transfer of holes results in charged impurity sites on the graphene surface. Interestingly the mobility $\mu = \frac{\sigma}{ne}$, determined from steepness of the gate dependent conductivity curves away from V_D, remains nearly constant with NO_2 doping. As μ is a measure of the scattering rate of charge carriers, this indicates the additional charged impurities resulting from NO_2 do not scatter the charged carriers, and suggests charged impurity scattering is *not* the scattering mechanism limiting mobility in graphene.

2.4.2 Graphene exposed to Potassium

Chen *et al (40)* performed similar transport experiments on graphene intentionally doped with potassium, yet arrived at very different conclusions. As seen in Figure 2-9A, upon exposure to K adsorbates, several important effects were noted. The Dirac point shifts to negative voltages. Potassium acts as a donor, transferring electrons to graphene,

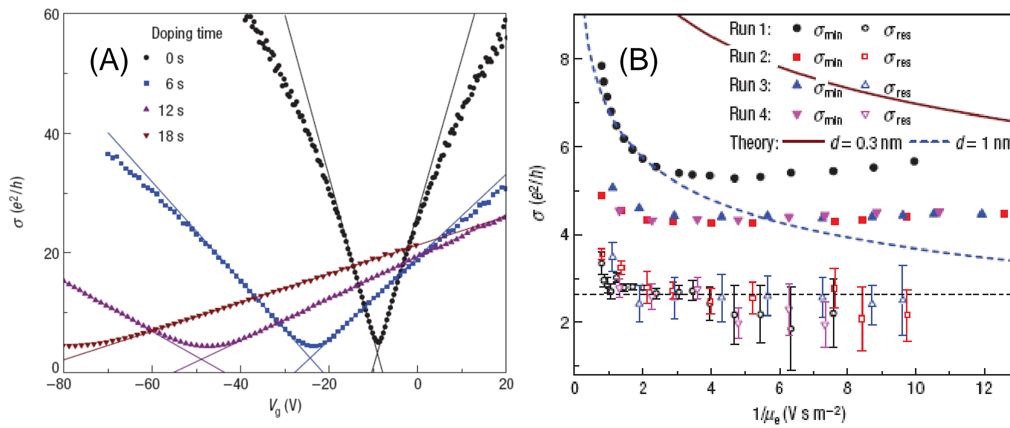

Fig 2-9 Graphene exposed to potassium. (A) Exposure to K results in *n-type* doping of graphene and decreased mobility due to charged impurity scattering. (B) σ_{min} decreases with increasing K concentration, saturating $\geq 4e^2/h$. Images are from Ref. *(41)*.

resulting in charged impurities at the surface. The mobility decreases with increasing potassium coverage (charged impurities). (Chen *et al* suggest that the mobility independent of charged impurity concentration observed in (*15*) may be due to the limited voltage scan range, poorly controlled environment, or sample contamination). In this work mobility and charged impurity concentration (n_{imp}) are found to be inversely proportional, with $\mu = \dfrac{5\times10^{15}\ \mathrm{V^{-1}\,s^{-1}}}{n_{imp}}$. Furthermore, comparing the impurity

concentration to Dirac point shift, ΔV_D, it is determined $\Delta V_D \propto \left(\frac{1}{\mu}\right)^b$ where b=1.2-1.3, as expected theoretically for point-like charged impurities. $\sigma(V_g)$ becomes more linear with increasing potassium exposure. As discussed previously, the dependence of the conductivity on carrier density is expected to be $\sigma \propto n^a$ with $a = 1$ for long range charged impurities and $a < 1$ for short-range scattering, with the competition between the scattering mechanisms resulting in the sublinearity at high carrier concentrations. Increasing the charged impurity concentration causes the transition from long range to short range scattering to move further away from the Dirac point yielding more linear conductivity curves with additional K coverage, as seen in Fig 2-9A. The minimum conductivity does not exhibit a universal value, instead it exhibits a dependence on sample doping, decreasing with increasing charged impurities and plateauing at $\sigma_{min} \geq \frac{4e^2}{h}$. The above properties are consistent with theoretical investigations of scattering from charged impurities (*26, 41*). In the proposed model, charged impurities either in the substrate or in the vicinity of graphene create a spatially inhomogeneous potential distribution in the graphene plane. At low carrier density, the spatially inhomogeneous potential breaks the system up into puddles of electrons and holes, inducing a residual density n^* that in turn changes the screening of charged impurities. The n^* and n_{imp} govern the Dirac point voltage, width of the plateau, and σ_{min} as well as the measured μ. While there are a few who disagree, is it generally accepted that charged impurities are the scattering mechanism limiting mobility in Si/SiO_2 supported graphene.

2.4.3 Resonant scattering in graphene

The introduction of defects or dopants such as lattice vacancies (*8, 42, 43*), atomic hydrogen (*44, 45*), fluorine (*9*), or ozone (*46*) have been found to dramatically impact charge transport. These strongly bound adsorbates are expected to generate midgap states with an energy level ε very close to the Dirac point, resulting in resonant scattering. Interestingly, as displayed in Fig 2-10A, upon the introduction of lattice vacancies via

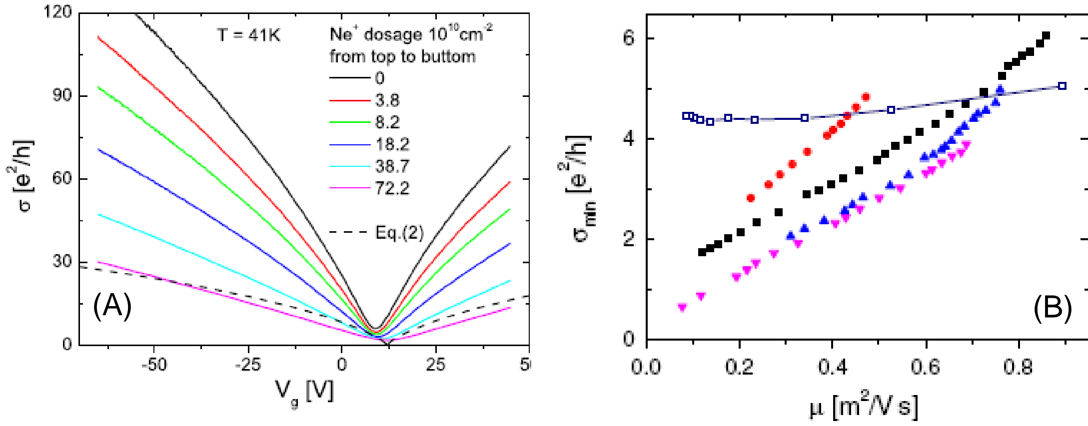

Fig 2-10 Graphene with lattice vacancies. (A) Gate dependent σ for various Ne^+ dosages. (B) The σ_{min} as a function of μ for separate samples following irradiation. The σ_{min} of graphene following K^+ doping is shown for comparison (open symbol). Images are from Ref. *(42).*

Ne^+ sputtering, the characteristic v-shape of σ vs. n observed in pristine graphene is maintained, while μ is reduced (*42*). The atomic-scale defects result in a large scattering cross section when E_F is close to the defect energy level ε, occurring near V_D. Away from V_D the scattering rate decays relatively slowly, resulting in $\sigma \propto n$. In particular, the conductivity is modeled to be $\sigma(n) = ne\mu = \frac{2e^2}{\pi h}\frac{n}{n_d}\ln(k_F R)$ where n_d is the defect density, k_F= is the Fermi wave vector, and R is the radius of the potential well, producing

roughly constant μ for atomic scale potential, *R.* Resonant scattering also impacts the measured σ_{min}. Whereas experimentally, pristine graphene or graphene subject to charged impurities exhibits $\sigma_{\min} \geq \frac{4e^2}{h}$ for typical device geometries, and above $\frac{4e^2}{\pi h}$ in the ballistic limit, samples exposed to resonant scatterers result in a σ_{min} below both these value as seen in Figure 2-10B. The dip below $\frac{4e^2}{\pi h}$ is an indication of inter-valley

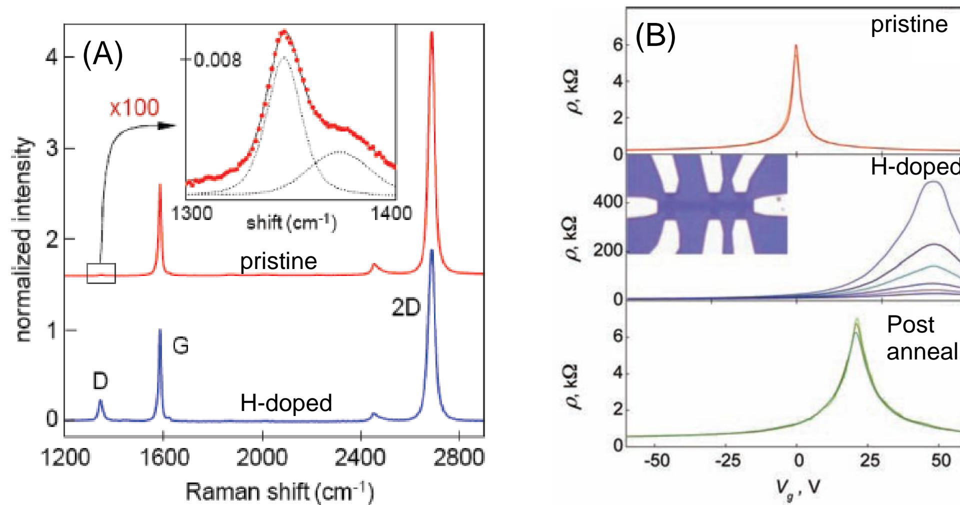

Fig 2-11 Graphene exposed to atomic hydrogen. (A) Raman spectra for pristine (red) and atomic hydrogen-doped (blue) graphene from Ref. (*29*). (B) Temperature dependence for pristine, H-doped, and post annealed graphene devices from Ref. *(44)*.

scattering and is detected as a defect peak in the Raman spectra. Recent work by Ni *et al* (*29*) investigating graphene exposed to atomic hydrogen demonstrates that, although previously unnoticed due to noise levels in Raman measurements, a defect peak (D) is universally present in pristine graphene devices (Fig 2-11A). The magnitude of the D peak intensity corresponds to a resonant scattering concentration which would limit μ to ~20,000 cm^2/Vs, and Ni *et al* suggest that resonant scattering may be the dominant

mechanism in pristine graphene devices, rather than charged impurities. Although, in light of other experimental results, this is an unlikely scenario. In particular, a single graphene flake spanning h-BN and SiO_2 exhibits enhanced μ in the region supported by h-BN. Presumably the graphene exhibits the same concentration of resonant scattering sites throughout, indicating resonant scattering is not the dominant mechanism. Additionally, exposing graphene to atomic hydrogen (*44*) or other resonant scatterers (*9, 46*) change the observed electronic behavior as seen in Figure 2-11B. Pristine graphene samples exhibit very weak temperature dependence of resistivity, being slightly metallic at the V_D and decreasing in ρ with decreasing temperature. Following H-exposure, the device exhibits insulating behavior, with ρ increasing by 2 orders of magnitude as the temperature decreases from 300 K to 4 K. The initial weakly temperature dependent metallic behavior is recovered after annealing the sample to desorb atomic hydrogen.

As highlighted in the studies above, investigations of doped and defected graphene has lead to better understanding of charge transport in graphene. Yet, there still remains much to be learned. We have contributed to this interesting field in several ways, which will be discussed in later chapters. Electronic doping and scattering resulting from transition metals having different work functions is presented in Chapter 5. In chapter 6, we directly compare the effects of metallic and insulating adsorbates, and in chapter 7 investigate how the spatial distribution of impurities (point like impurities vs. clusters) can impact the charge transport.

2.5 Magnetic Phenomena in graphene

The information obtained from investigations of pristine as well as doped/defected graphene provides a foundation for studies of magnetic phenomena in graphene. While pristine graphene is not expected be magnetic, there are several instances where introducing non-magnetic adsorbates or defects to the graphene lattice may result in magnetic moment formation. Employing the Anderson impurity model and modifying for graphene, Uchoa *et al* (*10, 47*) find that transition metal adatoms on graphene can develop a local magnetic moment due to anomalous broadening of the adatom local electronic states. Additionally, the application of a gate voltage can control the magnetic properties of the adatoms, and would allow for the identification of local moments through ordinary transport measurements.

The possibility of magnetic moment formation in graphene due to single carbon atom defects or atomic hydrogen adsorption has been under considerable theoretial investigation (*1-9*). These point-like defects are expected to modify the electronic p_z

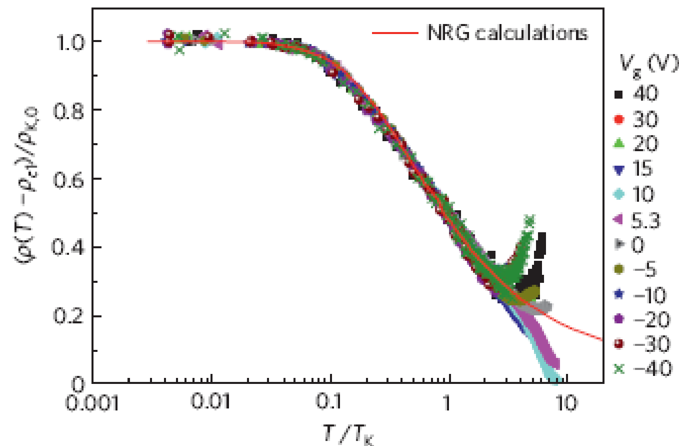

Fig 2-12 Universal Kondo behavior in graphene with lattice defects. The measured resistivity at all gate voltages is displayed. The red line is the expected universal Kondo behavior from numerical renormalization group calculations and fits the data well. Image is from Ref *(8).*

orbital of graphene, removing a conduction electron from the π-band and producing a localized magnetic moment in graphene. Recent experimental work performend by Chen *et al (8)* has investigated the temperature dependent charge transport in defected graphene. The temperature dependent ρ at all gate voltages exhibits a universal Kondo behavior (Fig 2-12). The Kondo effect has long been observed in metallic systems containing magnetic impurities. At low temperatures, resistiviy increases due the scattering of electrons from magnetic impurites. Near the Kondo temperature T_K, $\rho \propto \ln(T)$, whereas for $T << T_K$ the conduction electrons screen the magnetic moments and resistivity saturates, with a correction factor of $\rho \propto T^2$. As an essential component of the Kondo effect is the presence of magnetic moments, the observation of a universal Kondo behavior in defected graphene implies magnetic momnent formation due to lattice vacancies. Studies performed by Hong *et al (9)* measure features in charge transport which cannot be explained by existing theories but suggest adatom-induced magnetism in fluorinated graphene. Candini *et al* (*7*) measure hysteris in magnetic field dependent conductance measurements at very low temperature. The magnetoconductance is attributed to the magnetization reversal of paramagnetic centers in the graphene layer, possibly originating from defects in the device. In addition to charge transport measurements, bulk magnetometry has been used to investigate magnetism in graphene. Squid measurments of graphene exposed to point defects on graphene, in the form of adsorbed fluorine and lattice vacancies, show spin ½ paramagnetism, but no magnetic ordering even down to cryogentic temperatures (*1*). Other experimetnal investigations

using squid measurements show graphene exposed to point defects in the form of atomic hydrogen exhibits ferromagnetic behavior at room temperature (*6*).

While the experimental works discussed above present interesting and provocative results, direct evidence of magnetic moment formation in graphene is lacking. Results based on bulk squid magnetometry techniques measure the total magnetic signal but are unable to distinguish the origin of the signal, making these measurements susceptible to unintentional magnetic impurities. Studies based on charge transport can localize the measurements to the graphene device but do not directly probe the spin degree of freedom, and can be subject to various interpretations. These issues have led to uncertainty among scientists concerning validity of the results.

Utilizing non-local spin tranport in graphene devices provides a new approach able to directly probe magnetic moment formation in graphene exposed to defects or vacancies, conclusively resolving the issue of magnetism in graphene. Spin transport in graphene is introduced Chapter 3. In Chapter 9, the *spin-flip scattering* from magnetic moments generated by lattice vacancies and atomic hydrogen is investigated in detail. The resulting non-local spin transport and hanle spin precession data show clear signatures of magnetic moment formation due to atomic hydrogen adsorption or lattice vacancy defects.

References:

1. R. R. Nair *et al.*, Spin-half paramagnetism in graphene induced by point defects. *Nature Phys.*, **8**, 199 (2012).
2. O. Yazyev, Emergence of magnetism in graphene materials and nanostructures. *Rep. Prog. Phys.* **73**, 056501 (2010).
3. M. Sepioni *et al.*, Limits on intrinsic magnetism in graphene. *Phys. Rev. Lett.* **105**, 207205 (2010).
4. Y. Wang *et al.*, Room-temperature ferromagnetism of graphene. *Nano Lett.* **9**, 220 (2009).
5. H. S. S. Ramakrishna Matte, K. S. Subrahmanyam, C. N. R. Rao, Novel magnetic properties of graphene: Presence of both ferromagnetic and antiferromagnetic features and other aspects. *J. Phys. Chem. C* **113**, 9982 (2009).
6. L. Xie *et al.*, Room temperature ferromagnetism in partially hydrogenated epitaxial graphene. *Appl. Phys. Lett.* **98**, 193113 (2011).
7. A. Candini, C. Alvino, W. Wernsdorfer, M. Affronte, Hysteresis loops of magnetoconductance in graphene devices. *Phys. Rev. B* **83**, 121401 (2011).
8. J.-H. Chen, L. Li, W. G. Cullen, E. D. Williams, M. S. Fuhrer, Tunable Kondo effect in graphene with defects. *Nature Phys.* **7**, 535 (2011).
9. X. Hong, S.-H. Cheng, C. Herding, J. Zhu, Colossal negative magnetoresistance in dilute fluorinated graphene. *Phys. Rev. B* **83**, 085410 (2011).
10. B. Uchoa, V. N. Kotov, N. M. R. Peres, A. H. Castro Neto, Localized magnetic states in graphene. *Phys. Rev. Lett.* **101**, 026805 (2008).

11. K. Sengupta, G. Baskaran, Tuning Kondo physics in graphene with gate voltage. *Phys. Rev. B* **77**, 045417 (2008).

12. M. Hentschel, F. Guinea, Orthogonality catastrophe and Kondo effect in graphene. *Phys. Rev. B* **76**, 115407 (2007).

13. S.-P. Chao, V. Aji, Kondo and charge fluctuation resistivity due to Anderson impurities in graphene. *Phys. Rev. B* **83**, 165449 (2011).

14. B. Uchoa, A. H. Castro Neto, Superconducting states of pure and doped graphene. *Phys. Rev. Lett.* **98**, 146801 (2007).

15. F. Schedin *et al.*, Detection of individual gas molecules adsorbed on graphene. *Nature Mater.* **6**, 652 (2007).

16. K. S. Novoselov *et al.*, Electrical field effect in atomically thin carbon films. *Science* **306**, 666 (2004).

17. J. Martin *et al.*, Observation of electron-hole puddles in graphene using a scanning single-electron transistor. *Nature Phys* **4**, 144 (2008).

18. E. Fradkin, Critical behavior of disordered degenerate semiconductors. II. Spectrum and transport properties in mean-field theory. *Phys. Rev. B* **33**, 3263 (1986).

19. A. W. W. Ludwig, M. P. A. Fisher, R. Shankar, G. Grinstein, Integer quantum Hall transition: An alternative approach and exact results. *Phys. Rev. B* **50**, 7526 (1994).

20. P. A. Lee, Localized states in a d-wave superconductor. *Phys. Rev. Lett.* **71**, 1887 (1993).

21. N. M. R. Peres, F. Guinea, A. H. Castro Neto, Electronic properties of disordered two-dimensional carbon. *Phys. Rev. B* **73**, 125411 (2006).

22. A. K. Geim, K. S. Novoselov, The rise of graphene. *Nature Mater.* **6**, 183 (2007).

23. Y.-W. Tan *et al.*, Measurement of scattering rate and minimum conductivity in graphene. *Phys. Rev. Lett.* **99**, 246803 (2007).

24. F. Miao *et al.*, Phase-Coherent Transport in Graphene Quantum Billiards. *Science* **317**, 1530 (2007).

25. J.-H. Chen, C. Jang, S. Xiao, M. Ishigami, M. S. Fuhrer, Intrinsic and extrinsic performance limits of graphene devices on SiO_2. *Nature Nanotech.* **3**, 206 (2008).

26. E. H. Hwang, S. Adam, S. Das Sarma, Carrier Transport in Two-Dimensional Graphene Layers. *Phys. Rev. Lett.* **98**, 186806 (2007).

27. S. Das Sarma, S. Adam, E. H. Hwang, E. Rossi, Electronic transport in two-dimensional graphene. *Rev. Mod. Phys.* **83**, 407 (2011).

28. M. I. Katsnelson, A. K. Geim, Electron scattering on microscopic corrugations in graphene. *Phil. Trans. R. Soc. A* **366**, 195 (2008).

29. Z. H. Ni *et al.*, On Resonant Scatterers As a Factor Limiting Carrier Mobility in Graphene. *Nano Letters* **10**, 3868 (2010/10/13, 2010).

30. B. Huard, N. Stander, J. A. Sulpizio, D. Goldhaber-Gordon, Evidence of the role of contacts on the observed electron-hole asymmetry in graphene. *Phys. Rev. B* **78**, 121402 (2008).

31. R. Nouchi, M. Shiraishi, Y. Suzuki, Transfer characteristics in graphene field-effect transistors with Co contacts. *Appl. Phys. Lett.* **93**, 152104 (2008).

32. T. Mueller, F. Xia, M. Freitag, J. Tsang, P. Avouris, Role of contacts in graphene transistors: A scanning photocurrent study. *Phys. Rev. B* **79**, 245430 (2009).

33. F. Xia *et al.*, Photocurrent imaging and efficient photon detection in a graphene transistor. *Nano Lett.* **9**, 1039 (2009).

34. J. Park, Y. H. Ahn, C. Ruiz-Varga, Imaging of photocurrent generation and collection in single layer graphene. *Nano Lett.* **9**, 1742 (2009).

35. P. Blake *et al.*, Influence of metal contacts and charge inhomogeneity on transport properties of graphene near the neutrality point. *Solid State Commun.* **149**, 1068 (2009).

36. L. A. Ponomarenko *et al.*, Effect of a high-κ environment on charge carrier mobility in graphene. *Phys. Rev. Lett.* **102**, 206603 (2009).

37. C. Jang *et al.*, Tuning the effective fine structure constant in graphene: Opposing effects of dielectric screening on short- and long-range potential scattering. *Phys. Rev. Lett.* **101**, 146805 (2008).

38. C. R. Dean *et al.*, Boron nitride substrates for high-quality graphene electronics. *Nature Nanotech.* **5**, 722 (2010).

39. L. A. Ponomarenko *et al.*, Tunable metal-insulator transition in double-layer graphene heterostructures. *Nature Phys.* **7**, 958 (2011).

40. J.-H. Chen *et al.*, Charged-impurity scattering in graphene. *Nature Phys.* **4**, 377 (2008).

41. S. Adam, E. H. Hwang, V. M. Galitski, S. Das Sarma, A self-consistent theory for graphene transport. *Proc. Natl. Acad. Sci. U.S.A.* **104**, 18392 (2007).

42. J.-H. Chen, W. G. Cullen, C. Jang, M. S. Fuhrer, E. D. Williams, Defect scattering in graphene. *Phys. Rev. Lett.* **102**, 236805 (2009).

43. S.-H. Cheng *et al.*, Reversible fuorination of graphene: Evidence of a two-dimensional wide bandgap semiconductor. *Phys. Rev. B.* **81**, (2010).

44. D. C. Elias *et al.*, Control of graphene's properties by reversible hydrogenation: Evidence for graphane. *Science* **323**, 610 (2009).

45. J. Katoch *et al.*, Uncovering the dominant scatterer in graphene sheets on SiO2. *Phys. Rev. B.* **82**, 081417 (2010).

46. J. Moser *et al.*, Magnetotransport in disordered graphene exposed to ozone: From weak to strong localization. *Phys. Rev. B.* **81**, 205445 (2010).

47. B. Uchoa, C.-Y. Lin, A. H. Castro Neto, Tailoring graphene with metals on top. *Phys. Rev. B* **77**, 035420 (2008).

Chapter 3: Spin Transport in Graphene

Abstract:

Spintronics is an emerging field of study which utilized the spin of the electron for device functionality. Experimentally, electrical spin injection and transport have been studied in metals (*1-7*), semiconductors (*8-11*), and carbon nanotubes (*12, 13*). In the short time since its discovery, graphene has drawn considerable attention in the spintronics community due to high electronic mobility (*14*), gate tunability (*15*), room temperature spin transport (*16-19*), and theoretical predictions of low intrinsic spin-orbit coupling and hyperfine coupling (*20-23*).

In this chapter basic techniques used to investigate spin transport in graphene are introduced and recent advances in the field of graphene spintronics are discussed.

3.1 Local and non-local spin valve

Spin transport in graphene is investigated using a lateral non-local spin valve device. To introduce fundamental principles, we first discuss the more conventional structure, the local spin valve, which consists of two ferromagnetic (FM) electrodes separated by a non-magnetic (NM) material as seen in Figure 3-1A. In this thesis, graphene serves as the non-magnetic material. Due to the inherent spin imbalance present in FM materials, by applying a current between the two electrodes spins are injected from the FM into the graphene channel. The spins are then transported along the graphene and into the second FM. The signature of spin polarized transport is a change in resistance which depends on the orientation of injector and detector electrodes. Experimentally, this relative alignment is controlled by sweeping a magnetic field, B_{app}, along the easy axis of the electrodes,

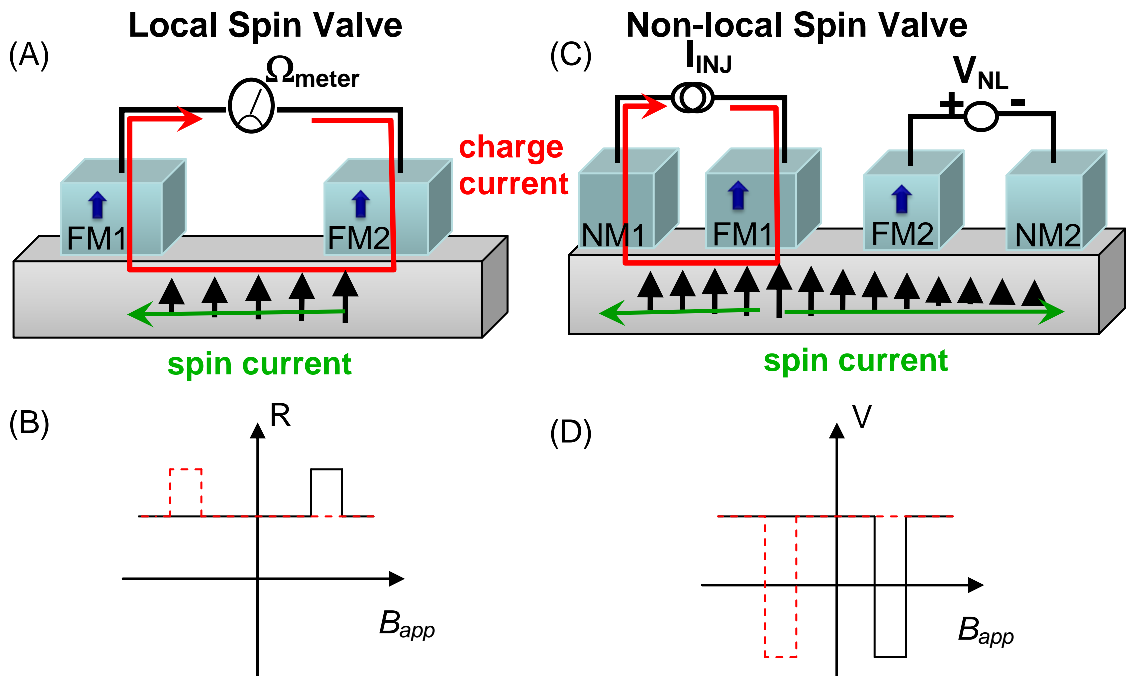

Fig 3-1 Lateral spin valve devices. (A) The non-local spin valve geometry with (B) schematic data. (C) Non-local spin valve geometry. The current path is separate from the voltage detection. (D) Schematic of data for non-local geometry

resulting in a low (high) resistance for parallel (antiparallel) orientation, as shown schematically in Figure 3-1B.

In the non-local geometry, the graphene is contacted by four electrodes as seen in Figure 3-1C. The inner two FM electrodes serve as injector and detector, while the outer two electrodes are non-magnetic and do not contribute to the spin signal. (To simplify fabrication, all four electrodes can be FM, but this is unnecessary and may result in additional voltage levels). The current path is no longer between the two FM electrodes, but instead between FM1 and the outer non-magnetic electrode NM1. Spins injected from FM1 travel towards FM2 through the process of diffusion, in the absence of charge current. The voltage measured between FM2 and NM2 is an indication of the spin density

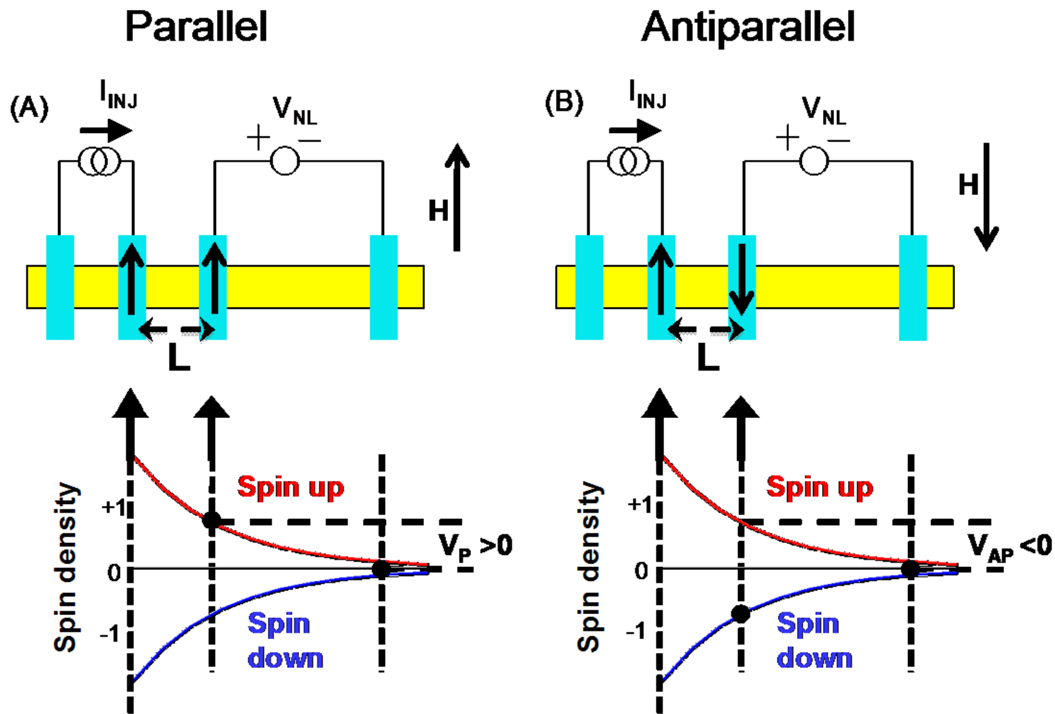

Fig 3-2 Spin density for (A) parallel and (B) antiparallel alignment of injector and detector electrodes.

reaching the detector electrode, and is sensitive to the relative orientation of the two FM electrodes (Fig 3-1C). A more detailed look at the spin density in the graphene device is provided in Figure 3-2. At the site of the injector electrodes, there is an accumulation of spin-up electrons with a corresponding deficit of spin-down electrons. The spin density decays along the length of the graphene due to spin relaxation processes. The detector electrode probes the spin density parallel to its magnetization, and will be positive for parallel alignment (Fig 3-2A) and negative for antiparallel alignment (Fig 3-2B). The measured voltage translates to the non-local resistance by R_{NL}=V/I with the difference measured for parallel and antiparallel alignments determining the non-local spin signal, $\Delta R_{NL}=(V_P-V_{AP})/I$, where I is the injection current.

While both local and non-local measurements detect spin dependent transport through associated changes in electronic signal, the non-local technique offers several advantages. First, the non-local measurement is more sensitive, providing better signal to noise ratio. Additionally, because the non-local technique is a voltage (not resistance) measurement, it is less susceptible to resistant artifacts such as anomalous Hall resistance and anisotropic magnetoresistance.

Although graphene is a two-dimensional material, the spin injection is assumed to be uniform along the length of the contact. Therefore, the one dimensional drift-diffusion equation (2-1) below, as developed by Takahashi and Maekawa (*24*), can be utilized to quantitatively analyze experimentally measured non-local resistance.

$$R_{NL}^{(P/AP)} = (+/-)2R_G e^{-L/\lambda} \prod_{i=1}^{2} \left(\frac{P_J \frac{R_i}{R_G}}{1-P_J^2} + \frac{P_F \frac{R_F}{R_G}}{1-P_F^2} \right) \times \left[\prod_{i=1}^{2} \left(1 + \frac{2\frac{R_i}{R_G}}{1-P_J^2} + \frac{2\frac{R_F}{R_G}}{1-P_F^2} \right) - e^{-2L/\lambda} \right]^{-1} \quad (2\text{-}1)$$

In the above equation, L is the distance between injector and detector electrodes, R_G is the graphene spin resistance, $R_{1,2}$ denotes the contact resistances of injector and detector electrodes, P_J is the spin polarization of the junction current, P_F is the ferromagnetic electrode spin polarization (assumed to be 0.35 for cobalt), R_F is the spin resistance of the ferromagnet, and λ_F is the spin diffusion length of the ferromagnet and $\lambda = \sqrt{D\tau}$, is the spin diffusion length, where D is the diffusion constant and τ the spin lifetime. Notably, the non-local spin signal depends strongly on the length. This relationship can be used to evaluate λ and is accomplished by fabricating a series of contacts on the same graphene flake at various L and fitting the observed length dependent R_{NL} to equation (2-1). It should be noted, this assumes each FM electrode exhibits the same spin injection properties.

3.2 Hanle spin precession

A second technique used to extract λ is based upon the Hanle effect and is considered to be the most definitive evidence that measured signals originate from spin injection. Additionally, only two FM electrodes are required, providing a clear advantage over fitting the length dependence of R_{NL}. In this method, the magnetic field is applied perpendicular to the sample causing the injected spin to precess as they diffuse along the sample. The spin density reaching the detector electrode is strongly dependent on the

applied field, as seen below in Figures 3-5C and 3-5D and can be fit to the Hanle equation

$$R_{NL} = S\int_0^{\infty} \frac{1}{\sqrt{4\pi D t}} \exp(-L^2/4Dt)\cos\left(\frac{g_e \mu_B}{\hbar} B_{app,z} t\right)\exp(-t/\tau)dt$$

in order to yield values for D and τ.

3.3 Spin transport in graphene

In 2007, the van Wees group reported the seminal work in the field of graphene spintronics, demonstrating electrical spin injection, transport, and detection in single layer graphene (*16*). Previous observations of magnetoresistance signals measured on graphene in a local spin valve geometry suggested spin transport, but possible artifacts could not be ruled out as the source of the signal, leaving the claim subject to doubt (*25*).

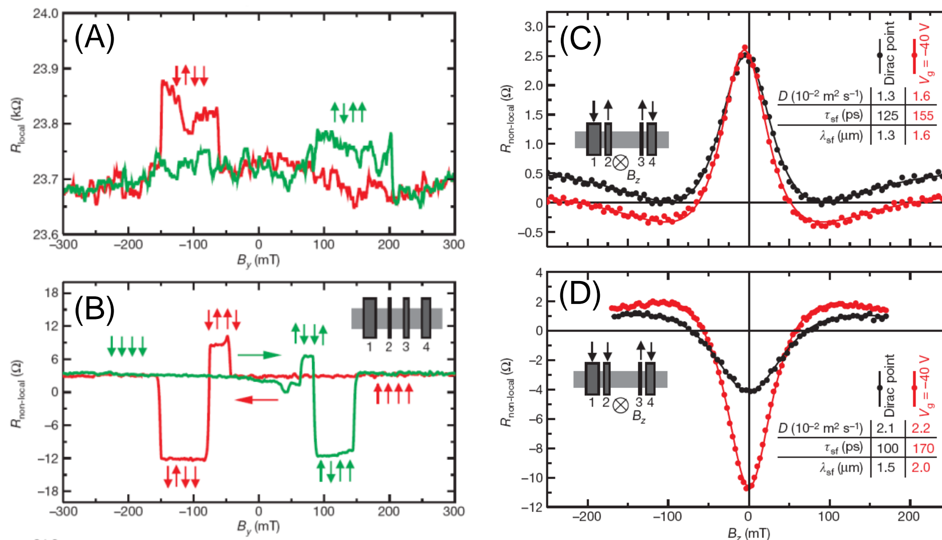

Fig 3-3 First demonstration of spin transport in graphene (A) Local spin valve signal. (B) Non-local signal. Hanle precession data for (C) parallel and (D) antiparallel alignment of injector and detector. Fitting of Hanle data yields τ_{sf} on the order of 100 ps, much lower than theoretically predicted. Figures are from Ref. *(16).*

On the contrary, Tombros *et al* (*16*) employed both local (Fig 3-3A) and non-local geometries (Fig 3-3B) in addition to spin precession measurements (Fig 3-3C and D) to conclusively demonstrate spin transport in graphene. Using a thin Al_2O_3 barrier between graphene and FM electrodes, they were able to observe non-local spin signal from cryogenic temperatures all the way to room temperature. The signal exhibited slight gate dependence, reaching a minimum ΔR_{NL} near the Dirac point. Interestingly, fitting of hanle precession yielded values for τ on the order of 100-150 ps. Later works have also measured surprisingly low lifetime values in the range of 50-200 ps (*17, 19, 26-28*).

The intrinsic spin lifetime in graphene is expected to be on the order of μs due to low spin orbit coupling and low hyperfine coupling (*20-23*). Spin orbit coupling is a relativistic effect in which the electric fields surrounding atomic nuclei are viewed as a magnetic field in the reference frame of a passing electron. The effective magnetic field interacts with the electron spin, resulting in spin relaxation. The strength of spin orbit coupling scales with atomic number, and hence should be small in carbon materials. Hyperfine coupling refers to the magnetic interaction between the spin of conduction electrons and nuclear spins. In graphene, this should also be a very small effect, as carbon is composed of ~99% ^{12}C, having no nuclear spin. The large disparity between experimentally observed and theoretically predicted lifetimes suggests extrinsic factors are limiting spin transport. A logical possibility is that the mechanisms limiting the charge-carrier mobilities also limit the spin relaxation times.

Motivated by this idea, the Kawakami group investigated the effect of surface chemical doping on spin transport. In particular, gold is intentionally deposited on the

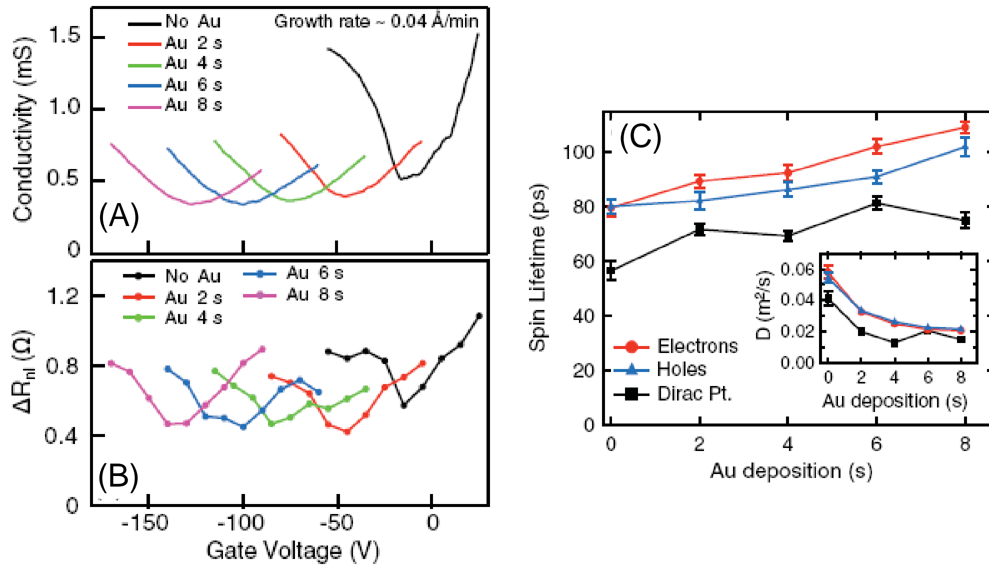

Fig 3-4 Surface Chemical Doping of graphene (A) Gate dependent σ as a function of Au doping. (B) Gate dependent ΔR_{NL} as a function of Au doping. Note no significant decrease in ΔR_{NL} with additional Au. (C) Spin lifetime as a function of Au. Inset: D vs. Au. Figures are from Ref. *(27)*.

surface of graphene spin valves in a highly controlled UHV environment, systematically adding charged impurities. While charge transport studies have shown charged impurities efficiently scatter momentum and are believed to be the dominant mechanism limiting mobility (*14, 29, 30*), surprisingly the study by Pi *et al (27)* shows they are not the dominant mechanism for spin relaxation in graphene. Comparing gate dependent conductivity (Fig 3-4A) and gate dependent ΔR_{NL} (Fig 3-4B) at various gold doping levels, it is apparent that the ΔR_{NL} tracks the gate dependent σ for the initial sample (as expected for transparent FM contacts) as well as subsequent Au doping. Most notably, the magnitude of ΔR_{NL} remains relatively unaffected, indicating charged impurities do not dramatically suppress spin lifetime. Direct measurements of τ via Hanle precession measurements provide further evidence, demonstrating that, in fact, spin lifetimes slightly

increase with increasing Au coverage (charged impurity concentration) as shown in Figure 3-4C.

A second extrinsic factor investigated by the Kawakami group involves the impact of contacts on spin transport in graphene. In chapter 8 I will discuss our work investigating the role of contact resistance, R_c, on ΔR_{NL}. The simple act of exposing graphene spin valve devices to water results in an enhancement of R_c, when transparent contacts are utilized (Co in direct contact with graphene) allowing direct comparisons of ΔR_{NL} on the same device. Increasing R_c by water exposure is found to increase ΔR_{NL}, indicating an enhanced spin injection efficiency, and also provides a simple method by which experimentalists can improve non-local signal magnitude.

An even more dramatic effect on spin transport is achieved through the careful engineering of highly resistive tunnel barrier contacts, as demonstrated by Han *et al (31, 32)*. Historically, spintronic investigations involving semiconductors have shown that spin injection from a FM contact to highly resistive material is inefficient and is often referred to as the conductivity mismatch problem. Spin injected into the device is able to diffuse along the channel, but also back into the FM contact, quickly loosing its orientation. Inserting a tunnel barrier between NM channel and FM electrode has been utilized in semiconductor spintronics in order to engineer a contact transparent enough to allow resistance measurements while also being opaque enough to prevent the backflow of spin. The low surface energy of graphene promotes clustering of deposited materials, making uniform tunnel barriers difficult to fabricate. To address this issue a technique utilizing a TiO_2 dressing layer and thin MgO barrier is used, and has successfully

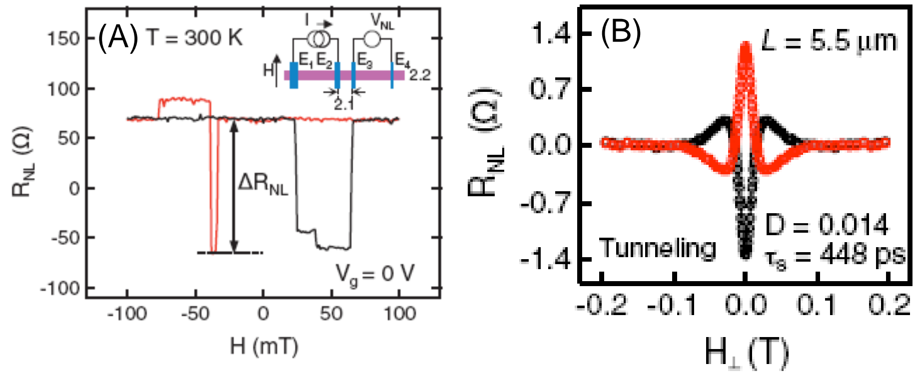

Fig 3-5 Tunneling spin injection into graphene (A) The use of tunnel barriers dramatically enhance ΔR_{NL} compared to transparent of pinhole contacts. (B) Spin lifetime is enhanced due to reduced contact induced spin relaxation. Images are from Ref. *(31)*.

produced tunneling spin injection into graphene. As a result, the largest value of ΔR_{NL}=130 Ω was observed at room temperature (Fig 3-5A) as well as spin lifetimes on the order of 500 ps (Fig 3-5B), considerably longer than previously observed τ~50-200 ps for transparent or pinhole contacts. Tunnel barriers greatly reduce the contact-induced spin relaxation and will be a necessary component for studies involving spin relaxation in graphene.

A third extrinsic factor examined by the Kawakami group involves magnetism in graphene. In Chapter 9 I will be presenting our work investigating graphene exposed to point defects in the form of atomic hydrogen or lattice vacancies. While theoretically predicted that disruption of p_z orbits in graphene by exposure to point defects may lead to the realization of magnetic moment formation, experimental results have been contradictory and controversial. To investigate this issue, a spin scattering measurement is performed utilizing non-local spin valve devices in which spin-polarized electrons

originate from the injector electrode, scatter from defect sites during transport along the sample, and are measured by a spin detector. The use of high quality tunnel barrier contacts is essential in this study, as the contact induced relaxation associated with transparent or pinhole electrodes can mask signatures of magnetic moment formation in the R_{NL} signal and hanle precession data. Unambiguous signatures of paramagnetic moment formation are detected in R_{NL} and hanle spin precession data, **only** after exposure to point defects, resolving the issue of magnetism in graphene.

References:

1. M. Johnson, R. H. Silsbee, Interfacial charge-spin coupling: injection and detection of spin magnetization in metals. *Phys. Rev. Lett.* **55**, 1790 (1985).
2. F. J. Jedema, A. T. Filip, B. J. v. Wees, Electrical spin injection and accumulation at room temperature in an all-metal mesoscopic spin valve. *Nature* **410**, 345 (2001).
3. F. J. Jedema, M. V. Costache, H. B. Heerche, J. J. A. Baselmans, B. J. v. Wees, Electrical detection of spin accumulation and spin precession at room temperature in metallic spin valves. *Appl. Phys. Lett.* **81**, 5162 (2002).
4. S. O. Valenzuela, D. J. Monsma, C. M. Marcus, V. Narayanamurti, M. Tinkham, Spin Polaried Tunneling at Finite Bias. *Phys. Rev. Lett.* **94**, 196601 (2005).
5. T. Kimura, Y. Otani, P. M. Levy, Electrical Control of the Direction of Spin Accumulation. *Phys. Rev. Lett.* **99**, 166601 (2007).
6. T. Kimura, T. Sato, Y. Otani, Temperature Evolution of Spin Relaxation in a NiFe/Cu Lateral Spin Valve. *Phys. Rev. Lett.* **100**, 066602 (2008).
7. T. Yang, T. Kimura, Y. Otani, Giant spin-accumulation signal and pure spin-current-induced reversible magnetization switching. *Nature Phys.* **4**, 851 (2008).
8. A. T. Hanbicki, B. T. Jonker, G. Itskos, G. Kioseoglou, A. Petrou, Efficient Electrical Spin Injection from a Magnetic Metal/Tunnel Barrier Contact into a Semiconductor. *Appl. Phys. Lett.* **80**, 1240 (2002).
9. O. M. van't Erve *et al.*, Electrical injection and detection of spin polarized carriers in silicon in a lateral transport geometry. *Appl. Phys. Lett.* **91**, 212109 (2007).

10. I. Appelbaum, B. Huang, D. J. Monsma, Electronic Measurement and Control of Spin Transport in Silicon. *Nature* **447**, 295 (2007).

11. X. Lou *et al.*, Electrical detection of spin transport in lateral ferromagnet-semiconductor devices. *Nature Phys.* **3**, 197 (2007).

12. S. Sahoo *et al.*, Electric field control of spin transport. *Nature Phys.* **1**, 99 (2005).

13. N. Tombros, S. J. van der Molen, B. J. van Wees, Separating Spin and Charge Transport in Single-Wall Carbon Nanotubes. *Phys. Rev. B* **73**, 233403 (2006).

14. C. R. Dean *et al.*, Boron nitride substrates for high-quality graphene electronics. *Nature Nanotech.* **5**, 722 (2010).

15. A. K. Geim, K. S. Novoselov, The rise of graphene. *Nature Mater.* **6**, 183 (2007).

16. N. Tombros, C. Jozsa, M. Popinciuc, H. T. Jonkman, B. J. van Wees, Electronic spin transport and spin precession in single graphene layers at room temperature. *Nature* **448**, 571 (2007).

17. W. Han *et al.*, Electron-hole asymmetry of spin injection and transport in single-layer graphene. *Phys. Rev. Lett.* **102**, 137205 (2009).

18. S. Cho, Y.-F. Chen, M. S. Fuhrer, Gate-tunable graphene spin valve. *Appl. Phys. Lett.* **91**, 123105 (2007).

19. M. Popinciuc *et al.*, Electronic spin transport in graphene field-effect transistors. *Phys. Rev. B.* **80**, 214427 (2009).

20. D. Huertas-Hernando, F. Guinea, A. Brataas, Spin-orbit coupling in curved graphene, fullerenes, nanotubes and nanotube caps. *Phys. Rev. B.* **74**, 155426 (2006).

21. D. Huertas-Hernando, F. Guinea, A. Brataas, Spin-Orbit-Mediated Spin Relaxation in Graphene. *Phys. Rev. Lett.* **103**, 146801 (2009).

22. H. Min *et al.*, Intrinsic and Rashba spin-orbit interactions in graphene sheets. *Phys. Rev. B* **74**, 165310 (2006).

23. Y. Yao, F. Ye, X.-L. Qi, S.-C. Zhang, Z. Fang, Spin-orbit gap of graphene: First-principles calculations. *Phys. Rev. B* **75**, 041401 (2007).

24. S. Takahashi, S. Maekawa, Spin injection and detection in magnetic nanostructures. *Phys. Rev. B* **67**, 052409 (2003).

25. E. W. Hill, A. K. Geim, K. S. Novoselov, F. Schedin, P. Blake, Graphene Spin Valve Devices. *IEEE Trans. Magn.* **42**, 2694 (2006).

26. C. Jozsa, M. Popinciuc, N. Tombros, H. T. Jonkman, B. J. van Wees, Electronic Spin Drift in Graphene Field-Effect Transistors. *Phys. Rev. Lett.* **100**, 236603 (2008).

27. K. Pi *et al.*, Manipulation of Spin Transport in Graphene by Surface Chemical Doping. *Phys. Rev. Lett.* **104**, 187201 (2010).

28. W. Han *et al.*, Electrical detection of spin precession in single layer graphene spin valves with transparent contacts. *Appl. Phys. Lett.* **94**, 222109 (2009).

29. J.-H. Chen *et al.*, Charged-impurity scattering in graphene. *Nature Phys.* **4**, 377 (2008).

30. S. Adam, E. H. Hwang, V. M. Galitski, S. Das Sarma, A self-consistent theory for graphene transport. *Proc. Natl. Acad. Sci. U.S.A.* **104**, 18392 (2007).

31. W. Han *et al.*, Tunneling spin injection into single layer graphene. *Phys. Rev. Lett.* **105**, 167202 (2010).

32. W. Han, R. K. Kawakami, Spin relaxation in single-layer and bilayer graphene. *Phys. Rev. Lett.* **107**, 047207 (2011).

Chapter 4: Device Fabrication and Measurement

Abstract:

In this section I present the detailed recipes used to fabricate graphene devices for charge and spin transport studies. The samples are measured in a unique *in-situ* ultra high vacuum (UHV) chamber which combines temperature dependent transport measurements with molecular beam epitaxy, atomic hydrogen source, and Argon sputtering capabilities. I discuss the various aspects of the chamber and electrical measurements.

4.1 Device Fabrication

The studies discussed in the following chapters use mechanically exfoliated graphene placed on a Si/SiO_2 substrate, where the SiO_2 layer is 300 nm. The fabrication procedure employed to achieve functional devices is outlined below.

4.1.1 Preparation of Si/SiO_2

The substrate used is purchased commercially, and arrives in the form of 4" wafers. Using a diamond scribe, the wafer is cleaved into several small rectangular samples, approximately 5 mm x 10 mm. Samples that are substantially larger than these dimensions will not be able to fit on the sample paddle for measurements, while smaller samples are difficult to secure to the sample paddle. To provide easy identification throughout the fabrication process, a letter is scribed on the back of each Si/SiO_2 piece. The samples are then cleaned in a chemical hood having positive airflow using the following steps:

1) Ultrasonic in Acetone for 15 mins
2) Ultrasonic in IPA for 10 mins
3) Ultrasonic in IPA for 10 mins
4) Flush samples with IPA for several seconds
5) Dry with clean Nitrogen gas
6) Heat samples on hot plate at 150 °C for at least 10 mins. If samples will be left for a substantially longer time, cover them with foil to prevent the accumulation of dust.

Clean samples can be stored in a vacuum box indefinitely prior to transferring graphene, although the number and quality of transferred graphene pieces tends to be higher when performed directly after cleaning of the substrate in finished.

4.1.2 Mechanical Exfoliation

Mechanical exfoliation, also referred to as the scotch tape method, describes the basic process of peeling off layers of graphene from bulk graphite and transferring to a desired substrate. Each individual seems to have their own tips and tricks. The method I use is as follows

1) Start with high quality highly oriented porolytic graphite, HOPG (SPI supplies, ZYA grade, 1 cm x 1 cm). Gently lay scotch tape across the HOPG and apply pressure with the index finger. The goal is to have no air-bubbles between HOPG and tape.
2) Slowly peel off the tape, producing a shiny square of flat, thin graphite. With graphite side up (sticky side up) attach the tape to a flat surface using two pieces of tape far away from the graphite.
3) Press a second piece of tape to the graphite square, apply pressure, then slowly remove. Fold and peel this once, resulting in two squares of very thin graphite.
4) Position the freshly peeled graphite section over the sample and apply pressure using the flat side of tweezers for approximately 30 seconds. Slowly peel back the tape and use optical microscopy to identify suitable pieces of single layer graphene.

4.1.3 Alignment marks

A 2 mm x 2 mm matrix of numbers and crosses is created using standard electron beam lithography techniques on the sample. The alignment marks are necessary so the graphene piece can be easily located to write patterns for electrical contacts. The crosses are separated by 50 um, with numbers every 500 μm. Also, 1000 μm to the right of the numbers and crosses are three large squares aligned in a vertical column. The first step towards alignment marks requires spin coating the sample with electron beam resist as described below

1) Using a clean glass pipette, drop a small amount of MMA electron beam resist only the sample. Using a ramp rate of 500 rpm/s, increase the speed to 3000 rpm. Hold steady at 3000 rpm for 45 sec then ramp down to 0 rpm at a rate of 500 rpm/s.
2) Transfer to a hotplate at 150 °C and bake for 2 minutes
3) Let the sample cool for 1 min
4) Using a clean glass pipette, drop a small amount of PMMA electron beam resist only the sample and spin coat using the same parameters as step 1).
5) Transfer to a hotplate at 170 °C and bake for 20 minutes
6) Let the sample cool for 1 min

Using a diamond scribe, a scratch is made on the right edge of the sample at approximately the same level as the graphene piece. The scratch provides a surface to focus on and also indicates the relative position for the alignment mark matrix. A scanning electron microscope (SEM) exposes the alignment mark pattern, which is then developed as follows

1) Immerse in MIBK:IPA 1:3 for 80 seconds

2) Immerse in IPA for 20 seconds

3) Immerse in water for 20 seconds

4) Dry using nitrogen gas

4.1.4 Defining the electrodes

The position of the graphene in the matrix is noted and several optical images of the graphene and surrounding areas are captured, with examples shown in Figure 4-1. The

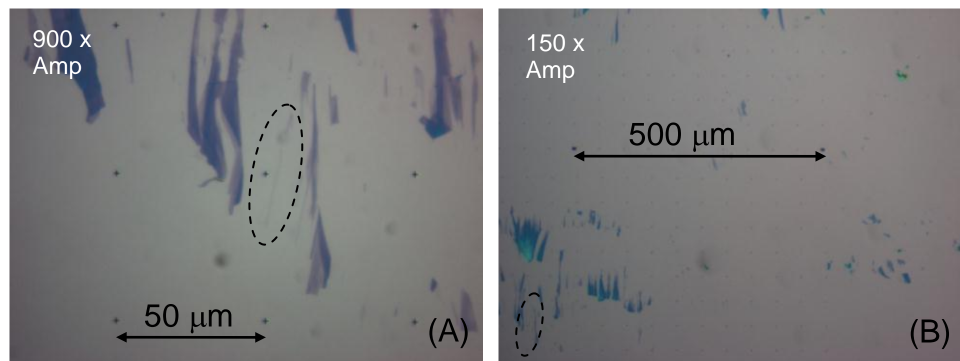

Fig 4-1 Alignment mark matrix written using electron beam lithography. (A) Optical image at (A) 900× amplification and (B) 900× amplification. The graphene is circled and arrows highlight the distance between crosses in (A) and numbers in (B).

optical images are pieced together using NPGS software and the electrode pattern is created. Each graphene sample has a unique position, size and shape, and will require an individually created electrode pattern. A second step of electron beam lithography exposes the pattern for electrodes. The procedure for developing the exposed electron-beam resist is the same as described in the previous section.

The next step is to deposit material to electrically contact the graphene. In this thesis, three types of devices are studied: hall bars, spin valves with transparent contacts, and

spin valves with tunnel barrier contacts. At this point, the fabrication steps vary depending on the final device required.

4.1.5 Depositing MgO/Co for transparent contacts

To fabricate spin valves with transparent contacts, electrodes are grown in a molecular beam epitaxy (MBE) chamber having base pressure below 1×10^{-9} torr. The growth is a two step process

1) Deposit a 2 nm MgO masking layer at normal incidence (0°)
2) Deposit 80 nm of Co at an angle of 7°. This angle evaporation technique reduces the contacting area between Co and graphene and is expected to increase spin signal. The process and final structure is detailed in Figure 4-2.

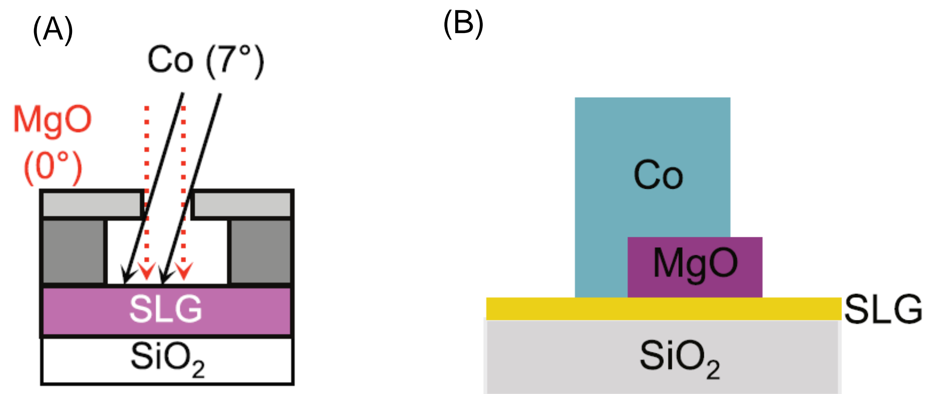

Fig 4-2 Fabrication of transparent contact spin valves. (A) Angle evaporation of MgO and Co results in electrodes (B) where a small area of Co is directly contacting graphene.

4.1.6 Depositing Ti/Au

Rather than depositing MgO/Co, the next step for hall bars and tunnel barrier spin valves requires Ti(10 nm)/Au(80 nm) electrodes. The material is deposited in a

commercial electron beam evaporator at base pressure below 5×10^{-6} Torr. The samples are then placed in PG remover at 70° C for approximately 30 mins to lift off the metal. They are rinsed in Acetone then IPA and dried using nitrogen gas. At this point, the hall bar device is complete, as shown in Fig 4-3A, but the spin valve sample has only outer non-magnetic electrodes as seen in Fig 4-3B. The tunnel barrier sample is annealed in ultra high vacuum at 150 °C for 1 hour. The sample then goes through a second spin

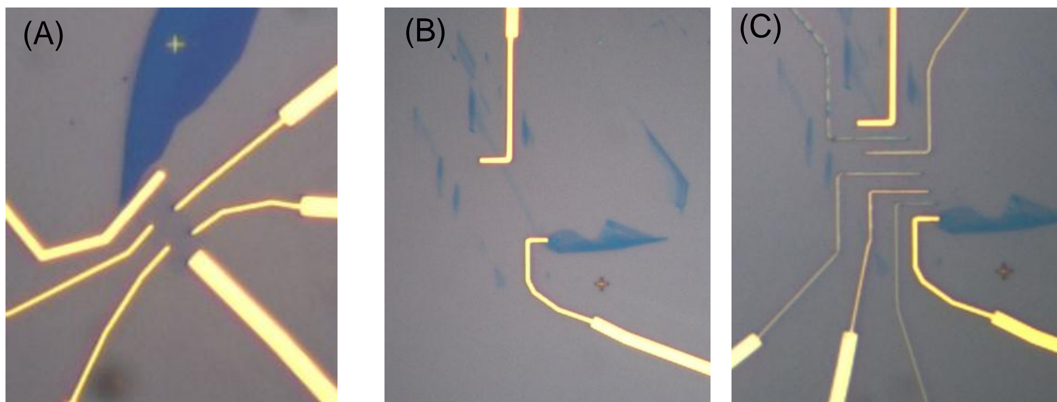

Fig 4-3 Device structures (A) A hall bar device, having Ti/Au electrodes. (B) The first step in fabricating a tunnel barrier spin valve device is depositing the outer non-magnetic Ti/Au electrodes. (C) A second step of e-beam lithography and metal deposition is needed to create in inner FM electrodes for the tunnel barrier spin valve.

coating and electron beam lithography step to define the inner ferromagnetic electrodes.

4.1.7 Depositing Ti/MgO/Co for tunnel barrier contacts

The growth of inner FM electrodes takes place in the MBE chamber using the following steps

1) Deposit 0.14 nm of Ti at 0° and 0.14 nm at 9°.

2) Leak in O_2 to a pressure of ~5×10^{-8} torr and keep stable for 30 minutes, allowing the Ti to fully oxidize.

3) Deposit 3 nm of MgO at 0° to serve as a masking layer, followed by 0.9 nm of MgO deposited at 9° for the tunnel carrier.

4) Deposit 80 nm of Co at 7°.

The details of the evaporation are provided in Fig. 4-4.

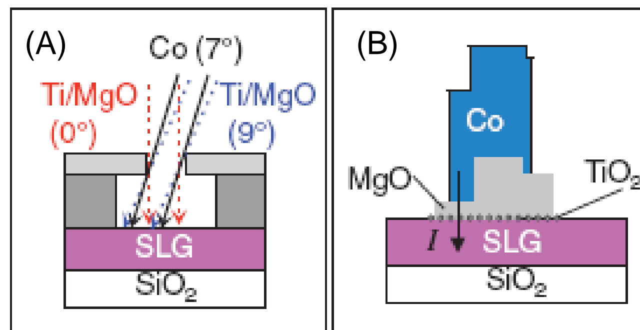

Fig 4-4 Fabrication of tunnel barrier spin valves. (A) Angle evaporation of Ti, MgO and Co results in electrodes (C) where Co is separated from graphene and current flows through the thin tunnel barrier, as indicated by the arrow

4.1.8 Capping with Al_2O_3

Prior to lift-off, transparent and tunnel barrier spin valves are capped with 5 nm Al_2O_3. The growth is performed at an angle of 7°, to match the Co deposition angle, and should minimize oxidation of the FM electrodes. The metal is then lifted off in PG remover. The final step is to rinse the sample in Acetone followed by IPA and dry using nitrogen. An optical image of a tunnel barrier spin valve device is displayed in Fig 4-3C.

4.2 Ultra high vacuum system

The ultra high vacuum (UHV) system, as shown schematically in Figure 4-5 is an integral component to the work presented in this thesis. The UHV system is divided into

several smaller components: load lock, buffer chamber, main MBE chamber, and small MBE chamber. Each portion has important functions. The load lock chamber is necessary

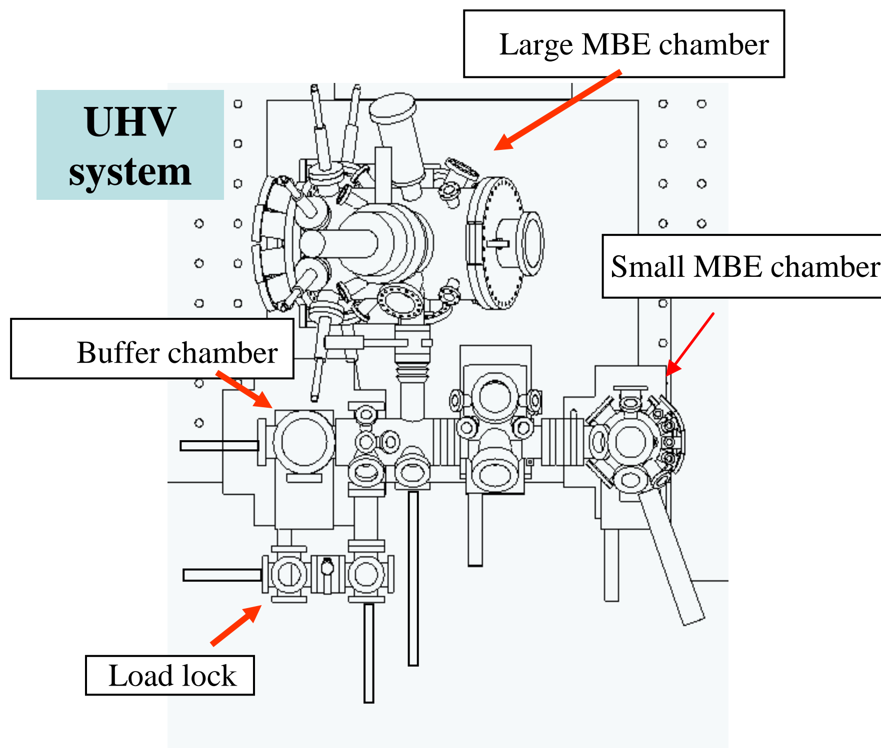

Fig 4-5 Top view of the ultra high vacuum system.

for quick and easy sample entry and exit into the UHV system. The pressure can be decreased from atmosphere to ~1×10^{-6} torr in less than an hour. At this point, the sample is loaded into the buffer chamber, where base pressure is 1×10^{-9}. The presence of the intermediate buffer chamber between load lock and growth chambers keeps the pressure in the growth chambers lower, better controlled, and the chambers free of contaminants. The buffer chamber also contains a heater, used in cleaning procedures, and low energy electron diffraction and auger spectroscopy capabilities. The main molecular beam epitaxy chamber (MBE) is used for the growth of electrodes, as described in the previous

section. MBE is a technique by which materials are heated in ultra high vacuum until they begin to sublimate. The “beam” of material is directed toward the substrate, resulting in a slow, layer by layer growth of high quality material. There are two different types of cells used in the MBE chamber. The first is a thermal evaporation cell. The desired material (i.e. Co, Fe, Pt, Au) is contained in a ceramic crucible, which is wrapped in conducting wire. Passing current through the wire and heats the material, resulting is sublimation. The second cell uses electron bombardment to locally heat the material and is used for Ti and MgO evaporation. A series of transfer arms, having 4 clips, mate with the circular sample pocket, as seen in Fig 4-6A, and allow samples to be transferred between the load lock, buffer chamber and main chamber. Moving samples into and out of the small MBE chamber require sliding the small rectangular paddle (Fig 4-6B) out of the large circle pocket. The paddle has been specially designed to fit into the small MBE chamber, where temperature dependent transport measurements can be completed while depositing material on the sample via MBE, sputtering, or exposing to atomic hydrogen.

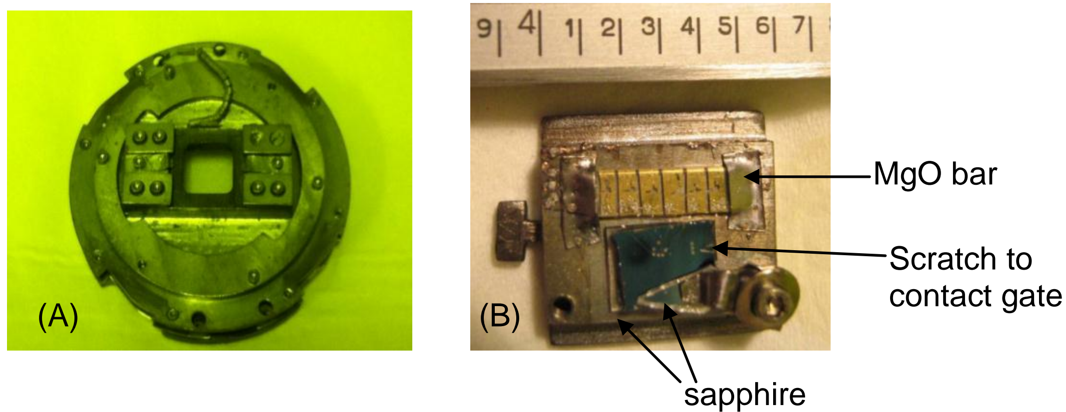

Fig 4-6 Sample pocket and sample paddle. (A) The large circle paddle is used to move samples into the UHV system. (B) The small paddle fits into the center of the pocket. The small MBE chamber is compatible with small paddles only.

4.3 Small MBE chamber

The studies discussed in this thesis are performed in the small MBE chamber. This provides a highly controlled environment for investigations involving the effects of doping or defecting graphene. In order to electrically contact the sample, 6 pins are carefully lowered onto the MgO bar by rotating a key, as shown in Fig 4-7.

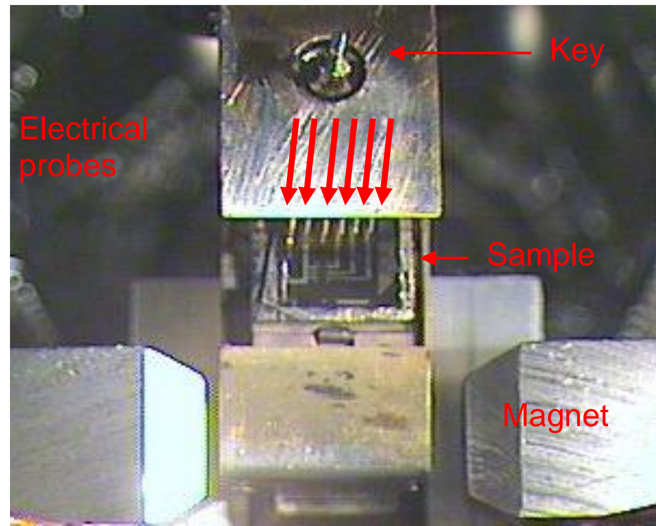

Fig 4-7 Sample measurement in the small MBE chamber.

The sample can be cooled to a base temperature of ~13 K using a constant flow of helium. A Lakeshore 331 controller monitors the sample temperature and controls the power to a small heater near the sample.

4.4 Electrical Measurements

Standard lock-in techniques are used for electrical measurements to provide improved signal to noise ratio. A schematic of the set-up is provided in Fig 4-8. The lock-in amplifier outputs an oscillating voltage signal, which is converted to an AC current using a home-made current source. For a standard gate dependent resistivity measurement, the current is applied between the two outer electrodes while the voltage between two inner electrodes is probed using the SR-560, and sent back to the amplifier. The carrier concentration is controlled by applying a gate, which is achieved using a Keithley 2400 voltage source.

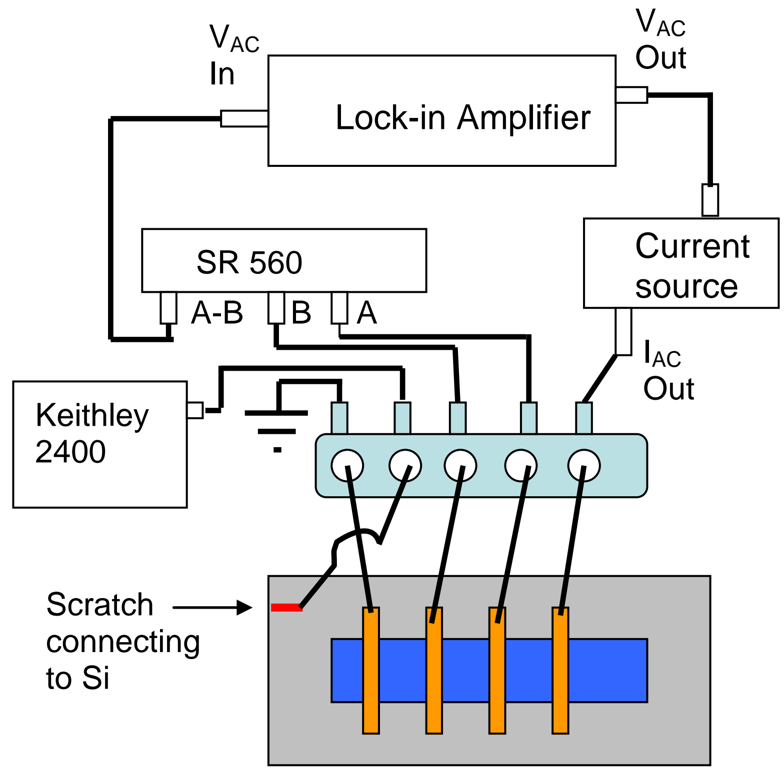

Fig 4-8 Schematic of electrical measurement.

Chapter 5: Electronic Doping and Scattering by Transition Metals on Graphene[1]

Abstract:

In this section we investigate the effects of transition metals (TM) on the electronic doping and scattering in graphene using molecular beam epitaxy combined with *in situ* transport measurements. The room temperature deposition of TM onto graphene produces clusters that dope *n-type* for all TM investigated (Ti, Fe, Pt). We also find that the scattering by TM clusters exhibits different behavior compared to 1/*r* Coulomb scattering. At high coverage, Pt films are able to produce doping that is either *n-type* or weakly *p-type*, which provides experimental evidence for a strong interfacial dipole favoring *n-type* doping as predicted theoretically.

---

[1]Published as: K. Pi, **K. M. McCreary**, W. Bao, Wei Han, Y. F. Chiang, Yan Li, S.-W. Tsai, C. N. Lau, and R. K. Kawakami, *Phys. Rev B*. **80**, 075406 (2009)

5.1 Introduction

Transition metal (TM) adatoms and clusters on graphene have recently been a topic of great interest: at low density, they are expected to induce doping, scattering (*1*), and novel magnetic (*2-4*) and superconducting (*5*) behavior; at high density (up to continuous coverage), they may locally dope or modify the band structure of graphene (*6-8*). Because of their importance for graphene-based electronics and the investigation of novel phenomena (*1-14*), there have been extensive theoretical studies (*1-8, 13, 14*). In contrast, the experimental exploration of TM/graphene systems is much more limited.

A key issue to investigate is the charge transfer between the TM and graphene because it is responsible for both the local doping and the charge impurity scattering. Generally, the relative work function (WF) between the TM and the graphene are believed to be important factors for determining the charge transfer (*11*), *i.e.* graphene will be *p*-doped (*n*-doped) if the TM's WF is larger (smaller) than graphene. Recently, density functional calculations predict the presence of a strong interfacial dipole that promotes the *n-type* doping of graphene (*8*). However, experimental studies of the local doping by TM contacts have yet to find evidence for this strong interfacial dipole layer (*9-12*).

In this work, we report *in situ* transport measurements of TM/graphene systems as a function of TM coverage for several different metals, using a molecular beam epitaxy (MBE) deposition system with built-in electrical probes. Similar techniques have been applied to study gases (*15*), molecules (*16*), and alkali metal (*17*) adatoms on graphene. The metals used in the study are Ti, Fe, and Pt, with WF of 4.3, 4.7, and 5.9 eV (*18*),

respectively (the WF of graphene is 4.5 eV (*19, 20*)). Surprisingly, at low coverage, the TM clusters dope graphene *n-type*, regardless of its WF relative to that of graphene. For the scattering at low coverage, we find that the scattering by TM clusters exhibits different behavior compared to $1/r$ Coulomb scattering. Extending to high coverage, we make the important observation that Pt films are able to produce doping that is either *n-type* or weakly *p-type*. Because WF considerations alone would predict strong *p-type* doping, this result provides experimental evidence for the strong interfacial dipole favoring *n-type* doping as calculated theoretically (*8*).

5.2 Sample Description

Samples are prepared by mechanical exfoliation of Kish graphite onto a SiO_2/Si substrate (300 nm thickness of SiO_2). Single layer graphene flakes are identified by optical microscopy and Raman spectroscopy (*21*). Figure 5-1A shows a scanning electron microscope (SEM) image of a typical graphene device with Au/Ti electrodes defined by e-beam lithography. The device is annealed under Ar/H_2 environment at 200°C for one hour to remove resist residue (*22, 23*) and degassed in ultrahigh vacuum at 90°C for one hour. The room temperature MBE deposition of TM atoms (growth pressure $< 7\times10^{-10}$ torr) is calibrated by a quartz deposition monitor. The coverage is converted from atoms/cm^2 to "monolayers" (ML) where 1 ML is defined as 1.908×10^{15} atoms/cm^2, the areal density of primitive unit cells in graphene. For low coverage, the room temperature deposition of TM leads to clustering as shown in the atomic force microscope (AFM) image of 0.01 ML Pt on graphene (Figure 5-1B). The presence of isolated adatoms

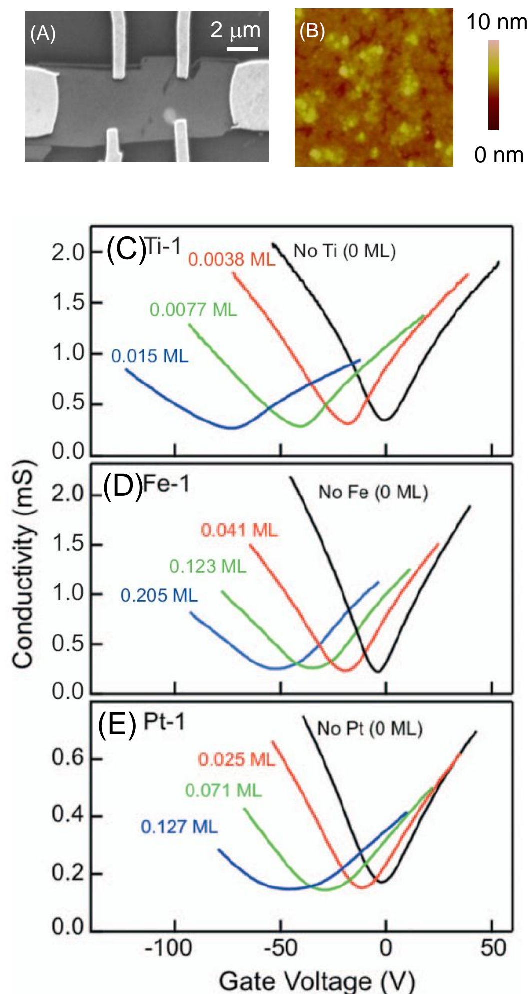

Fig 5-1 Graphene doped with transition metal adsorbates. (A) SEM image of a graphene device with Au(100 nm)/Ti(10 nm) electrodes. (B) AFM image of 0.01 ML of Pt deposited on single-layer graphene. (C-E) The gate-dependent conductivity at selected TM coverage for Ti, Fe, and Pt, respectively.

cannot be ruled out by the AFM, but are unfavorable theoretically (*6*). *In situ* transport measurements are performed using standard lock-in detection (1 μA excitation).

5.3 Results

The fine control of TM deposition provides the ability to probe the effect of small amounts of material on the transport properties of graphene. Figure 5-1C shows representative gate dependent conductivity scans for various thicknesses of Ti in the low

coverage regime. The minimum in the gate dependent conductivity identifies the position of the Dirac point (V_D), while the slope corresponds to the mobility of charge carriers in the graphene. With increasing coverage, two characteristic behaviors are observed. First, the introduction of Ti on the graphene surface results in shifting the Dirac point towards more negative gate voltages, indicating that the Ti is a donor, producing *n-type* doping in the graphene. Second, the slope of the conductance curves away from the Dirac point decreases, indicating that the Ti introduces additional scattering to lower the mobility. Both of these characteristics are also observed for Fe doping (Figure 5-1D) and Pt doping (Figure 5-1E).

Figure 5-2 highlights the relation between the Dirac point shift ($V_{D,shift} = V_D - V_{D,initial}$) and TM coverage for a collection of Ti, Fe, and Pt samples in the low coverage

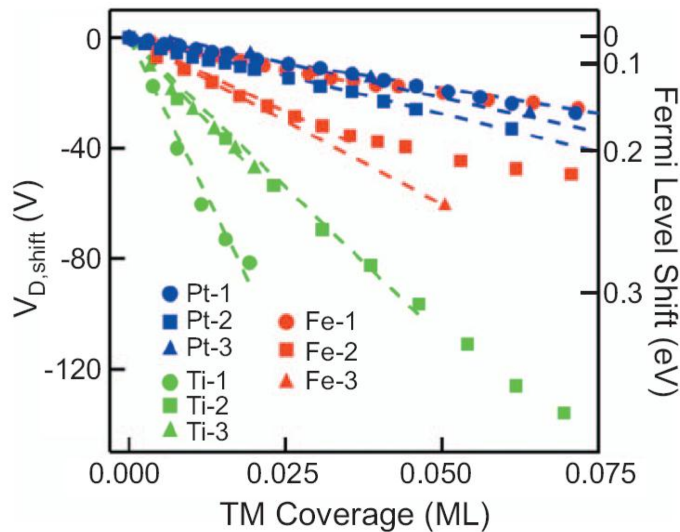

Fig 5-2 Dirac point shift vs coverage for nine separate samples. The dashed lines indicate the linear fit used to define the doping efficiencies, which are: 0.174, 0.092, and 0.082 electrons/ atom for Ti-1, Ti-2, and Ti-3, respectively; 0.017, 0.040, and 0.046 electrons/atom for Fe-1, Fe-2, and Fe-3, respectively; 0.014, 0.021, and 0.019 electrons/atom for Pt-1, Pt-2, and Pt-3, respectively.

regime. Despite the sample-to-sample variations which may be due to differences in the graphene surface purity, growth rate uncertainties, and the possible dependence of graphene WF on flake size or edge roughness (*24*), several important features are discovered. First, all samples, including the Pt samples with WF greater than graphene, result in *n-type* doping. Second, the three different TM result in three different ranges for slopes, with the Ti samples exhibiting the most negative initial slopes (-2169 to -4602 V/ML). From this value the doping efficiency, or number of electrons transferred per Ti atom to graphene is determined by knowing the carrier concentration associated with the given change in gate voltage ($\Delta n = \alpha \Delta V_g$, where $\alpha = 7.2\times10^{10}$ $V^{-1}cm^{-2}$ based on calculated capacitance values). The doping efficiency is in the range of 0.082 to 0.174 electrons per Ti atom. The Fe shows the next strongest efficiency (0.017 to 0.046), while the Pt is the weakest electron donor with the efficiency of 0.014 to 0.021 electrons transferred for each Pt atom. Upon recalling the bulk WFs of Ti (4.3 eV), Fe (4.7 eV), and Pt (5.9 eV), it is apparent that the WF of the TM directly affects the doping efficiency, with electrons being more easily transferred from the lowest WF material, Ti, compared to the highest WF material, Pt. Although the WF of Fe is much closer to that of Ti, the doping efficiency of Fe is more similar to that of Pt. This behavior implies that in addition to the work function, wave function hybridization, structural modifications, or other effects may contribute to the electronic doping of graphene.

Figures 5-3A through 5-3C show the conductivity as a function of carrier concentration [$n = -\alpha(V_g - V_D)$]. The electron and hole mobilities are determined by taking the slope of the conductivity away from the Dirac point ($\mu_{e,h} = |\Delta\sigma / e\Delta n|$) (*15, 17*).

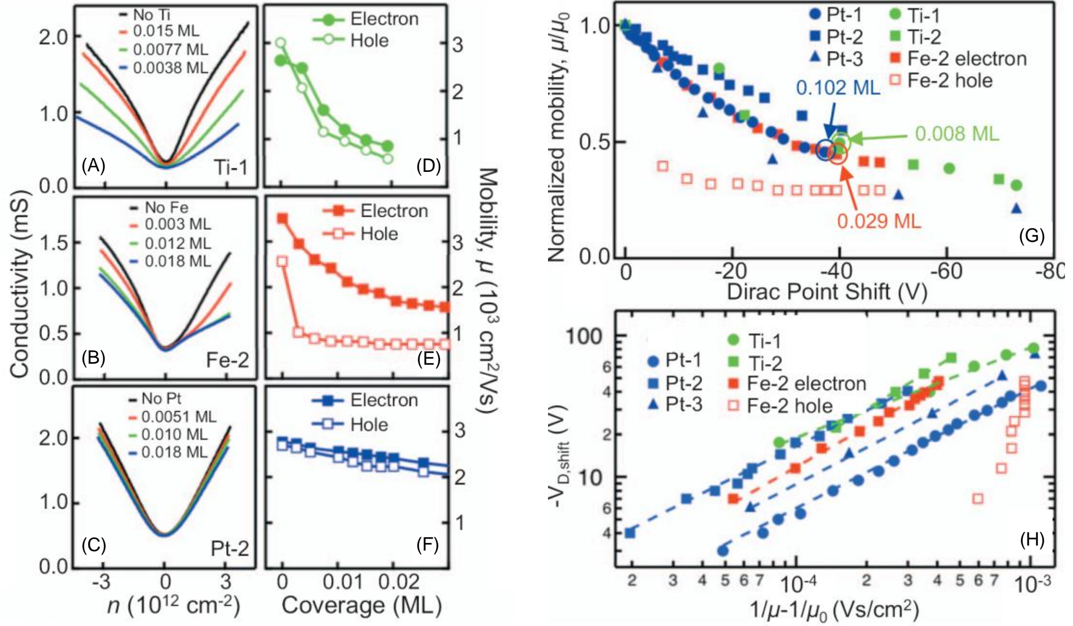

Fig 5-3 Comparing conductivity, mobility, normalized mobility, and -$V_{D,shift}$ for graphene samples doped with Ti, Fe, and Pt. (A-C) The conductivity vs carrier concentration for Ti, Fe, and Pt, respectively, for four different TM coverages. (D-F) The electron and hole mobilities for Ti, Fe, and Pt, respectively, as a function of TM coverage. (G) The normalized mobility (μ/μ_0) vs Dirac point shift. The data points corresponding to 0.102 ML Pt, 0.008 ML Ti, and 0.029 ML Fe on samples Pt-1, Ti-1, and Fe-2 are circled. (H) -$V_{D,shift}$ is plotted vs $1/\mu$-$1/\mu_0$. The dashed lines are power-law fits to the equation, $-V_{D,shift} \sim \Gamma_{TM}{}^{b}$, where b is 0.64, 1.01, 0.85, 0.83, 0.86, and 0.95 for Ti-1, Ti-2, Pt-1, Pt-2, Pt-3, and Fe-2 electrons, respectively.

Figures 5-3D through 5-3F illustrate the detailed dependence of mobility on the TM coverage for Ti, Fe, and Pt samples in the low coverage regime. Comparing the different samples at equivalent coverages, the Ti exhibits the strongest scattering and Pt has the weakest scattering. Noting that the trend in the scattering (Ti > Pt) matches that of the doping efficiency, we investigate this relationship by plotting the normalized mobility (*25*) against the Dirac point shift (Figure 5-3G). The average mobility, $\mu = (\mu_e + \mu_h)/2$, is plotted for Ti and Pt. The Fe samples typically exhibit a reduction of hole mobility which is most pronounced in sample Fe-2, so μ_e and μ_h are plotted separately. Comparing the

different materials shows that the mobility reduction of Ti, Pt, and Fe (electrons) is much more strongly related to the Dirac point shift than the TM coverage (Figure 5-3G). Because the Dirac point shift not only measures the doping level in the graphene but also the average charge density of the TM, the data shows that the scattering is related to the average charge density of the clusters—a characteristic that is plausible for Coulomb scattering. However, we point out that this behavior is actually different from what is calculated for Coulomb scattering by point-like scatterers with $1/r$ potential (*26*). Specifically, in ref. 26, the scattering per impurity does not scale linearly with the impurity charge (α_ε) and instead has a strong quadratic component, resulting in scattering that scales as $\alpha_\varepsilon^2 n_{imp} = \alpha_\varepsilon(\alpha_\varepsilon n_{imp}) \sim \alpha_\varepsilon(V_{D,shift})$. Due to the presence of the material-dependent α_ε factor (i.e. doping efficiency), the mobility vs. Dirac point shift curves should be significantly different for different materials. Therefore, the observed scattering by TM clusters exhibits behavior that differs from $1/r$ Coulomb scattering by isolated impurities (*1*).

Additionally, we analyze the power law relationship between the scattering and doping effects. The total scattering rate is $\Gamma = \Gamma_0 + \Gamma_{TM}$, where Γ_0 is the scattering rate of the undoped sample and Γ_{TM} is the scattering rate induced by the TM. Because mobility is inversely proportional to scattering, the quantity $1/\mu - 1/\mu_0$ is proportional to Γ_{TM}. The relationship between the Dirac point shift and Γ_{TM} is investigated by plotting $-\Delta V_{D,shift}$ vs. $1/\mu - 1/\mu_0$ on a log-log scale (Figure 5-3H). The dashed lines are power law fits, $-\Delta V_{D,shift} \sim (\Gamma_{TM})^b$, with values of b ranging from 0.64 – 1.01 as indicated in the figure caption. Compared to the results of Chen et. al. (*17*) which find values of b = 1.2-1.3 for scattering

by isolated potassium impurities, our results with $b \leq 1$ indicate a different behavior for scattering by TM clusters.

A surprising result from the studies at low coverage (Figures 5-1 through 5-3) is the *n-type* doping of graphene by Pt. If the WF is the only factor affecting the transfer of electrons between materials, Pt is expected to dope graphene strongly *p-type*, since the WF of Pt (5.9 eV) is significantly larger than that of graphene (4.5 eV). Density functional calculations of bulk TM on graphene (*8*) present a possible explanation for this observed behavior by predicting the formation of an interfacial dipole layer, resulting in a potential step to favor *n-type* doping ($\Delta V = 0.9$ eV). So far, however, there has been no experimental evidence for such a strong dipole layer forming at the interface between a bulk TM and graphene (*9-12*). To investigate the theoretical prediction of a strong interfacial dipole layer between the graphene and bulk TM, we extend the Pt-doping study to higher coverage to study the charge transfer from Pt films. Figure 5-4A displays V_D as a function of coverage for several Pt-doped samples. An initial rapid shift toward negative voltages is observed in all samples. As more Pt is deposited, bringing the sample into the medium coverage regime, the rate of shift in V_D slows and reaches a minimum value before gradually increasing towards more positive voltages. At high coverage, the Dirac point stabilizes and shows very little variation with additional deposition. The sample morphology is measured by *ex situ* AFM. The AFM image for 0.62 ML of Pt shows that the Pt is still in the form of isolated clusters (Figure 5-4B). At the higher coverage of 3.19 ML, the Pt forms a connected film with some uncovered regions of graphene (Figure 5-4C). The connected film provides a parallel conduction pathway that

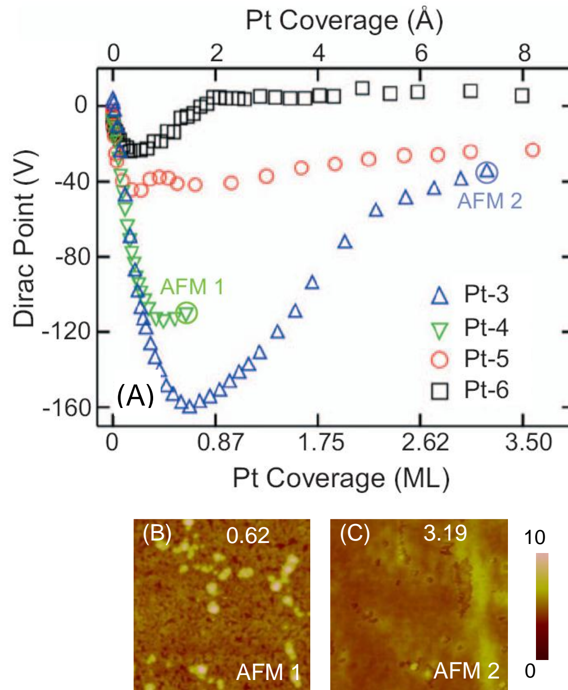

Fig 5-4 Pt-doped graphene at high coverage. (A) The Dirac point as a function of Pt coverage up to high coverage. (B) AFM image of 0.62 ML Pt exhibits isolated clusters. (C) AFM image of 3.19 ML Pt indicates a connected film with some areas of bare graphene.

contributes to the measured conductivity value, but should not be gate dependent. The gate dependence of the conductivity is primarily due to the chemical potential shift of the graphene that is not covered by the metal. For graphene in direct contact with metal, the local chemical potential is pinned, exhibiting no gate dependence. Transport measurements provide a reliable method for determining the V_D as well as the type of doping (electron or hole) in the uncovered graphene regions for both the clusters and the partially covered films. Thus, the final values of V_D in the high coverage regime clearly show that Pt films can produce either *n-type* or weak *p-type* doping of the graphene. This sample-to-sample variation is most likely due to differences in the initial surface purity among samples. Although hydrogen cleaning is performed on all samples, trace amounts

of resist residue could remain, directly affecting the TM-graphene spacing. Due to the highly spacing-dependent interfacial dipole strength (*8*), any variation in the spacing will directly effecting the type and amount of doping. The fact that both *n-type* and weak *p-type* doping is observed provides experimental evidence for the presence of a strong interfacial dipole layer favoring *n-type* doping as predicted theoretically (*8*) because the expected doping based only on WF considerations would lead to strong *p-type* doping.

An interfacial dipole whose strength decreases with increasing equilibrium spacing (d_{eq}) (*8*) provides a possible explanation for the non-monotonic behavior of the Dirac point shift in Pt samples. Based on theoretical calculations, the d_{eq} between TM adatoms and graphene is less than 3 Å (*6*) while for bulk TM the distance increases to ~3.3 Å (*8*). The *n-type* doping observed in samples at low coverage is an indication of a strong interfacial dipole favoring *n-type* doping, as expected for low coverages exhibiting a small d_{eq}. As the bulk-like regime is approached, the increasing d_{eq} decreases the dipole strength and hence reduces the *n-type* doping efficiency as observed by the shift in the Dirac point toward positive voltages. We emphasize that the interfacial dipole provides just one possible scenario to explain the non-monotonic evolution of the Dirac point shift. A quantitative understanding is complicated by the fact that the WF can differ from bulk values for small clusters (< 4 nm lateral size) (*27*) and the corresponding quantity for adatoms (should they be present) is the first ionization energy. Therefore, further theoretical calculations are needed to fully understand the doping effect of clusters. Regardless of the exact mechanism for doping by clusters, an interfacial dipole is still necessary to explain the *n-type* or weak *p-type* doping measured in the bulk-like regime.

5.4 Summary

In conclusion, the exploration of TM/graphene systems leads to several important observations. At low coverage, the doping efficiency is found to be related to the TM WFs, but Ti, Fe, and Pt all exhibit *n-type* doping even for materials with higher WF than graphene (i.e. Fe, Pt). Extending the Pt doping study to higher thickness, the doping can either be *n-type* or weakly *p-type*. Because WF considerations alone would generate strong *p-type* doping, this result provides experimental evidence for the strong interfacial dipole favoring *n-type* doping as predicted by theory (*8*). Analysis of the scattering at low coverage indicates that the scattering by TM clusters exhibits different behavior compared to $1/r$ Coulomb scattering.

References:

1. M. I. Katsnelson, F. Guinea, A. K. Geim, Scattering of electrons in graphene by clusters of impurities. *Phys. Rev. B* **79**, 195426 (2009).
2. B. Uchoa, V. N. Kotov, N. M. R. Peres, A. H. Castro Neto, Localized magnetic states in graphene. *Phys. Rev. Lett.* **101**, 026805 (2008).
3. B. Uchoa, C.-Y. Lin, A. H. Castro Neto, Tailoring graphene with metals on top. *Phys. Rev. B* **77**, 035420 (2008).
4. A. V. Krasheninnikov, P. O. Lehtinen, A. S. Foster, P. Pyykkö, R. M. Nieminen, Embedding Transition-Metal Atoms in Graphene: Structure, Bonding, and Magnetism. *Phys. Rev. Lett.* **102**, 126807 (2009).
5. B. Uchoa, A. H. Castro Neto, Superconducting states of pure and doped graphene. *Phys. Rev. Lett.* **98**, 146801 (2007).
6. K. T. Chan, J. B. Neaton, M. L. Cohen, First-principles study of metal adatom adsorption on graphene. *Phys. Rev. B* **77**, 235430 (2008).
7. Y. Mao, J. Yuan, J. Zhong, Density functional calculation of transition metal adatom adsorption on graphene. *J. Phys. Condens. Matter* **20**, 115209 (2008).
8. G. Giovannetti *et al.*, Doping Graphene with Metal Contacts. *Phys. Rev. Lett.* **101**, 026803 (2008).
9. E. J. H. Lee, K. Balasubramanian, R. T. Weitz, M. Burghard, K. Kern, Contact and edge effects in graphene devices. *Nature. Nanotech.* **3**, 486 (2008).
10. F. Xia *et al.*, Photocurrent Imaging and Efficient Photon Detection in a Graphene Transistor. *Nano Lett.* **9**, 1039 (2009).

11. B. Huard, N. Stander, J. A. Sulpizio, D. Goldhaber-Gordon, Evidence of the role of contacts on the observed electron-hole asymmetry in graphene. *Phys. Rev. B* **78**, 121402 (2008).

12. J. Park, Y. H. Ahn, C. Ruiz-Varga, Imaging of photocurrent generation and collection in single layer graphene. *Nano Lett.* **9**, 1742 (2009).

13. H. Sevinçli, M. Topsakal, E. Durgun, S. Ciraci, Electronic and magnetic properties of 3d transition-metal atom adsorbed graphene and graphene nanoribbons. *Phys. Rev. B.* **77**, 195434 (2008).

14. M. I. Rojas, E. P. M. Leiva, Density functional theory study of a graphene sheet modified with titanium in contact with different adsorbates. *Phys. Rev. B* **76**, 155415 (2007).

15. F. Schedin *et al.*, Detection of individual gas molecules adsorbed on graphene. *Nature Mater.* **6**, 652 (2007).

16. D. B. Farmer *et al.*, Chemical doping and electron-hole donduction asymmetry in graphene devices. *Nano Lett.* **9**, 388 (2008).

17. J.-H. Chen *et al.*, Charged-impurity scattering in graphene. *Nature Phys.* **4**, 377 (2008).

18. *CRC Handbook of Chemistry and Physics*. (CRC Press, Boca Raton, FL, 2008).

19. S. J. Sque, R. Jones, P. R. Briddon, The transfer doping of graphite and graphene. *Phys. Status Solidi A.* **204**, 3078 (2007).

20. N. Ooi, A. Rairkar, J. B. Adams, Density functional study of graphite bulk and surface properties. *Carbon* **44**, 231 (2006).

21. A. C. Ferrari, Raman spectrum of graphene and graphene layers. *Phys. Rev. Lett.* **97**, 187401 (2006).

22. S. V. Morozov *et al.*, Giant intrinsic carrier mobilities in graphene and its bilayer. *Phys. Rev. Lett.* **100**, 016602 (2008).

23. M. Ishigami, J. H. Chen, W. G. Cullen, M. S. Fuhrer, E. D. Williams, Atomic structure of graphene on SiO_2. *Nano Lett.* **7**, 1643 (2007).

24. R. Ramprasad, P. von Allmen, L. R. C. Fonseca, Contributions to the work function: A density-functional study of adsorbates at graphene ribbon edges. *Phys. Rev. B* **60**, 6023 (1999).

25. *The mobility is normalized to cancel uncertainties related to the determination of the effective lengths and widths of the graphene flakes.*

26. D. S. Novikov, Elastic scattering theory and transport in graphene. *Phys. Rev. B* **76**, 245435 (2007).

27. M. Pushkin *et al.*, Study of the tunnel conductance and electronic screening in nanoclusters of *d* metals on graphite surface. *Bull. Russ. Acad. Sci. Phys.* **72**, 878 (2008).

Chapter 6: Metallic and Insulating Adsorbates on Graphene[1]

Abstract

In the following chapter, we directly compare the effect of metallic titanium (Ti) and insulating titanium dioxide (TiO_2) on the transport properties of single layer graphene. The deposition of Ti results in substantial *n*-type doping and a reduction of graphene mobility by charged impurity scattering. Subsequent exposure to oxygen largely reduces the doping and scattering by converting Ti into TiO_2. In addition, we observe evidence for short-range scattering by TiO_2 impurities. These results illustrate the contrasting scattering mechanisms for identical spatial distributions of metallic and insulating adsorbates.

[1]Published as: **K. M. McCreary**, K. Pi, and R. K. Kawakami, *Appl. Phys. Lett*. **98,** 192101 (2011)

6.1 Introduction

The interaction of electrons in graphene with surface adsorbates is a central issue for electronic mobility, correlated electron physics (*1, 2*), and applications in chemical sensors (*3, 4*). Furthermore, metals and insulators on graphene surfaces are employed for essential device elements such as electrical contacts (*5*), gate dielectrics (*6, 7*), and tunnel barriers (*8, 9*), so it is important to understand their influence on the electronic properties of graphene. While experiments have separately investigated the doping of graphene by metallic (*10-12*) and insulating adsorbates (*12, 13*), the transition from metallic to insulating behavior of the adsorbates has not been explored.

In this paper, we compare the electronic properties of graphene doped with metallic Ti and insulating TiO_2 and investigate the transition between the metallic and insulating states of the adsorbates. The experiments are performed in ultrahigh vacuum (UHV) where submonolayer amounts of Ti are deposited onto graphene electronic devices and subsequently converted to TiO_2 by a partial pressure of oxygen gas. The evolution of the electronic properties is monitored by *in situ* transport measurements during the entire deposition and oxidation process, which allows direct comparison between Ti- and TiO_2-doping for identical spatial distribution of the dopant atoms. We find that the Ti doping produces substantial charge transfer to the graphene (*n*-type doping) and a strong reduction of mobility due mainly to charged impurity scattering. As the Ti is converted to TiO_2, the effects of the adsorbates are largely reversed: both the charge transfer and impurity scattering are greatly reduced. This clearly demonstrates that insulating adsorbates have much less influence on the electronic properties of graphene as compared

to metallic adsorbates. Furthermore, we find evidence that TiO_2 impurities produce short-range scattering in single layer graphene. Because Ti is often used for adhesion of electrical contacts and TiO_2 is used as a seed layer for tunnel barriers (*8*), the results for these materials are particularly important for understanding the electronic and spintronic properties of graphene devices.

6.2 Sample Preparation

Samples are prepared by mechanical exfoliation of highly oriented pyrolytic graphite onto a SiO_2/Si substrate (300 nm thickness of SiO_2). Single layer graphene (SLG) flakes are identified by optical microscopy and Raman spectroscopy (*14*). Ti/Au electrodes are defined by electron beam lithography. Devices are then annealed in a Ar/H_2 environment to remove resist residue (*15, 16*) and loaded into UHV to be degassed (*11*).

The sample is then transferred under UHV to a molecular beam epitaxy (MBE) system where *in situ* transport measurements are performed during the deposition of Ti adatoms. The Ti is deposited from a triode electron beam source (*17*). During the Ti deposition, the pressure remains below 7×10^{-10} torr. The sample is held at room temperature, which will promote the formation of clusters (*12*). The deposition rate is calibrated by a quartz deposition monitor. The submonolayer coverage is converted from atoms/cm^2 to "monolayers" (ML) where 1 ML is defined as 1.908×10^{15} atoms/cm^2, the areal density of primitive unit cells in graphene.

6.3 Results

Figure 6-1A displays the gate dependent conductivity (σ) for clean graphene and for select amounts of Ti deposition. The conductivity is measured in a four-probe geometry

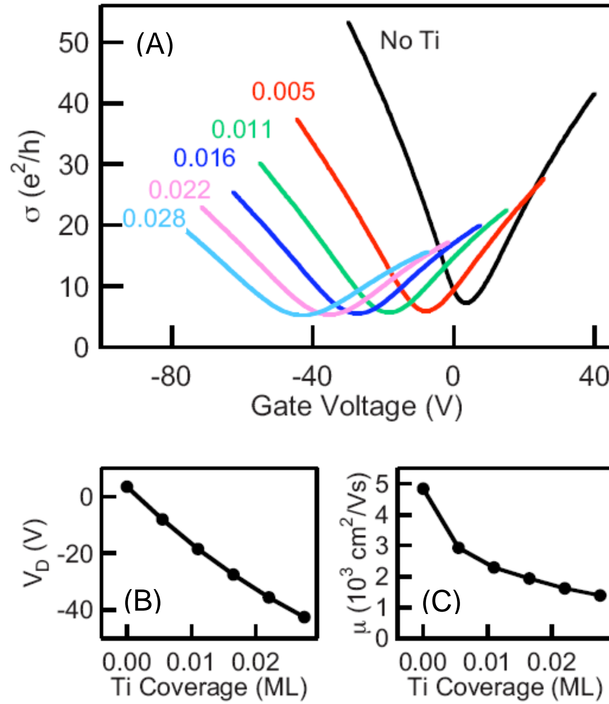

Fig 6-1 Ti-doped graphene. (A) The gate dependent conductivity at selected values of Ti coverage. (B, C) The Dirac point and mobility, respectively, as a function of Ti coverage.

using standard lock-in detection techniques. The minimum conductivity (σ_{min}) as a function of gate voltage (V_g) identifies the Dirac point (V_D). The carrier concentration is calculated as $n = -(\kappa\varepsilon_0/ed)(V_g - V_D)$, where κ is the relative dielectric constant of SiO_2 (3.9), ε_0 is the permittivity of free space, and d is the dielectric thickness (300 nm). This yields $n = -\alpha(V_g - V_D)$ with $\alpha = 7.2\times10^{10}$ $V^{-1}cm^{-2}$. The slope of σ in the linear regions to the right (left) of the V_D is directly related to electron (hole) mobility through the relation $\mu_{e,h}=\Delta\sigma/e\Delta n$. Prior to Ti deposition, the clean graphene exhibits a V_D close to zero V_g, indicating little chemical doping. The average mobility, defined as $\mu=(\mu_e+\mu_h)/2$, is 4830 cm^2/Vs, typical for graphene supported by a SiO_2 substrate. As Ti is deposited, V_D shifts to more negative gate voltages, indicating electrons are being transferred from Ti to

graphene. The charge transfer results in positively charged impurities on the surface, which act as sources of additional scattering for charge carriers in the graphene. The widening of the curves in Figure 6-1A with increased Ti deposition signifies the mobility is decreasing, and is a clear indication of the additional scattering. Figure 6-1B plots the values for the V_D, while Figure 6-1C shows the average mobility for the clean sample and five Ti depositions. As a result of 0.028 ML Ti deposition, V_D shifts from +3.5 V to -42.5 V while μ is reduced from 4830 to 1390 cm^2/Vs, consistent with previous studies (*11*).

Following the deposition of Ti, the sample is left undisturbed in the UHV environment while the conductivity is measured at discrete time intervals. Figure 6-2A shows the gate dependent conductivity measured immediately after deposition along with 6, 23, 47, and 103 minutes after the 0.028 ML Ti deposition. Note that the data labeled 0 min in Figure 6-2A is labeled 0.028 ML Ti in Figure 6-1A. During this time, there are small changes in both mobility and V_D, most likely due to cluster formation (*12*). Subsequently, oxygen is leaked into the chamber at a pressure of 1×10^{-6} torr. Exposure to oxygen has an immediate and drastic effect on the measured transport properties. The Dirac point shifts to more positive voltages, showing that the transformation from metallic Ti to insulating TiO_2 decreases the electronic doping level of the graphene. This is reasonable when one compares metals and insulators on a simplified level. Metals have free electrons which can easily be transferred to graphene, whereas the electrons in insulators are tightly bound. Therefore the presence of TiO_2 on graphene should have little effect on the electronic doping. In conjunction with the decrease in doping is an increase in mobility, as is seen in Figure 6-2B by the narrowing of the curves with longer

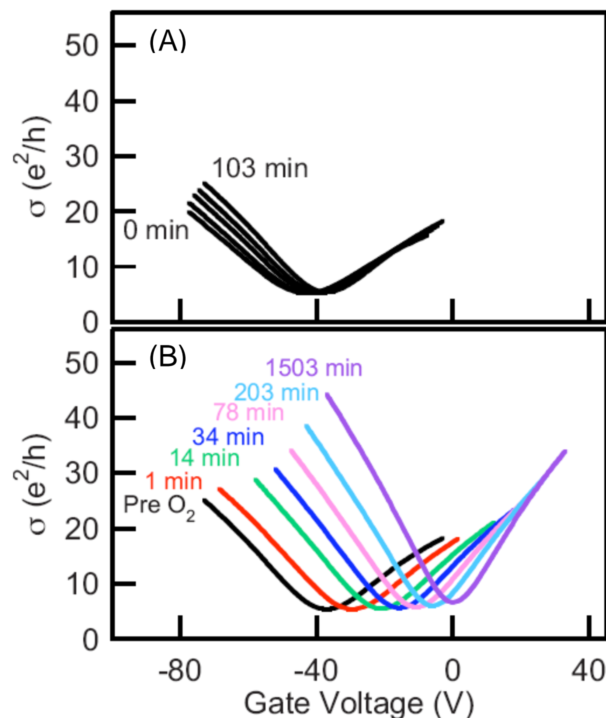

Fig 6-2 Effect of cluster formation and oxygen exposure on Ti-doped graphene. (A) The gate dependent conductivity is displayed for 0, 6, 23, 47 and 103 minutes following the final Ti deposition. (B) The gate dependent conductivity prior to O_2 exposure and after 1, 14, 34, 78, 203, and 1503 minutes of exposure to oxygen at a pressure of 1×10^{-6} torr.

oxygen exposure. The results of Ti deposition and oxidation are summarized in Figure 6-3, which shows the gate dependent conductivity for the clean device, 0.028 ML Ti and fully oxidized Ti impurities. The final Dirac point of 0 V almost fully recovers to the initial Dirac point of +3.5 V. To ensure that these effects are not related to physisorption of oxygen to the graphene surface (which could produce electronic doping (*18*)), we perform control experiments on clean graphene devices in UHV. For an exposure of 1300 Langmuirs of O_2, there is no observable change in the mobility and the Dirac point shifts by less than 2 V, indicating that any physisorbed oxygen has negligible effect.

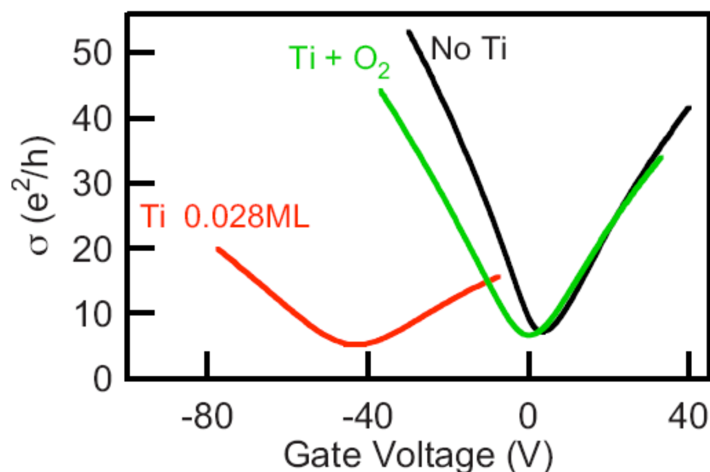

Fig 6-3 A comparison of the gate dependent conductivity curves measured for the clean sample, after 0.028 ML Ti deposition, and after 1503 minutes of oxygen exposure.

The recovery of the Dirac point to nearly its initial value relies on the property of autocompensation of TiO_2 surfaces (*19*). The strong electronegativity of oxygen results in Ti being positively charged while the oxygen will be negatively charged. In principle, this could produce a polar surface that introduces electronic doping in the graphene: if the TiO_2 is terminated by Ti, the positive bound charges would induce a strong *n*-type doping in the graphene. However, UHV studies find that TiO_2 surfaces are autocompensated (*19*), meaning the proportion of Ti and O surface atoms are balanced, making the surface charge-neutral. The incomplete recovery of the Dirac point suggests that there is not a perfect autocompensation between the Ti and O—the chemical interaction between the Ti atoms and the graphene may alter the energetics of autocompensation.

To investigate the relationship between electron scattering and the amount of charge on the impurities, we plot the mobility and minimum conductivity as a function of the Dirac point voltage. Figure 6-4A shows μ vs. V_D and Figure 6-4B shows σ_{min} vs. V_D

throughout the Ti doping, cluster formation, and oxidation steps. The effect of Ti doping is represented by the solid black circles and follows the path from “1” to “2” in Figures 6-4A and 6-4B with V_D shifting to negative values while both μ and σ_{min} are reduced. The cluster formation is represented by green crosses from “2” to “3”. The oxidation is represented by the open red circles from “3” to “4” with V_D shifting back toward zero while μ and σ_{min} are both increasing. Interestingly, the paths followed by μ and σ_{min} during the oxidation step (“3” to “4”) fall on nearly the same curves as for the initial Ti deposition (“1” to “2”). The overlap of the deposition and oxidation curves is expected if the main scattering mechanism is long-range charged impurity scattering. In this case the electron scattering should depend only on the amount of charge located on the impurities (i.e. the Dirac point voltage) and not on its chemical species or local bonding. Thus, these results indicate that the main scattering mechanism for Ti and partially oxidized Ti is charged impurity scattering. Looking more closely, the oxidation curves for σ_{min} and μ exhibit a different behavior when the Ti is nearly fully oxidized (near “4”). When the oxidation curves are extrapolated to the initial V_D of +3.5 V, σ_{min} extrapolates to the initial value for clean graphene (“1”, Fig 6-4B), but μ extrapolates to a value less than the initial value for clean graphene (“1”, Fig 6-4A). The different behavior occurs because σ_{min} is determined by the formation of electron-hole puddles which are generated by the long-range charged impurity scattering (*13, 20*). On the other hand, μ can have contributions from both long-range and short-range scattering. Thus, σ_{min} is expected to have a full recovery for charge-neutral impurities, while the reduced value of μ (extrapolated to $V_D \rightarrow +3.5$ V) indicates a contribution from short-range scattering by

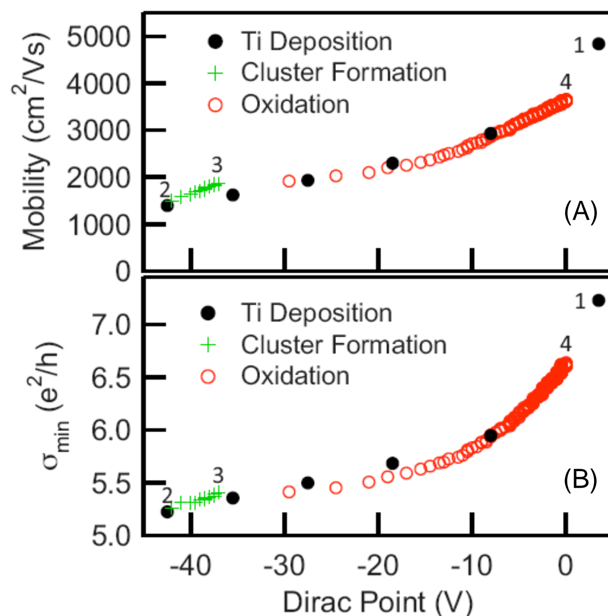

Fig 6-4 (A, B) **The mobility and minimum conductivity, respectively, as a function of Dirac point voltage**. The solid black circles in each graph correspond to Ti deposition, green crosses to cluster formation, and open red circles to oxidation.

TiO_2 impurities. This is consistent with recent evidence for short-range scattering by insulating layers on SLG (*7*).

6.4 Conclusion

In conclusion, we have monitored the electronic properties of doped graphene as impurities are transformed from Ti to TiO_2. It is determined that the conversion of adsorbates from metallic to insulating behavior largely reverses both the charge transfer and charged impurity scattering. The trends observed in mobility indicate that the presence of TiO_2 introduces additional short-range scattering to the system.

References:

1. B. Uchoa, A. H. Castro Neto, Superconducting states of pure and doped graphene. *Phys. Rev. Lett.* **98**, 146801 (2007).
2. B. Uchoa, V. N. Kotov, N. M. R. Peres, A. H. Castro Neto, Localized magnetic states in graphene. *Phys. Rev. Lett.* **101**, 026805 (2008).
3. F. Schedin *et al.*, Detection of individual gas molecules adsorbed on graphene. *Nature Mater.* **6**, 652 (2007).
4. O. Leenaerts, B. Partoens, F. M. Peeters, Adsoption of H_2O, NH_3, CO, NO_2, and NO on graphene: A first-principles study. *Phys. Rev. B* **77**, 125416 (2008).
5. K. S. Novoselov *et al.*, Electrical field effect in atomically thin carbon films. *Science* **306**, 666 (2004).
6. J. R. Williams, L. DiCarlo, C. M. Marcus, Quantum hall effect in a gate-controlled p-n junction of graphene. *Science* **317**, 638 (2007).
7. W. Zhu, D. Neumayer, V. Perebeinos, P. Avouris, Silicon nitride gate dielectrics and band gap engineering in graphene layers. *Nano Lett.* **10**, 3572 (2010).
8. W. Han *et al.*, Tunneling spin injection into single layer graphene. *Phys. Rev. Lett.* **105**, 167202 (2010).
9. N. Tombros, C. Jozsa, M. Popinciuc, H. T. Jonkman, B. J. van Wees, Electronic spin transport and spin precession in single graphene layers at room temperature. *Nature* **448**, 571 (2007).
10. J.-H. Chen *et al.*, Charged-impurity scattering in graphene. *Nature Phys.* **4**, 377 (2008).

11. K. Pi *et al.*, Electronic doping and scattering by transition metals on graphene. *Phys. Rev. B* **80**, 075406 (2009).
12. K. M. McCreary *et al.*, Effect of cluster formation on graphene mobility. *Phys. Rev. B* **81**, 115453 (2010).
13. C. Jang *et al.*, Tuning the effective fine structure constant in graphene: Opposing effects of dielectric screening on short- and long-range potential scattering. *Phys. Rev. Lett.* **101**, 146805 (2008).
14. A. C. Ferrari, Raman spectrum of graphene and graphene layers. *Phys. Rev. Lett.* **97**, 187401 (2006).
15. S. V. Morozov *et al.*, Giant intrinsic carrier mobilities in graphene and its bilayer. *Phys. Rev. Lett.* **100**, 016602 (2008).
16. M. Ishigami, J. H. Chen, W. G. Cullen, M. S. Fuhrer, E. D. Williams, Atomic structure of graphene on SiO_2. *Nano Lett.* **7**, 1643 (2007).
17. R. Verrucchi, S. Nannarone, Triode electron bombardment evaporation source for ultrahigh vacuum thin film deposition. *Rev. Sci. Instrum.* **71**, 3444 (2000).
18. L. Liu *et al.*, Graphene oxidation: Thickness-dependent etching and strong chemical doping. *Nano Lett.* **8**, 1965 (2008).
19. U. Diebold, The surface science of titanium dioxide. *Surf. Sci. Rep.* **48**, 53 (2003).
20. S. Adam, E. H. Hwang, V. M. Galitski, S. Das Sarma, A self-consistent theory for graphene transport. *Proc. Natl. Acad. Sci. U.S.A.* **104**, 18392 (2007).

Chapter 7: The Effect of Cluster Formation on Graphene Mobility[1]

Abstract:

In this section we investigate the effect of gold (Au) atoms in the form of both point-like charged impurities and clusters on the transport properties of graphene. Cryogenic deposition (18 K) of Au decreases the mobility and shifts the Dirac point in a manner that is consistent with scattering from point-like charged impurities. Increasing the temperature to room temperature promotes the formation of clusters, which is verified with atomic force microscopy. We find that for a fixed amount of Au impurities, the formation of clusters enhances the mobility and causes the Dirac point to shift back towards zero.

[1]Published as: **K. M. McCreary**, K. Pi, A. G. Swartz, Wei Han, W. Bao,C. N. Lau, F. Guinea, M. I. Katsnelson, and R. K. Kawakami, *Phys. Rev. B* **81**, 115453 (2010).

7.1 Introduction

High electronic mobility in graphene is a striking property that is crucial for many of its potential applications (*1, 2*). Therefore, understanding the mechanisms that limit the mobility of carriers in graphene is extremely important. It is also of a high conceptual interest, since transport properties of chiral massless fermions are essentially different from those of conventional charge carriers in metals and semiconductors (*3, 4*). Currently, typical mobilities are far below the mobility of electrons in graphite and it is generally assumed that extrinsic effects are the cause of this suppression. Charged impurity scattering has received the most attention (*5-9*), with the majority of studies modeling the impurities as point-like objects (1/r potential). Recently, theoretical studies considered the physical structure of the charged impurities and found that clusterization of charged impurities can be one of the most important factors influencing their scattering properties (*10*).

In this study, we utilize *in situ* transport measurements to investigate the relationship between the clusterization of charged impurities and the electronic transport in graphene. In ultrahigh vacuum (UHV), we deposit gold impurities onto the surface of graphene devices at cryogenic temperatures, which generates *n-type* doping and decreases the mobility in a manner consistent with scattering from point-like charged impurities. As the sample temperature is gradually increased up to room temperature, the increased thermal energy promotes clusterization of the gold impurities, which leads to an increase of the mobility and a decrease of the electronic doping of graphene. The increase in mobility

due to cluster formation is consistent with theoretical models (*10*) and illustrates a mechanism that plays a role in determining the electrical conductivity of graphene.

7.2 Sample Preparation

Single layer graphene is obtained through mechanical exfoliation of Kish graphite onto a SiO_2/Si(001) substrate (SiO_2 thickness of 300 nm). A suitable single layer flake is identified using optical microscopy and verified through Raman spectroscopy (*11*). Standard electron beam lithography techniques are employed to pattern the sample into a four-point probe geometry, with contacting electrodes of Au(100 nm)/Ti(10 nm). Following the completion of all fabrication steps, the graphene device is annealed in an Ar/H atmosphere at 200ºC to remove photoresist and other chemical residues (*12, 13*). The sample is then loaded into a UHV system for degassing at 90ºC. Gold impurities are deposited on the graphene surface using a thermal molecular beam epitaxy (MBE) source while the sample temperature is controlled by a variable temperature flow cryostat. Specially designed electrical probes for transport measurements allow all metal deposition and transport measurements to be performed in the same UHV chamber without transferring or changing the sample position throughout the course of the study.

7.3 Results

Both graphene and graphite are known to have high surface diffusions, promoting the clustering of materials when deposited at room temperature. Theoretical calculations of adsorption and diffusion energies suggest the deposition of gold onto a graphene surface at cryogenic temperatures will suppress the motion of the gold, minimizing the formation of clusters (*14-19*). In this study, the graphene device is cooled to 18 K in UHV prior to

measuring the gate dependent conductivity of the clean sample. Gold is then deposited at a rate of 5.0×10^{11} atoms/(cm^2 sec) in 1 sec intervals for a total of 6 sec while the temperature is held constant at 18 K. The rate of gold deposition is measured using a quartz crystal deposition monitor, and pressures remain below 7×10^{-10} torr. The additional presence of gold atoms on the surface is expected to result in charge transfer between gold and graphene as well as affect the graphene mobility without resulting in wave function hybridization (*20-22*). Following each deposition, the gate dependent conductivity is measured. The effect of gold deposition on the transport properties is displayed in Figure 7-1A. Several trends become apparent as the amount of gold

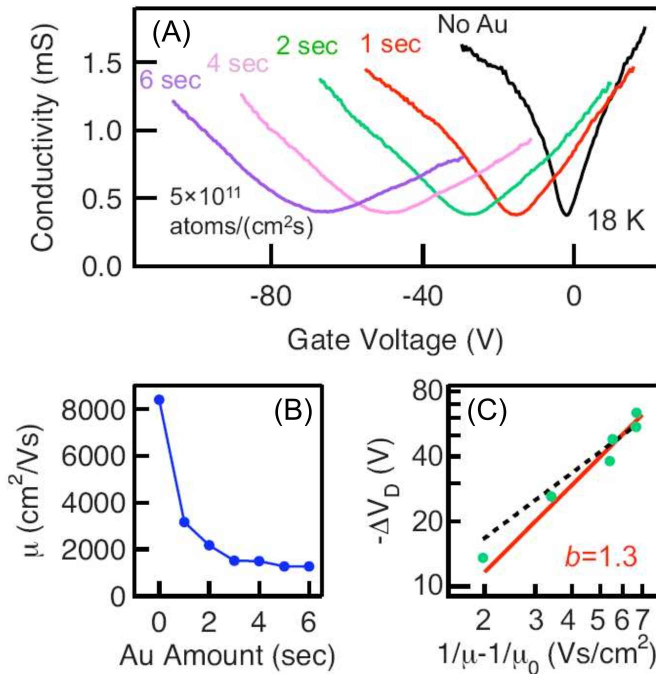

Fig 7-1 Graphene exposed to Au at 18 K (A) The gate dependent conductivity at selected values of gold deposition. (B) The mobility as a function of gold deposition. (C) $-\Delta V_D$ is plotted vs. $1/\mu - 1/\mu_0$. The solid line is the power-law fit to the equation, $-\Delta V_D \sim (1/\mu - 1/\mu_0)^b$, where b=1.3. For comparison the dashed line shows a power law with b=1.

increases. The Dirac point (V_D) shifts toward more negative voltages, indicating the transfer of electrons from gold to graphene. With increased gold concentration, the width of the minimum conductivity region increases and the conductivity curves also become more linear. In addition, the slope of the linear portion away from the Dirac point decreases, indicating a decrease in electron and hole mobility, since the mobilities ($\mu_{e,h}$) are determined using the relation $\mu_{e,h} = |\Delta\sigma/e\Delta n|$ (*5, 7*), where the carrier concentration, n, is directly related to the gate voltage, V_g, by n=-$\alpha(V_g$-$V_D)$ with α=7.2x10^{10} $V^{-1}cm^{-2}$. The average mobility values, $\mu = (\mu_e + \mu_h)/2$, are shown for the clean sample and the 6 gold depositions in Figure 7-1B and exhibit a drastic decrease upon the first deposition of gold, followed by a gradual decrease with additional gold.

To determine whether the features described are generated by scattering from point-like charged impurities (*5, 7*) or clusters (*6*), it is necessary to investigate the relationship between Dirac point shift ($\Delta V_D = V_D - V_{D,initial}$) and impurity concentration (*5, 8*). Increasing the impurity concentration (in either adatom or cluster form) will result in more scattering centers and a decreased mobility. The presence of point-like charged impurities affects the mobility through the relationship μn_{imp}=5×10^{15} $V^{-1}s^{-1}$ (*5, 8*). Using this relation and the mobility value for the clean graphene, μ_0=8390 cm^2/Vs, we find an impurity concentration of 6.0×10^{11} cm^{-2}, similar to values found for other high quality clean samples (*23*). The quantity $1/\mu - 1/\mu_0$ is therefore proportional to the impurity concentration induced by gold alone. Using the final mobility value of 1270 cm^2/Vs after 6 sec of gold deposition, it is calculated that the gold induces 3.3×10^{12} cm^{-2} impurities/cm^2, consistent with the value of 3.0×10^{12} atoms/cm^2 calculated from the

measured deposition rate of gold (previous theoretical work (*5, 8*) and calculations here assume a charge transfer of one electron per impurity adatom). The additional impurities will also result in a shift of the Dirac point through the power law relationship, $-\Delta V_D \sim (1/\mu - 1/\mu_0)^b$, with values of b=1.2-1.3 for point-like scattering ($1/r$ Coulomb potential),(*5, 8*) while scattering from clusters of material results in $b < 1.0$ (*6*). Figure 7-1C shows the data of Dirac point shift vs. $1/\mu - 1/\mu_0$ as well as the best fit line, having a coefficient b=1.3 (solid line). For comparison, the dashed line represents a power law with b=1. The experimentally measured coefficient, b, along with the similarity between measured and calculated impurity concentration indicate that gold deposited at low temperature behaves as point-like charged impurities.

Following the deposition of gold at cryogenic temperatures, the transport properties are monitored as the temperature is increased by discrete amounts until reaching room temperature. Figure 7-2A shows an increase in the mobility as the temperature is increased, and Figure 7-2B shows the corresponding change in the Dirac point. At each temperature value, the temperature is stabilized and the gate dependent conductivity is measured to determine the mobility and Dirac point voltage. To test for dynamics, the temperature is held fixed for at least 35 minutes while the transport measurement is repeated every ~8 minutes. In the range between 18 K and 210 K, we observe no time dependence of the mobility or Dirac point. Although, at higher temperatures, the mobility and Dirac point do exhibit a slow dynamics. In Figures 7-2A and 7-2B, the multiple data points at 240 K, 270 K, and near RT (292-298 K) represent the time evolution over 42 minutes, 42 minutes, and 600 minutes, respectively. Figures 7-2C and 7-2D show the

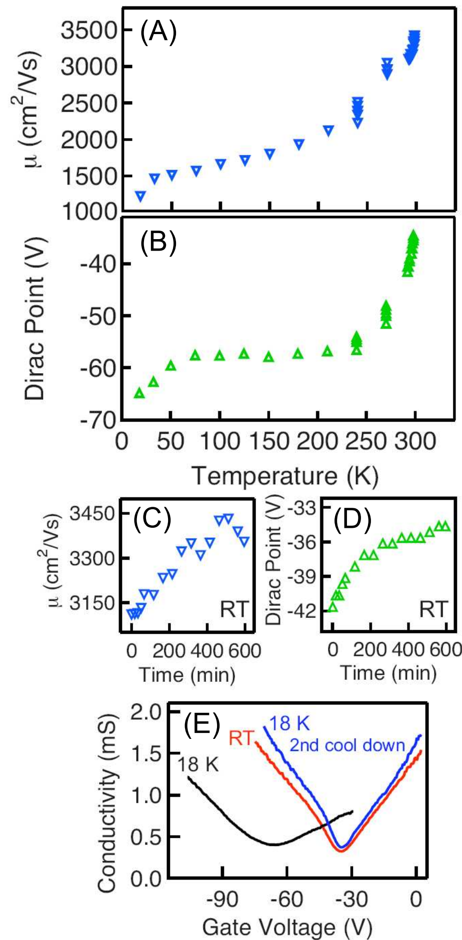

Fig 7-2 Transport properties as a function of temperature. (A) The mobility and (B) Dirac point shift are displayed as a function of temperature. Above 210 K, the mobility and Dirac point change over time at fixed temperature, indicated by the multiple data points at set temperature values. The time dependence of mobility (C) and Dirac point (D) are displayed for the sample at room temperature over a span of 10 hours. (E) A comparison of the gate dependent conductivity curves measured immediately after gold deposition at 18 K, upon warming to room temperature, and after the second cool down indicate irreversible cluster formation.

explicit time dependence of the mobility and Dirac point that continues for over 10 hours at RT.

Compared to the initial mobility value of 1270 cm^2/Vs at 18 K, the final room temperature value of 3360 cm^2/Vs is nearly three times as large. This change in mobility

is equivalent to the removal of 2.4×10^{12} impurities/cm^2. The moderate temperatures used in this study do not provide nearly enough thermal energy to result in evaporation of the gold. Hence, a more plausible explanation for the observed mobility increase involves the rearranging of impurities to form clusters. Based on theoretical predictions, for a fixed amount of impurities, the formation of large circular clusters will decrease the scattering cross section compared to that of isolated adatoms (*10*), which would manifest itself experimentally as an increase in mobility. While the mobility shows a continuous change over the measured temperature range, the Dirac point exhibits minimal change between temperature of 75 K and 210 K. This behavior in Dirac point has interesting implications for the doping due to small clusters and will be discussed in more detail later. While clean graphene is known to have minimal temperature dependence, the effect of temperature on metal doped graphene samples has not yet been investigated. To rule this factor out as the cause of the drastic change in doping and scattering observed, the sample is once again cooled. Figure 7-2E shows the gate dependent conductivity for (*i*) the initial state at 18 K immediately following the gold deposition (black curve), (*ii*) after heating to room temperature (red curve), and (*iii*) for the second cool-down to 18 K (blue curve). The minimal change observed between room temperature and 18 K during the second cool down, along with the substantial difference between the two curves measured at 18 K, indicates an irreversible change that is due to cluster formation of the gold impurities.

The time dependent properties of the transport measurement provide insight into the clusterization dynamics. At the lower temperatures (18 K – 210 K), no dynamics are observed within the resolution of the measurement (~8 min.). In this regime, the cluster

formation is limited primarily by energetics of surface diffusion (i.e. thermal energy vs. energy barrier heights). The clusterization occurs as the temperature is increased and reaches a stable state at fixed temperature within 8 minutes. On the other hand, at higher temperatures (≥240 K), the observed dynamics over long time scales implies that issues of clusterization dynamics (e.g. probability of cluster collisions, density of clusters, etc.) become more important than energetics.

Atomic force microscopy (AFM) is utilized to characterize the structure of the gold on the graphene surface. As suggested by the drastic changes in transport measurements, the gold has formed clusters of material, clearly identified in Figure 7-3A. The boundary between the substrate and SLG is identified in the figure. There is no preferential clusterization at this boundary, contrary to what has been observed at elevated

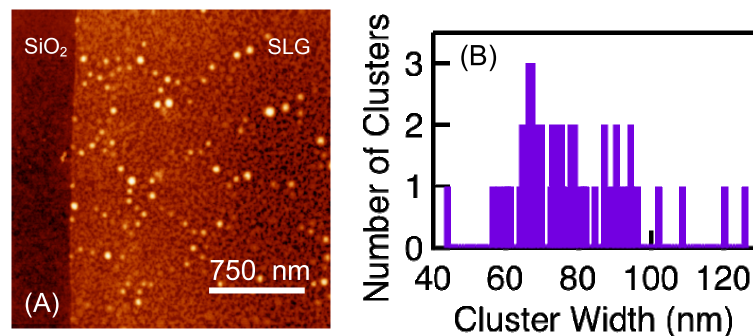

Fig 7-3 The distribution of Au on graphene at room temperature. (A) The room temperature AFM scan shows clusters of gold on the surface of graphene. (B) A histogram of cluster sizes measured in two 1.5 μm × 1.5 μm area scans.

temperatures (*16*). The circular nature of the clusters allows further comparisons between experimental data and the theoretical predications of Katsnelson *et. al.* (*10*). By modeling the behavior of charge carriers scattered from a circularly symmetric potential,

it is predicted that the scattering cross section of a large cluster ($k_F R$>1) is comparable to that of a single isolated impurity. Through further analysis of two 1.5 μm × 1.5 μm area scans, the cluster diameter is found to vary from approximately 40 to 120 nm, as seen in Figure 7-3B. From this data, we are also able to estimate a cluster density of 2.4×10^{9} cm^{-2}. Assuming a large cluster will have a similar effect on mobility as a point like scatterer, a final mobility value on the order of 8300 cm^2/Vs is expected (limited by the initial mobility of the clean device). While the observed recovery is clearly not this drastic, it is evident that the clustering has significantly reduced the scattering compared to the initial state of point like charged impurities. A distinct possibility, to account for the only moderate enhancement of mobility, is that not all the material has formed clusters. Single atoms or small clusters of several atoms are below the resolution of AFM. These isolated impurities would provide additional scattering sites, preventing the mobility from fully recovering, without being detected during the AFM measurement. In any case, the measured transport data clearly shows that for the same number of gold atoms, the effect on mobility is significantly reduced when the impurities are in the form of clusters compared to that of isolated adatoms.

While the mobility changes throughout the measured temperature range, the Dirac point shows little variation at low temperatures (< 210 K) followed by a rapid shift toward more positive values as room temperature is approached. We note that the plateau in the Dirac point data (Figure 7-2B) does not imply that the cluster formation has stopped between 70 K and 210 K; the increase of the mobility in this temperature range clearly indicates that structure of the gold clusters is changing. Rather, the plateau

structure is due to a more complicated relation between the electronic doping by clusters and the measurement of the Dirac point. A qualitative understanding of this behavior may be reached by considering the effect of large clusters in comparison to adatoms on the surface of graphene. In the case of adatoms, the graphene system is relatively homogeneous, with the carriers transferred between metal and graphene not localized to any particular region. These transferred carriers result in a large shift in the Fermi energy, as measured by the Dirac point shift. However, for large clusters, their effect on the graphene is more similar to the effect produced by metallic electrodes (*24*). In this case, the graphene can no longer be considered a homogeneous system, and is instead separated into three areas. The majority of charge transferred between the metal and graphene is confined to the region directly below an electrode, resulting in a Fermi level that is pinned and unaffected by the gate voltage. Away from the electrode, the carrier concentration is governed solely by the gate voltage. A third region exists at the edges of the electrodes, where charge diffuses away from the large concentration situated below the electrodes. In this transition region, the carrier concentration is affected by both the metal and the gate voltage. It is the presence of this transition region which results in a shift in the Dirac point. While the continually changing mobility in the collected data indicates cluster formation throughout the temperature range, the behavior of the Dirac point implies a transition between the adatom-like and electrode-like situations described above. At lower temperatures, small clusters and adatoms are unable confine carriers, resulting in a Dirac point that has been shifted greatly in comparison to that of the clean sample. Above a certain threshold (T~210 K), the clusters behave similarly to electrodes,

with some of the doping electrons confined to the region below the cluster and unaffected by gate voltage. As larger clusters continue to form, the number of confined carriers continues to increase. Under the conditions of fixed amount of gold impurities, this leads to a decrease in the number of carriers in the transition regions, causing the Dirac point to shift back towards zero. We note that the Dirac point behavior is consistent with previous studies of Pt clusters on graphene, where the Dirac point shifts toward zero at higher coverages (*6*). Therefore, in addition to the effects discussed above, the role of cluster size on the interfacial dipole strength and the equilibrium distance between the metal and graphene may have to be considered (*22, 25*).

While this provides a qualitative explanation, future experiments may be able to provide more insight into this behavior by combining transport measurements with low temperature growth and atomic resolution scanning probe microscopy.

7.4 Conclusion

In conclusion, we have shown that gold deposited at low temperature behaves as point-like charged impurities. The shift in Dirac point clearly indicates electrons are transferred from gold to graphene at submonolayer coverages. For a fixed amount of gold impurities, it is discovered that the formation of clusters significantly enhances the mobility and causes the Dirac point to shift back toward zero. The latter is attributed to the increased inhomogeneity associated with large clusters, while the former is qualitatively consistent with the theoretical prediction of reduced scattering by clustered impurities.

References:

1. A. K. Geim, K. S. Novoselov, The rise of graphene. *Nature Mater.* **6**, 183 (2007).
2. A. H. Castro Neto, F. Giunea, N. M. R. Peres, K. S. Novoselov, A. K. Geim, The electronic properties of graphene. *Rev. Mod. Phys.* **81**, 109 (2009).
3. K. S. Novoselov *et al.*, Two-dimensional gas of massless Dirac fermions in graphene. *Nature* **438**, 197 (2005).
4. Y. Zhang, J. W. Tan, H. L. Stormer, P. Kim, Experimental observation of the quantum Hall effect and Berry's phase in graphene. *Nature* **438**, 201 (2005).
5. J.-H. Chen *et al.*, Charged-impurity scattering in graphene. *Nature Phys.* **4**, 377 (2008).
6. K. Pi *et al.*, Electronic doping and scattering by transition metals on graphene. *Phys. Rev. B* **80**, 075406 (2009).
7. F. Schedin *et al.*, Detection of individual gas molecules adsorbed on graphene. *Nature Mater.* **6**, 652 (2007).
8. S. Adam, E. H. Hwang, V. M. Galitski, S. Das Sarma, A self-consistent theory for graphene transport. *Proc. Natl. Acad. Sci. U.S.A.* **104**, 18392 (2007).
9. D. S. Novikov, Elastic scattering theory and transport in graphene. *Phys. Rev. B* **76**, 245435 (2007).
10. M. I. Katsnelson, F. Guinea, A. K. Geim, Scattering of electrons in graphene by clusters of impurities. *Phys. Rev. B* **79**, 195426 (2009).
11. A. C. Ferrari, Raman spectrum of graphene and graphene layers. *Phys. Rev. Lett.* **97**, 187401 (2006).

12. S. V. Morozov *et al.*, Giant intrinsic carrier mobilities in graphene and its bilayer. *Phys. Rev. Lett.* **100**, 016602 (2008).

13. M. Ishigami, J. H. Chen, W. G. Cullen, M. S. Fuhrer, E. D. Williams, Atomic structure of graphene on SiO_2. *Nano Lett.* **7**, 1643 (2007).

14. K. T. Chan, J. B. Neaton, M. L. Cohen, First-principles study of metal adatom adsorption on graphene. *Phys. Rev. B* **77**, 235430 (2008).

15. S. Malola, H. Hakkinen, P. Koskinen, Gold in graphene: In plane adsorption and diffusion. *Appl. Phys. Lett.* **94**, 043106 (2009).

16. Y. Gan, L. Sun, F. Banhart, One- and two- dimensional diffusion of metal atoms in graphene. *Small* **4**, 587 (2008).

17. F. J. Ribeiro, J. B. Neaton, S. G. Louie, M. L. Cohen, Mechanism for bias-assisted indium mass tranport on carbon nanotube surfaces. *Phys. Rev. B* **72**, 075302 (2005).

18. G. M. Wang, J. J. BelBruno, S. D. Kenny, R. Smith, Gold adatoms and dimers on relaxed graphite surfaces. *Phys. Rev. B* **69**, 195412 (2004).

19. P. Jensen, X. Blase, P. Ordejon, First principles study of gold adsorption and diffusion on graphite. *Surf. Sci.* **564**, 173 (2004).

20. R. Varns, P. Strange, Stability of gold atoms and dimers adsorbed on graphene. *J. Phys.: Condens. Matter* **20**, 225005 (2008).

21. I. Gierz, C. Riedl, U. Starke, C. R. Ast, K. Kern, Atomic hole doping of graphene. *Nano Lett.* **8**, 4603 (2008).

22. G. Giovannetti *et al.*, Doping graphene with metal contacts. *Phys. Rev. Lett.* **101**, 026803 (2008).

23. Y.-W. Tan *et al.*, Measurement of scattering rate and minimum conductivity in graphene. *Phys. Rev. Lett.* **99**, 246803 (2007).

24. F. Xia *et al.*, Photocurrent imaging and efficient photon detection in a graphene transistor. *Nano Lett.* **9**, 1039 (2009).

25. P. A. Khomyakov *et al.*, First-principles study of the interaction and charge transfer between graphene and metals. *Phys. Rev. B* **79**, 195425 (2009).

Chapter 8: Enhancement of Spin Injection into Graphene by Water Dipping

Abstract:

We immerse single layer graphene spin valves into purified water for a short duration (<1 min) and investigate the effect on spin transport. Following water immersion, we observe an enhancement in non-local magnetoresistance. Additionally, the enhancement of spin signal is correlated with an increase in junction resistance, which produces an increase in spin injection efficiency. This study provides a simple way to improve the signal magnitude and establishes the robustness of graphene spin valves to water exposure, which enables future studies involving chemical functionalization in aqueous solution.

8.1 Introduction:

Graphene has become a promising material for spin-based electronics due to the observation of spin transport at room temperature (*1, 2*) with long spin lifetimes (*3, 4*), long spin diffusion lengths (*1*), and high spin injection efficiency (*5*). Additionally, its extreme sensitivity to surface adsorbates provides an effective method for modifying charge transport properties (*6-8*) and is predicted to induce interesting spin-dependent phenomena (*9, 10*). In particular, controlling graphene's properties using aqueous solutions for chemical functionalization is gaining interest in several fields (*11-14*). To exploit such capabilities for spintronics, it is important to establish the robustness of graphene spin valves to aqueous solution processing. In this paper, we investigate the effect of dipping graphene spin valves into ultrapure water and surprisingly find that the spin transport signal is enhanced significantly following such a process. Further studies reveal that the enhancement of spin signal is correlated with an increase of the junction resistance, which can be understood within the framework of the one-dimensional (1D) drift-diffusion model (*15*) of spin transport.

8.2 Sample Preparation:

Single layer graphene (SLG) spin valves, having cobalt electrodes with an MgO masking layer to reduce the Co/graphene contact area (*16*). are fabricated following the procedure outlined in refs. (*17, 18*). Spin transport is investigated at room temperature in the non-local spin valve geometry (*19*) as summarized in Figure 8-1A. A representative curve for the non-local resistance, R_{NL} = V/I, as a function of magnetic field, H, applied along the electrode axis is displayed in figure 8-1B, with constant background subtracted.

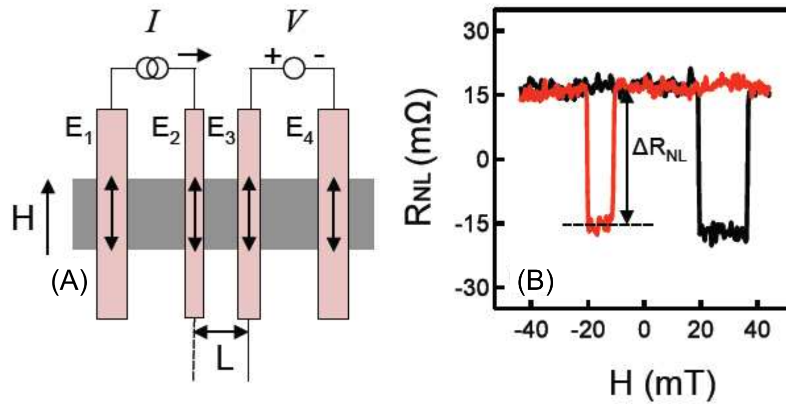

Fig 8-1 Non-local spin transport in graphene. (A) A schematic illustration of a graphene spin valve in the non-local measurement geometry. (B) Typical nonlocal magnetoresistance curves as a function of applied magnetic field. This SLG sample has a channel length of 1.5 μm and is measured at the Dirac point. The black (red) curve is for increasing (decreasing) magnetic field.

The non-local resistance difference between the parallel and antiparallel magnetization alignments of electrodes E_2 and E_3 is defined as ΔR_{NL}. This represents the signal due to spin transport in the graphene from the spin injector (E_2) to the spin detector (E_3).

8.3 Results

Prior to immersion in water, the graphene conductivity (σ) and ΔR_{NL} are characterized as a function of gate voltage (V_G), as shown in Figure 8-2A. The minimum in σ identifies the Dirac point, V_D, at 5 V for sample 1. The electron density is given by $n = \alpha(V_G - V_D)$, with $\alpha = 7.2\times10^{10}$ cm^{-2}/V and negative values of n corresponding to hole densities (*6*). The spin signal, ΔR_{NL}, is roughly proportional to σ, which can be understood by the 1D drift-diffusion model of spin transport (*15*). In the limit of small but non-zero interface resistance, the spin signal is given by

$$
\begin{aligned}
\Delta R_{NL} &= F_{el} F_{gr} \sigma \\
F_{el} &= 4\left(\frac{p_F R_F}{1-p_F^2} + \frac{p_J R_J}{1-p_J^2}\right)^2 \\
F_{gr} &= \frac{W}{\lambda_s}\left(\frac{e^{(-L/\lambda_S)}}{1-e^{(-2L/\lambda_S)}}\right)
\end{aligned}
\qquad (8\text{-}1)
$$

where W is the width of the graphene, L is the spacing between injector (E_2) and detector (E_3), λ_S is the spin diffusion length in the SLG, R_J is the interfacial resistance between the Co and SLG, p_J is the spin-asymmetry of the interfacial resistance, R_F is the spin-resistance of the cobalt, and p_F is the spin-asymmetry of the bulk Co resistivity. Equation (8-1) shows that ΔR_{NL} is proportional to σ, with the proportionality coefficient depending on the properties of the Co electrodes (F_{el}) and the spin diffusion in graphene (F_{gr}). This equation is valid in the limit of R_J, $R_F << \lambda_S/\sigma W$. Possible variations in λ_S with electron density could produce a complicated relationship in the ΔR_{NL} vs. V_G curve (through changes in F_{gr}), but the experimental results in Figure 8-2A indicate this is not a strong effect.

To investigate the effect of water immersion on the spin transport properties, we submerge the spin valves in ultrapure water for approximately 5 seconds (unless otherwise noted) then quickly dry the devices under a flow of nitrogen gas. The water is prepared by filtration in a Millipore system, which yields a high resistivity of 18.2 MΩ-cm and a pH value between 5.70 and 5.85.

Figure 8-2B shows ΔR_{NL} as a function of gate voltage before and after the water dip for sample 1. Surprisingly, the water dipping enhances the spin signal by a factor of over 6. We compare σ before and after the water dip as shown in Figure 8-2C and find that

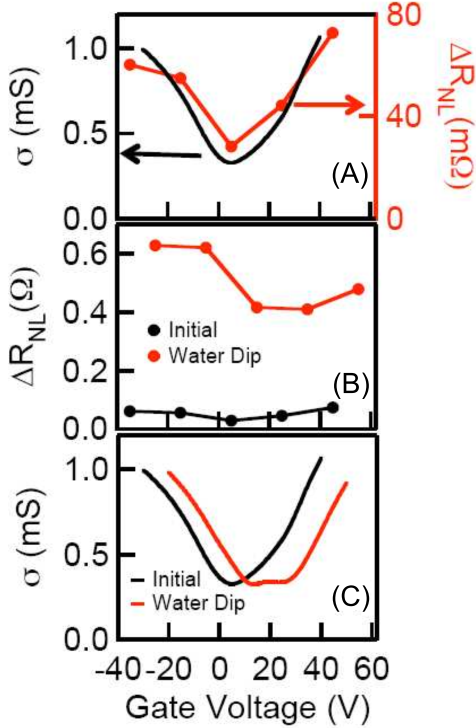

Fig 8-2 Spin transport following water exposure. (A) The conductivity (solid line) and ΔR_{NL} (circles) as a function of gate voltage on sample 1 (with L= 2 μm), measured prior to water exposure. (B,C) ΔR_{NL} and σ are compared before and after water immersion. ΔR_{NL} increases by at least a factor of six following water immersion, which cannot be attributed to the changes observed in conductivity.

although there are some minor changes in σ, it is clearly unable to explain the large enhancement of ΔR_{NL}. In all devices showing an enhanced ΔR_{NL}, the effect cannot be attributed to a corresponding enhancement of σ. This type of enhancement has been observed on 9 of 11 devices studied.

To investigate the origin of the enhanced spin signal, we turn our attention to the other factors in equation 1, namely F_{gr} and F_{el}. F_{gr} describes the spin diffusion from the injector electrode to the detector electrode with characteristic decay length of λ_S ($\lambda_S = \sqrt{D\tau_S}$ where D is the electron diffusion coefficient and τ_S is the spin lifetime).

Even though the water dip does not substantially change the charge transport properties, namely σ and D, the spin diffusion length could increase if the water significantly increases τ_S. As shown in Figure 8-3A based on equation 1, when R_J is held at 250 Ω, increasing λ_S results in an enhancement of ΔR_{NL}, which saturates as λ_S becomes larger than L. All other parameters are specified in the figure captions. We note that further enhancement of ΔR_{NL} can occur if λ_S exceeds the size of the graphene flake (*20, 21*).

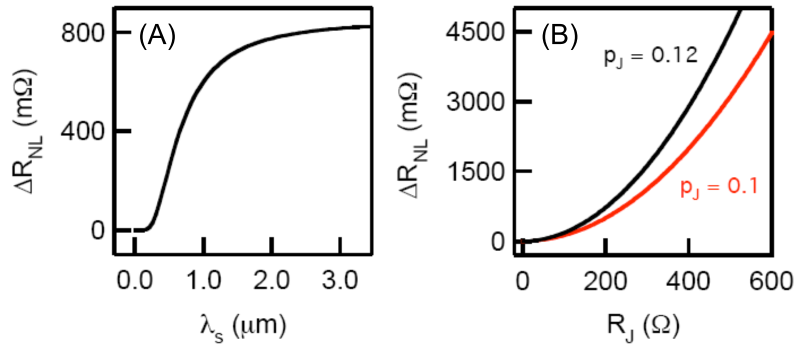

Fig 8-3 Nonlocal magnetoresistance based on equation 1 using typical values of W=2 μm, L=1.5 μm, σ=0.5 mS, p_F=0.4, R_F=2.2×10^{-2} Ω (ρ_{Co}=5.8×10^{-8} Ωm, λ_S^{Co}=38 nm, A_J=0.1 μm^2). (A) The dependence of ΔR_{NL} on λ_S while R_J is held constant at 250 Ω and p_J = 0.1. (B) The dependence of ΔR_{NL} on R_J while λ_S is held constant at 2 μm. The two curves are for values of p_J=0.1 and 0.12.

Another factor in determining ΔR_{NL} is F_{el}, which is related to the electronic and spin-dependent properties of the electrodes and their interface with the graphene. The first term of F_{el} in equation (8-1) depends on bulk properties of Co (p_F, λ_S^{Co}) that should not change with water dipping. Water dipping is more likely to affect the second term of F_{el}, which describes the interfacial properties of the junctions. The two important parameters are p_J and R_J, which could be affected by the water dip. To illustrate the dependence of ΔR_{NL} on p_J and R_J, Figure 8-3B shows ΔR_{NL} as a function of R_J while keeping λ_S and p_J

fixed at typical values. The two curves correspond to p_J values of 0.1 and 0.12. As apparent in the plot, an increase in R_J can result in a substantial enhancement of ΔR_{NL}.

In order to investigate the source of the observed magnetoresistance enhancement, we study several more devices in which close attention is paid to both the junction resistance and ΔR_{NL}. To monitor the junction resistance, a three probe differential resistance (dV/dI) measurement is performed. In this geometry, the resistance of electrode E_2 is measured by applying a DC current plus AC modulation from E_1 to E_2 while measuring the voltage difference between E_3 and E_2 as the DC current is varied. Because the measured differential resistance R_{el} includes not just R_{J} but also the cobalt resistance, wire bond resistance, and the resistance of the measurement system we keep the wire bonds intact throughout the study including during the dip.

We find that the water dipping produces an increase in R_{el} in a majority of samples. Furthermore, the enhancement of ΔR_{NL} was observed only in samples that also show an increase of R_{el}. The correlation between changes in R_{el} and ΔR_{NL} is best illustrated in a particular device (sample 2) that was submerged in water twice. In a first dip, the ΔR_{NL} was not significantly affected, as can be seen by comparing the black (initial sample) and red (dip #1) curves in figure 8-4B. The small increase in the ΔR_{NL} on the electron side of the Dirac point is attributed to the change in conductivity resulting from the water dip, as seen in figure 8-4B. Additionally, the first dip had no effect on the electrode resistance, as indicated by the overlap of initial (solid black) and water dipped (dashed red) curves in figure 8-4C. A second extended dip of ~50 sec was performed on the same sample. Following this dip, the ΔR_{NL} increased by more than 60% as shown in Figure 8-4A. The

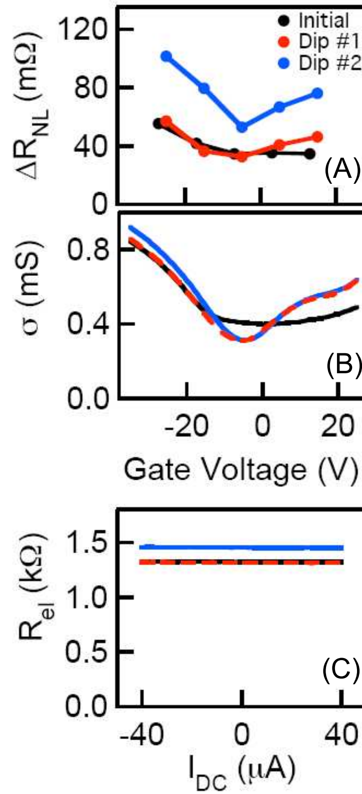

Fig 8-4 Investigating the source of the observed magnetoresistance enhancement. (A-C) ΔR_{NL}, σ, and differential resistance R_{el}, respectively, before water immersion (black, solid) and after dip #1 (red, dashed) and dip #2 (blue, solid) for sample 2 having L=1.5 μm. The first dip has little effect on ΔR_{NL} and R_{el}, with the black and red R_{el} curves completely overlapped. Following dip #2, the ΔR_{NL} in enhanced by at least 60%, and R_{el} increases from 1315 Ω to 1454 Ω. The constant bias dependence of R_{el} indicates an ohmic contact.

gate dependent conductivity curves before and after the extended dip are nearly identical, as can be seen in Figure 8-4B, whereas the R_{el} shows an increase from 1315 Ω to 1454 Ω. This sample highlights both situations we have observed as a result of exposure to water: either the ΔR_{NL} is enhanced and R_{el} increases, or ΔR_{NL} remains largely unchanged and no change in R_{el} is observed.

As discussed earlier, based on theoretical considerations, the possible explanations for the enhancement of ΔR_{NL} are increases in λ_S, p_J and/or R_J. While changes to λ_S and p_J

may be present (and certainly cannot be ruled out), the observed correlation between R_{el} and ΔR_{NL} due to water dipping provides strong evidence that an increase of R_{J} is the important factor for producing the enhanced spin signal. Furthermore, the relationship between increasing R_{J} and ΔR_{NL} has been established experimentally in related studies on tunneling spin injection, where R_{J} was intentionally increased by inserting tunnel barriers into the Co/graphene interface (*5*). Further work is needed to understand the microscopic origin of the enhancement of R_{J} due to water dipping.

8.4 Conclusion

In conclusion, we have demonstrated that dipping graphene spin valves in ultrapure water can enhance the non-local spin signal. Further studies provide evidence that an increase in the junction resistance is the most important factor for the enhancement of the spin signal, which can be understood within the 1D drift-diffusion model of spin transport. This could be useful in future device fabrication as a simple way to improve the signal magnitude. More importantly, it establishes the robustness of graphene spin valves to water dipping, which enables future studies of chemical functionalization in aqueous solution.

References:

1. N. Tombros, C. Jozsa, M. Popinciuc, H. T. Jonkman, B. J. van Wees, Electronic spin transport and spin precession in single graphene layers at room temperature. *Nature* **448**, 571 (2007).
2. S. Cho, Y.-F. Chen, M. S. Fuhrer, Gate-tunable graphene spin valve. *Appl. Phys. Lett.* **91**, 123105 (2007).
3. T.-Y. Yang *et al.*, Observation of long spin-relaxation times in bilayer graphene at room temperature. *Phys. Rev. Lett.* **107**, 047206 (2011).
4. W. Han, R. K. Kawakami, Spin relaxation in single-layer and bilayer graphene. *Phys. Rev. Lett.* **107**, 047207 (2011).
5. W. Han *et al.*, Tunneling spin injection into single layer graphene. *Phys. Rev. Lett.* **105**, 167202 (2010).
6. K. Pi *et al.*, Electronic doping and scattering by transition metals on graphene. *Phys. Rev. B* **80**, 075406 (2009).
7. J.-H. Chen *et al.*, Charged-impurity scattering in graphene. *Nature Phys.* **4**, 377 (2008).
8. F. Schedin *et al.*, Detection of individual gas molecules adsorbed on graphene. *Nature Mater.* **6**, 652 (2007).
9. B. Uchoa, A. H. Castro Neto, Superconducting states of pure and doped graphene. *Phys. Rev. Lett.* **98**, 146801 (2007).
10. B. Uchoa, V. N. Kotov, N. M. R. Peres, A. H. Castro Neto, Localized magnetic states in graphene. *Phys. Rev. Lett.* **101**, 026805 (2008).

11. P. K. Ang *et al.*, A bioelectronic platform using a graphene-lipid bilayer interface *ACS Nano* **4**, 7387 (2010).

12. Y. Ohno, K. Maehashi, Y. Yamashiro, K. Matsumoto, Electrolyte-dated graphene field effect transistors for detecting pH and protein adsorption. *Nano Lett.* **9**, 3318 (2009).

13. J. Hong *et al.*, Effect of nitrophenyl functionalization on the magnetic properties of epitaxial graphene. *Small*, doi: 10.1002/smll.201002244 (2010).

14. M. Dankerl *et al.*, Graphene solution-gated field effect transistor array for sensing applications. *Adv. Funct. Mater.* **20**, 3117 (2010).

15. S. Takahashi, S. Maekawa, Spin injection and detection in magnetic nanostructures. *Phys. Rev. B* **67**, 052409 (2003).

16. T. Kimura, Y. Otani, J. Hamrle, Enhancement of spin accumulation in a nonmagnetic layer by reducing junction size. *Phys. Rev. B.* **73**, 132405 (2006).

17. W. Han *et al.*, Electrical detection of spin precession in single layer graphene spin valves with transparent contacts. *Appl. Phys. Lett.* **94**, 222109 (2009).

18. W. Han *et al.*, Electron-hole asymmetry of spin injection and transport in single-layer graphene. *Phys. Rev. Lett.* **102**, 137205 (2009).

19. M. Johnson, R. H. Silsbee, Interfacial charge-spin coupling: injection and detection of spin magnetization in metals. *Phys. Rev. Lett.* **55**, 1790 (1985).

20. H. Jaffres, J.-M. George, A. Fert, Spin transport in multiterminal devices: Large spin signals in devices with confined geometry. *Phys. Rev. B. (R)* **82**, 140408 (2010).

21. H. Dery, L. Cywinski, L. J. Sham, Lateral diffusive spin transport in layered structures. *Phys. Rev. B. (R)* **73**, 041306 (2006).

Chapter 9: Direct Detection of Magnetic Moment Formation in Graphene

Abstract:

Many fascinating predictions have been made regarding magnetism in graphene including the formation of magnetic moments from dopants, defects, and edges (*1-9*). While several experimental techniques provide insight into this problem (*10-22*), lack of direct evidence for magnetic moment formation hinders development of this nascent field. In this chapter, we report a new and unique approach to conclusively demonstrate the formation of magnetic moments in graphene resulting from the introduction of atomic hydrogen adsorbates or lattice vacancies. Through *in situ* spin transport measurements on graphene spin valves, we observe unambiguous signatures of magnetic moments through their scattering of pure spin currents. These signatures are absent in pristine graphene and emerge when atomic hydrogen or vacancies are controllably introduced under ultrahigh vacuum conditions, providing clear evidence that both types of point defects generate magnetic moments in graphene. These results provide a foundation for magnetism in graphene and open the door to exciting future studies of gate tunable magnetism (*5*), Kondo effect (*20*), edge induced magnetism (*6-9, 18*), and magnetic nanoribbons (*23*).

9.1 Introduction

Previous experimental studies utilizing bulk magnetometry (*10-18*), charge transport (*19-21*), and scanning tunneling microscopy (STM) (*18, 22*) have provided interesting and provocative results, but are subject to limitations. Bulk magnetometry directly measures magnetic properties, but since it measures the total magnetic moment, it cannot distinguish the origin of the signal. This makes it difficult to rule out artifacts from environmental magnetic impurities. Transport and STM measurements locally probe the graphene, but so far these measurements have been charge-based, so data are subject to various interpretations. The method introduced in this paper utilizes spin transport to combine the beneficial aspects of magnetometry and transport measurements, and achieves direct detection of magnetic moments in graphene by probing their intrinsic spin degree-of-freedom.

9.2 Results

For a systematic investigation, the entire experiment is performed in an ultrahigh vacuum (UHV) chamber equipped with an atomic hydrogen source, Ar-sputtering gun to create vacancies, and spin transport measurement capability. The spin transport measurement is first performed on a pristine single layer graphene (SLG) spin valve as a control measurement. Then dopants/defects are controllably introduced to the SLG and the spin transport experiment is repeated. The sample is never exposed to air during the entire process. Therefore, observed signatures of magnetic moment formation are caused by the adsorbed hydrogen or lattice vacancies introduced in UHV.

Experiments are performed on non-local SLG spin valves (*24-26*) (Fig. 9-1A) consisting of two outer Au/Ti electrodes (*a* and *d*) and two ferromagnetic (FM) Co electrodes that make contact to SLG across MgO/TiO_2 tunnel barriers (*b* and *c*). The tunnel barrier is present only at the site of the FM electrodes, leaving the rest of thee graphene uncovered. The device is fabricated on a SiO_2/Si substrate (300 nm thickness of SiO_2) where the Si is used as a global back gate to tune the carrier density. Details of device fabrication are published elsewhere (*26*).

The charge and spin transport properties of pristine SLG spin valves are measured at 15 K using standard lock-in techniques. The gate dependent resistivity (ρ_G) of a representative sample A (black curve in Fig 9-1B) exhibits a maximum at the gate voltage (V_G) of 0 V, which defines the Dirac point (V_D= 0 V). This sample exhibits mobility (μ) of 6105 cm^2/Vs (*27*). To investigate spin transport in the SLG device (Fig 9-1A), a current (*I*) is applied between electrodes *b* and *a*, injecting spin-polarized carriers into graphene directly below the FM injector, *b*. The spin population diffuses along the sample (*x*-axis) and the spin density is measured at the FM spin detector, *c*, as a voltage difference (*V*) between electrodes *c* and *d*. An applied magnetic field ($B_{app,y}$) along the electrode magnetization direction (*y*-axis) is used to control the relative orientation of spin injector and detector magnetizations. For parallel alignment, the measured non-local resistance ($R_{NL}=V/I$) is positive whereas for antiparallel alignment R_{NL} is negative. The non-local spin signal ΔR_{NL}, defined as the difference between parallel and antiparallel states ($\Delta R_{NL} = R_{NL}^{P} - R_{NL}^{AP}$), is a measure of the spin density reaching the detector electrode *c*. A typical scan of R_{NL} as a function of $B_{app,y}$ (Fig. 9-1C) displays discrete

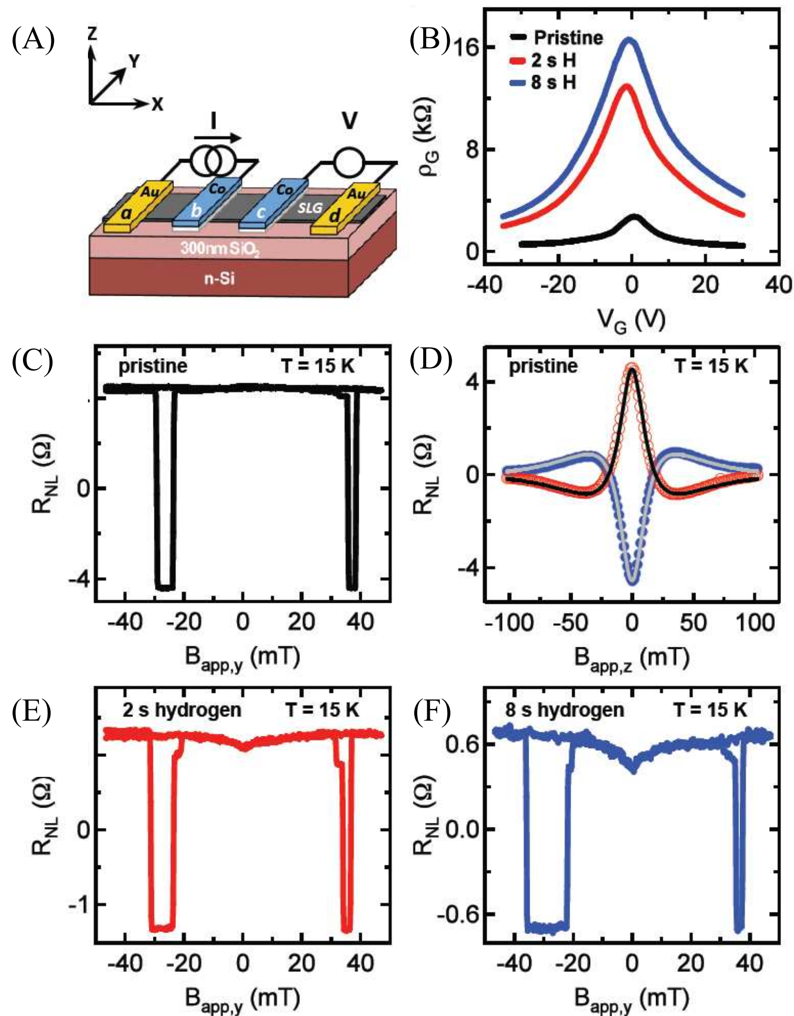

Fig 9-1 The effect of hydrogen exposure on charge and spin transport in SLG at 15 K. (A) Schematic illustration of the non-local spin valve geometry having Au/Ti outer electrodes (*a*and *d*) and Co inner electrodes (*b* and *c*) which serve as spin injector and detector. A Ti/MgObarrier (depicted in white) is present between the Co electrodes and graphene layer. Spin polarized carriers are injected into graphene directly below the FM injector, *b,* by the application of current between electrodes *a* and *b*. The injected spin population diffuses from the injector, *b*, along the *x*-axis to the detector, electrode *c*. The spin density is measured as a voltage difference between electrodes *c* and *d*. (B) Gate dependent ρ_G for the pristine graphene (black) and following exposure to atomic hydrogen for 2 s (red) and 8 s (blue). (C) Non-local spin transport measurement for pristine graphene. (D) Hanle spin precession measurement on pristine graphene. Fits to the Hanle data yield τ^{so} = 479 ps and D = 0.023 m^2/s. (E and F) Non-local spin transport measurements after atomic hydrogen exposure for 2 s and 8 s, respectively. Both curves exhibit a dip in R_{NL} at zero applied field, which is caused by increased relaxation of the spin current by an exchange interaction and is the clear signature of magnetic moment formation.

jumps as the electrode orientation changes between parallel and antiparallel. This sample exhibits a ΔR_{NL} of 8.8 Ω (sample A with $V_G - V_D$ = -15 V). A constant spin-independent background is subtracted from all R_{NL} data presented in this study. Spin precession measurements (Fig. 9-1D) are performed in order to determine the spin lifetime (τ^{so}) and diffusion coefficient (*D*). The magnetic field is applied out-of-plane, in the *z*-direction, ($B_{app,z}$) which induces spin precession, reducing the overall spin polarization. The red (blue) data corresponds to the parallel (antiparallel) states of the injector and detector. Fitting the precession data (grey curves in Fig. 9-1D) to the Hanle equation (*25, 26*)

$$R_{NL} = S\int_0^{\infty} \frac{1}{\sqrt{4\pi Dt}} e^{(-L^2/4Dt)} \cos\left(\frac{g_e \mu_B}{\hbar} B_{app,z} t\right) e^{(-t/\tau^{so})} dt \tag{9-1}$$

yields values of τ^{so} = 479 ps, D = 0.023 m^2/s and a spin diffusion length of $\lambda = \sqrt{D\tau^{so}}$ = 3.3 μm. It should be noted that in the case of pristine graphene, the longitudinal spin relaxation (τ_1^{so}) and transverse spin relaxation (τ_2^{so}) due to spin orbit coupling are equivalent ($\tau_1^{so} = \tau_2^{so} = \tau^{so}$) (*25*).

The interfacial spin polarization, P_J, is determined by fitting the The R_{NL} data for the pristine graphene (Fig 9-1C) to the drift-diffusion equation (*28*) describing spin transport in graphene, as displayed below in (9-2)

$$R_{NL}^{(P/AP)} = (+/-)2R_G e^{-L/\lambda} \prod_{i=1}^{2}\left(\frac{P_J \frac{R_i}{R_G}}{1-P_J{}^2} + \frac{P_F \frac{R_F}{R_G}}{1-P_F{}^2}\right) \times \left[\prod_{i=1}^{2}\left(1 + \frac{2\frac{R_i}{R_G}}{1-P_J{}^2} + \frac{2\frac{R_F}{R_G}}{1-P_F{}^2}\right) - e^{-2L/\lambda}\right]^{-1} \tag{9-2}$$

In the above equation, R_G is the graphene spin resistance defined by, $R_G = \rho_G \lambda / w$, where ρ_G is the resistivity and w is the graphene width. $R_{1,2}$ denotes the contact resistances of injector and detector electrodes, P_F is the ferromagnetic electrode spin polarization (assumed to be 0.35 for cobalt), and $R_F = \rho_F \frac{\lambda_F}{l_j w}$ is the spin resistance of the ferromagnet, where $\rho_F = 5.8\times10^{-8}$ Ωm is the resistivity of cobalt, l_j = 50 nm is the effective spin injector contact length of the ferromagnetic electrode and is determined by the fabrication procedures (see reference (*26*) for details), and lastly, λ_F is the spin diffusion length of the ferromagnet, taken to be 38 nm in cobalt. The measured ΔR_{NL}=8.8 Ω for Sample A (Fig. 9-1C) corresponds to a P_J=20% for parameters λ=3.3 μm, ρ_G=898 Ω, w = 2.3 μm, R_1=15.76 kΩ, and R_2=4.00 kΩ. The contact resistances are measured in a three terminal geometry (*29*) and are found to be unaffected by hydrogen exposure. The measured value of 20% interfacial spin polarization is comparable to previously reported values for efficient spin injection into SLG through tunneling contacts(*29*). P_J is assumed to remain constant throughout hydrogen exposure, a reasonable assumption since the graphene at the site of spin injection is protected by the electrode and contact resistances remain unchanged.

Atomic hydrogen is introduced to spin valve devices at 15 K at a chamber pressure of 1×10^{-6} torr using a commercial Omicron source. Diatomic hydrogen is cracked inside a tungsten capillary tube that is heated by electron bombardment. The amount of hydrogen introduced to the chamber is controlled via a leak valve, which is tuned to maintain a chamber pressure of 1×10^{-6} torr (the base pressure of the chamber is below 1×10^{-9} torr).

The heating power of the Omicron source is determined by the high voltage (HV) applied to the capillary and the emission current between capillary and filament (I_{em}). We use the parameters HV= 1kV and I_{em}= 80 mA. The distance from source to sample is 100 mm. A shutter positioned between the SLG spin valve and hydrogen source is used in order to control the exposure time. Additionally, deflector plates are used to steer any charged ions away from the sample.

Following 2 s hydrogen exposure, the gate dependent ρ_G (red curve in Fig. 9-1B) is dramatically increased. An additional 6 s of exposure (8 s total) further increases ρ_G (blue curve of Fig. 9-1B) and decreases the mobility to 495 cm^2/Vs. We obtain an order of magnitude estimate for the hydrogen concentration based upon the changes in charge transport properties assuming adsorbed hydrogen induces resonant scattering. Comparing with previous experimental work on resonant scattering in graphene via fluorine doping (*21*) and lattice vacancies (*30*), the hydrogen concentration is estimated to be on the order of 0.1%, indicating samples are in the dilute limit of hydrogen coverage.

Accompanying the changes in charge transport are also changes in spin transport. Figures 9-1E and 9-1F display R_{NL} of sample A at V_G-V_D = -15 V as a function of $B_{app,y}$ following 2 s and 8 s of exposure, respectively. The initial ΔR_{NL} of 8.8 Ω is reduced to 2.6 Ω after 2 s of hydrogen exposure and further reduced to 1.4 Ω after 8 s. Interestingly, the R_{NL} scans exhibit a dip centered at zero applied field. The dip in R_{NL} is prevalent for both up and down sweeps of $B_{app,y}$ at all measured gate voltages and has been reproduced on multiple samples following hydrogen exposure. The ratio of the dip magnitude to

ΔR_{NL} is found to increase with increasing hydrogen exposure (comparing Fig. 9-1E and 9-1F), indicating the dip feature is dependent on the amount of adsorbed hydrogen.

To understand the origin of the dip in R_{NL}, we re-examine equation (9-2), the drift-diffusion equation for spin transport. This equation shows that the spin density at the detector electrode depends on both charge and spin properties. Thus, magnetic field dependent changes to the graphene resistivity could in principle produce variations in R_{NL}. To investigate this possibility in hydrogen-doped graphene, gate dependent ρ_{G} measurements are performed on sample B at three distinct in-plane magnetic fields (Fig. 9-2A). The three curves are indistinguishable, showing that the applied magnetic field has no effect on the measured ρ_{G} of hydrogen-doped samples. Therefore, the dip in R_{NL} does not originate from field-dependent changes in charge transport. Next, we perform minor loop analysis on sample B (Fig. 9-2B) by reversing the magnetic field sweep immediately after the first magnetization reversal. The inversion of the dip in the antiparallel state (red curve) proves that the dip is due to increased spin relaxation at low fields.

We investigate the possibility that the observed dip in the non-local resistance originates from hyperfine coupling between conduction electrons and nuclear spins. In graphene, this scenario is unlikely due to the small abundance of intrinsic nuclear spins in carbon (>98% of carbon is ^{12}C, which has no nuclear spin) and a lack of contact hyperfine coupling in the p_z-orbitals that make up the conduction and valence bands. Nevertheless, investigating the situation is necessary because the adsorption of hydrogen on graphene may alter the hyperfine coupling. Two effects that could in principle alter

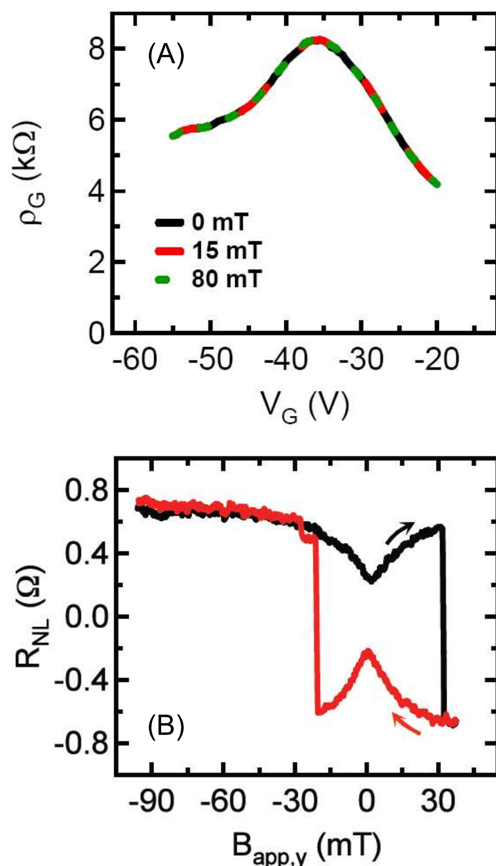

Fig 9-2 Investigating the source of the dip measured in R_{NL}.(A) Gate-dependent ρ_G of SLG after hydrogen exposure measured at several discrete in-plane applied magnetic fields. The applied field has no effect on the charge transport behavior on the graphene device. (B) Minor loop scan. For parallel alignment (black) of injector and detector electrodes, the R_{NL} exhibits a dip at $B_{app,y}$= 0 mT, whereas for antiparallel alignment (red) a peak is measured. This verifies that the low field behavior is due to increased spin relaxation, as opposed to an artifact of the background level.

the non-local resistance include hyperfine coupling to dynamically polarized nuclear spins (*31, 32*) and organic magnetoresistance (OMAR) (*33, 34*).

The effect of OMAR has previously been observed in carbon C_{60} and functionalized carbon-based polymers (*33, 34*). OMAR originates from hyperfine induced spin mixing between singlet and triplet states and manifests itself as a magnetic field dependent resistivity. However, as shown in Fig. 9-2A, resistivity does not change as a function of

applied in-plane magnetic field. This confirms OMAR is not responsible for the observed dip in R_{NL}.

The effect of dynamic nuclear polarization (DNP) was demonstrated clearly by Salis *et al (32)* and Chan *et al.* (*31*) who investigated GaAs non-local spin valves at low temperatures. Specifically, Salis *et al.* observed a dip in R_{NL} at zero applied magnetic field, similar to the dip we observe in hydrogen-doped graphene. They attributed their dip to precessional spin dephasing caused by hyperfine coupling to dynamically polarized nuclear spins. To determine whether such nuclear spin effects are present in hydrogen-doped graphene we perform a series of tests.

Test 1*:* Nuclear spin relaxation times are typically long (~minutes), and therefore, slow dynamics at this time scale are a characteristic of effects related to DNP. This is manifested in non-local spin transport data as a “lab time” dependence *(32)*. In our investigation of hydrogen-doped graphene, we do not observe a lab time dependence or a magnetic field ramp rate dependence.

Test 2*:* A characteristic feature of hyperfine coupling to the nuclear spin bath through DNP is the nuclear field’s linear dependence on the applied field (*32*). Specifically, at zero field the nuclear spin bath depolarizes slowly over time. The depolarization of the nuclear spin bath is evident in R_{NL} data as the gradual decrease and eventual disappearance (after a few minutes) of the dip when the applied field is set to zero (Figure 1 of Salis *et al.* (*32*)). We perform this test on hydrogen-doped graphene spin valves, as shown in Fig. 9-3. First, the magnetic field is held at -30 mT for 10 minutes to ensure any possible nuclear spin

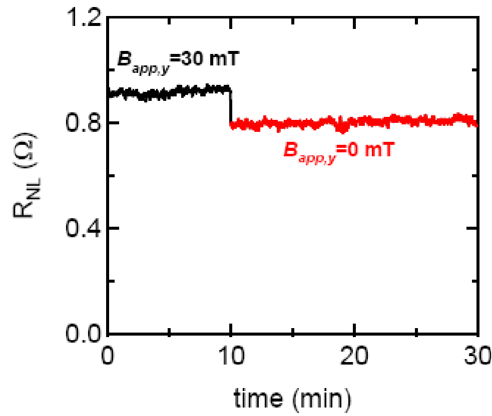

Fig 9-3 Test of nuclear spin effects. The non-local spin transport signal signal is measured for 10 mins while *Bapp,y*= 30 mT (black). This ensures any possible nuclear spins will reach steady state. The field is ramped to zero, and held constant for the following 20 mins (red). The observed response excludes hyperfine coupling to nuclear spins as the origin of the reduced spin signal at low fields.

transients reach steady state. The R_{NL} is measured continuously during this period and exhibits a value of ~0.92 Ω. Then the magnetic field is quickly reduced to zero, coinciding with the immediate drop of R_{NL} to ~0.80 Ω. This drop occurs because $B_{app,y}$= 0 mT is at the center of the dip in R_{NL}. The R_{NL} is measured over the following 20 minutes, for which the observed value remains unchanged at ~0.80 Ω. This indicates that the magnitude of the dip is independent of lab time. If the dip were due to hyperfine coupling to dynamically polarized nuclear spins, then the magnitude of the dip would gradually decrease to zero (i.e. R_{NL} would increase back to ~0.92 Ω). Because this behavior is not observed, the dip in R_{NL} cannot be due to DNP.

Test 3: For the case of DNP, applying a constant out-of-plane magnetic field during a non-local spin transport measurement (in-plane field scan) results in a

characteristic feature of nuclear depolarization and repolarization as the in-plane field crosses zero (Figure 1 of Chan *et al.* (*31*)). We perform this measurement on hydrogen-doped graphene and observe no evidence of depolarization or repolarization features. Together, these three tests show that the dip in R_{NL} is not due to hyperfine coupling to dynamically polarized nuclear spins.

The above investigations of OMAR and DNP conclusively exclude the possibility of hyperfine coupling with nuclear spins as the source of the observed dip in the non-local spin transport.

As we discuss in the following, emergence of the dip following hydrogen adsorption identifies magnetic moment formation in graphene. The dip in R_{NL} is a characteristic feature of spin relaxation from exchange coupling with localized magnetic moments, and can be illustrated from a simple textbook example of two coupled spins in a magnetic field. The Hamiltonian is given by $H = A_{ex}\vec{S}_e \cdot \vec{S}_M + g_e\mu_B\vec{S}_e \cdot \vec{B}_{app} + g_M\mu_B\vec{S}_M \cdot \vec{B}_{app}$, where $\vec{S}_e$ is the conduction electron spin, $\vec{S}_M$ is the spin of the magnetic moment, g_e and g_M are the respective *g*-factors, and A_{ex} is the exchange coupling strength. Due to the presence of the exchange coupling, the individual spins are not conserved; only the total spin $\vec{S}_{tot} = \vec{S}_e + \vec{S}_M$ is conserved. For the case where both $\vec{S}_e$ and $\vec{S}_M$ are spin-1/2, the quantum mechanical eigenstates in zero magnetic field are the well-known singlet ($\vec{S}_{tot}$= 0) and triplet ($\vec{S}_{tot}$= 1) spin states (*35*). The exchange interaction leads to a non-conservation of $\vec{S}_e$, which for hydrogen doped graphene spin valves results in a reduction of the spin density at low fields. At higher magnetic fields the Zeeman terms

dominate and the two spins decouple so that the magnitude and *z*-components of $\vec{S}_e$ and $\vec{S}_M$ become good quantum numbers, similar to the Paschen-Back effect (*35*). With increasing field, the detected spin density of the conduction electrons increases because $\vec{S}_e$ decouples from $\vec{S}_M$, leading to reduced spin relaxation . Therefore the observed dip in R_{NL} is explained qualitatively by this simple model of an exchange interaction with magnetic moments.

To quantitatively analyze the experimental data, we must consider that a conduction electron will interact with many localized magnetic moments. Thus, the terms in the Hamiltonian involving the conduction electron are given by, $H_e = \eta_M A_{ex} \vec{S}_e \cdot \langle \vec{S}_M \rangle + g_e \mu_B \vec{S}_e \cdot \vec{B}_{app} = g_e \mu_B \vec{S}_e \cdot \left(\overline{\vec{B}}_{ex} + \vec{B}_{app} \right)$ where η_M is the filling density of magnetic moments. The averaging $\langle ... \rangle$ is over the ensemble of magnetic moments and the effective field generated by the exchange interaction is $\overline{\vec{B}}_{ex} = \eta_M A_{ex} \langle \vec{S}_M \rangle / g_e \mu_B$. As the spins diffuse through the lattice they experience varying magnetic moments which results in varying Larmor frequencies. In the local frame associated with the electrons this can be described by a time-dependent, randomly fluctuating magnetic field, $\vec{B}_{ex}(t) = \overline{\vec{B}}_{ex} + \Delta\vec{B}_{ex}(t)$ with the rms value given by the time average

$$\left(\Delta B_{ex}^{rms}\right)_{\alpha}^{2} = \left\langle \left[\Delta B_{ex,\alpha}(t)\right]^{2} \right\rangle_{t} \tag{9-3a}$$

$$\left(\Delta B_{ex}^{rms}\right)^{2} = \left(\Delta B_{ex}^{rms}\right)_{x}^{2} + \left(\Delta B_{ex}^{rms}\right)_{y}^{2} + \left(\Delta B_{ex}^{rms}\right)_{z}^{2} \tag{9-3b}$$

where α is an *xyz* component index. The time scale of the fluctuation is given by a correlation time τ_c defined by

$$\left\langle \Delta \boldsymbol{B}_{ex}(t) \cdot \Delta \boldsymbol{B}_{ex}(t-t') \right\rangle_t \sim \exp\left(-t'/\tau_c\right)$$

Spin relaxation resulting from a randomly fluctuating magnetic field has been solved in the review article by Fabian, *et al*. (see section IV.B.2 of reference (*36*)). For the non-local spin signal geometry, the injected spin polarization and the applied magnetic field lie along the same axis (*y*-axis) and the spin relaxation rate is given by longitudinal spin relaxation equation IV.36 of reference (*36*). The equation is rewritten using $\omega_\alpha = g_e \mu_B \Delta B_{ex,\alpha}/\hbar$ and $\omega_0 = g_e \mu_B \overline{B}_{total}/\hbar = g_e \mu_B \left(B_{app,y} + \overline{B}_{ex,y}\right)/\hbar$ to yield,

$$\frac{1}{\tau_1^{ex}} = \frac{(\Delta B)^2}{\tau_c} \frac{1}{\left(B_{app,y} + \overline{B}_{ex,y}\right)^2 + \left(\frac{\hbar}{g_e \mu_B \tau_c}\right)^2} \tag{9-4}$$

where $(\Delta B)^2 = \left(\Delta B_{ex}\right)_x^2 + \left(\Delta B_{ex}\right)_z^2$. In other words, precession around randomly fluctuating exchange fields along the *x*- and *z*-axes induce spin relaxation. Equation (9-4) also shows that the spin relaxation is suppressed by a large applied magnetic field. Intuitively, this occurs because the precession axis is defined by the large applied field (along *y*-axis) and fluctuating fields along the *x*- and *z*-axes have very little ability to tilt the precession axis. This peak in spin relaxation at low magnetic fields produces the observed dip in R_{NL}.

Due to the presence of $\overline{B}_{ex,y}$ in equation (9-4), ferromagnetic ordering will produce a dip in R_{NL} that is centered away from zero and is hysteretic, while paramagnetic ordering

will produce a non-hysteretic dip centered at zero field. Thus, the magnetic moments measured in these experiments (Fig. 9-1E and 9-1F) are paramagnetic. For paramagnetic moments, $\overline{B}_{ex,y}$ takes the form of the Brillouin function (B_J) and is given by

$$\overline{B}_{ex,y} = \eta_M A_{ex} \langle S_{M,y} \rangle / g_e \mu_B = \eta_M A_{ex} J B_J(x) / g_e \mu_B \qquad \text{(9-5a)}$$

$$B_J(x) = \frac{2J+1}{2J} \coth\left(\frac{2J+1}{2J} x \right) - \frac{1}{2J} \coth\left(\frac{1}{2J} x \right) \qquad \text{(9-5b)}$$

where J is the total angular momentum quantum number of the magnetic moment, $x = \frac{J g_e \mu_B}{k_B T} B_{app,y}$, k_B is Boltzmann's constant, and T is temperature. For our experiments at T = 15 K, this reduces to $x = J g_e \, B_{app,y} / (22.32\text{Tesla})$. Thus, for the values of $B_{app,y}$ in our experiments $x << 1$ so that $B_J(x) \approx (J+1)x/3J$ to yield

$$\overline{B}_{ex,y} = \frac{\eta_M A_{ex} J(J+1)}{3\mu_B} \left(\frac{B_{app,y}}{22.32\text{Tesla}} \right) \qquad \text{(9-6)}$$

Thus, the total field can be written as

$$\begin{aligned} B_{total} &= B_{app,y} + \overline{B}_{ex,y} = B_{app,y} + \frac{\eta_M A_{ex} J(J+1)}{3\mu_B} \left(\frac{B_{app,y}}{22.32\text{Tesla}} \right) \\ &= \left(1 + \frac{\eta_M A_{ex} J(J+1)}{3\mu_B (22.32\text{Tesla})} \right) B_{app,y} = \frac{g_e^*}{g_e} B_{app,y} \end{aligned} \qquad \text{(9-7)}$$

where the g_e^* is the enhanced g-factor due to the presence of the exchange field. Substituting this into equation (9-4) yields the expression for spin relaxation from

paramagnetic moments in the linear regime,

$$\frac{1}{\tau_1^{ex}} = \frac{(\Delta B)^2}{\tau_c} \frac{1}{\left(\frac{g_e^*}{g_e} B_{app,y}\right)^2 + \left(\frac{\hbar}{g_e \mu_B \tau_c}\right)^2} = \frac{\frac{(\Delta B)^2}{\tau_c}\left(\frac{g_e}{g_e^*}\right)^2}{\left(B_{app,y}\right)^2 + \left(\frac{\hbar}{g_e^* \mu_B \tau_c}\right)^2} \tag{9-8}$$

which can be expressed in the general form

$$\frac{1}{\tau_1^{ex}} = \Gamma \frac{\gamma^2}{B_{app,y}^2 + \gamma^2} \tag{9-9}$$

Thus, the spin relaxation rate due to the exchange field is described by a Lorentzian curve which depends explicitly on the applied field, $B_{app,y}$, resulting in strong spin relaxation at low fields and suppressed spin relaxation at high fields.

The total longitudinal spin lifetime, T_1^{total}, of conduction electrons is dependent on both the usual spin relaxation due to spin orbit coupling (τ^{so}) and longitudinal spin relaxation from the exchange field (τ_1^{ex}), such that $\frac{1}{T_1^{total}} = \frac{1}{\tau_1^{ex}} + \frac{1}{\tau^{so}}$. This susequently affects the spin diffusion length, such that

$$\lambda = \sqrt{D T_1^{total}} = \sqrt{D\left(\frac{1}{\tau^{so}} + \frac{1}{\tau_1^{ex}}\right)^{-1}} = \sqrt{D\left(\frac{1}{\tau^{so}} + \Gamma \frac{\gamma^2}{B_{app,y}^2 + \gamma^2}\right)^{-1}} \tag{9-10}$$

The exchange field is not accounted for in the standard Hanle equation, as presented in equation (9-1), preventing direct determination of τ^{so} and D through Hanle fitting. Instead, the Einstein relation

$$D = \frac{\sigma}{e^2 \nu} \qquad (9\text{-}11)$$

is employed to obtain D for hydrogen-doped samples, where ν denotes the density of states and e is the electron charge. Assuming ν is unchanged by exposure to hydrogen, which is reasonable in the dilute limit, the diffusion coefficient of hydrogen-doped samples D_{hyd} is determined from the pristine diffusion coefficient $D_{pristine}$ and the conductivities of hydrogen-doped (σ_{hyd}) and pristine ($\sigma_{pristine}$) graphene.

$$D_{hyd} / D_{pristine} = \frac{\sigma_{hyd}}{e^2 \nu} / \frac{\sigma_{pristine}}{e^2 \nu} = \frac{\sigma_{hyd}}{\sigma_{pristine}} \qquad (9\text{-}12)$$

The change in conductivity from 1.113 mS to 0.143 mS exhibited by sample A at $V_G - V_D$ = -15 V (Fig 9-1B) following hydrogen exposure results in D_{hyd}=0.0029 m^2/s.

Determination of D is an important step, and now allows us to apply the above model to the non-local spin transport data presented in Fig. 9-1F (sample A, $V_G - V_D$ = -15 V) and fit using the non-local equation (9-2), $\lambda = \sqrt{D T_1^{total}}$, and the exchange spin relaxation equation (9-9). The resulting fit (red line in Fig. 9-4A) replicates the shape and magnitude of the dip measured in R_{NL} (black line in Fig. 9-4A). The field dependent T_1^{total} (Fig. 9-4B), exhibits a minimum of 464 ps at zero field and increases asymptotically towards τ^{so} = 531 ps for large $B_{app,y}$. The values obtained from the fit for Γ and γ are 2.73×10^8 s^{-1}, and 8.32 mT, respectively for the parameters R_F=0.019 Ω, ρ_G =6.99 kΩ R_1=15.76 kΩ, R_2=4.00 kΩ, P_J=0.20, P_F=0.35, and L=5.25 μm. The field-

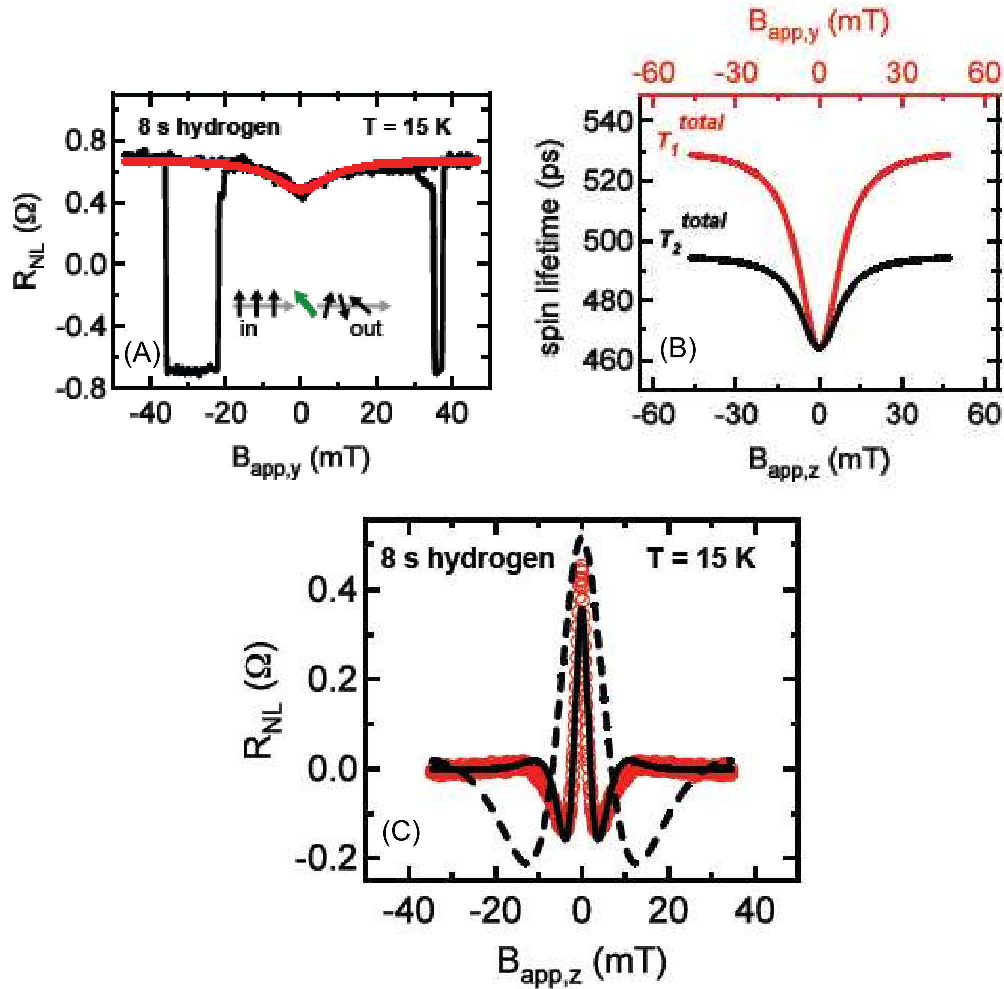

Fig 9-4 Analysis of spin transport following atomic hydrogen exposure. (A) The dip in R_{NL} after 8 s hydrogen exposure (black) is fit with a field dependent R_{NL} (red) due to the formation of paramagnetic moments. Inset: Schematic of magnetic moment detection via spin relaxation. Spin polarized conduction electrons (black) are injected into the graphene device and undergo spin relaxation due to their interaction with magnetic moments (green). (B) Field dependence of the total longitudinal spin lifetime (black) and transverse spin lifetime (red) resulting from exchange coupling to magnetic moments. (C) Hanle precession data following 8 s hydrogen exposure (red) is fit using the field dependent T_2^{total} and the model of paramagnetic impurities (solid black). For comparison, the best fit in the absence of an exchange field is displayed (black dash).

dependent spin relaxation relaxation following atomic hydrogen exposure, which emerges as a dip in R_{NL}, is a clear signature of paramagnetic moment formation.

Spin precession measurements provide further evidence for the presence of magnetic moments. Figure 9-4C shows spin precession data for sample A (8 s exposure) with FM electrodes in the parallel alignment state. The Hanle curve has considerably narrowed compared to the precession measurements obtained prior to hydrogen adsorption (Fig. 9-1D). The sharpening of the Hanle curve results from the presence of an exchange field. The injected spins precess around a total field $B_{tot} = B_{app,z} + \overline{B}_{ex,z}$ (along z-axis) that includes not only the applied field, but also the exchange field from the paramagnetic moments. To properly account for the enhanced enhanced precession by the presence of an exchange field due to magnetic moments, the Hanle equation must be modified to be

$$R_{NL} = S\int_0^{\infty} \frac{1}{\sqrt{4\pi Dt}} e^{-t/T_2^{total}} e^{-L^2/4Dt} \cos\left(\frac{g_e \mu_B}{\hbar}\left(B_{app,z} + \overline{B}_{\mathrm{ex,z}}\right)t\right) dt \quad (9\text{-}13)$$

where T_2^{total} is the transverse spin lifetime. For the Hanle geometry, the injected spin polarization is along the y-axis and the applied magnetic field is along the z-axis. In this case the spin relaxation rate is given by transverse spin relaxation equation IV.38 of reference (*36*). The equation is rewritten using $\omega_\alpha = g_e \mu_B \Delta B_{ex,\alpha} / \hbar$ and $\omega_0 = g_e \mu_B \overline{B}_{total} / \hbar = g_e \mu_B \left(B_{app,z} + \overline{B}_{ex,z}\right) / \hbar$ to yield,

$$\frac{1}{\tau_2^{ex}} = \frac{1}{2}\left[\frac{(\Delta B)^2}{\tau_c \left(\frac{\hbar}{g_e \mu_B \tau_c}\right)^2}\right] + \frac{1}{2}\left[\frac{(\Delta B)^2}{\tau_c} \frac{1}{\left(B_{app,z} + \overline{B}_{ex,z}\right)^2 + \left(\frac{\hbar}{g_e \mu_B \tau_c}\right)^2}\right] \quad (9\text{-}14)$$

where the fluctuating field is assumed to be isotropic: $(\Delta B_{ex})_x^2 = (\Delta B_{ex})_y^2 = (\Delta B_{ex})_z^2$.

For paramagnetic moments, this becomes

$$\frac{1}{\tau_2^{ex}} = \frac{1}{2}\left[\frac{\frac{(\Delta B)^2}{\tau_c}\left(\frac{g_e}{g_e^*}\right)^2}{\left(\frac{\hbar}{g_e^*\mu_B\tau_c}\right)^2}\right] + \frac{1}{2}\left[\frac{\frac{(\Delta B)^2}{\tau_c}\left(\frac{g_e}{g_e^*}\right)^2}{\left(B_{app,z}\right)^2 + \left(\frac{\hbar}{g_e^*\mu_B\tau_c}\right)^2}\right] \tag{9-15}$$

Which can be simplified to

$$\frac{1}{T_2^{total}} = \frac{1}{\tau^{so}} + \frac{\Gamma}{2}\left(1 + \frac{\gamma^2}{B_{app,z}^2 + \gamma^2}\right). \tag{9-16}$$

Comparing equations (9-9) and (9-16) it is apparent T_2^{total} is related to, but different from T_1^{total} , For comparison, T_2^{total} is plotted as the black line in Fig 9-4B. The modified Hanle equation then takes the form

$$R_{NL} = S\int_0^\infty \frac{1}{\sqrt{4\pi Dt}} e^{-t\left(\frac{1}{\tau^{so}} + \frac{\Gamma}{2}\left[1 + \frac{\gamma^2}{B_{app,z}^2 + \gamma^2}\right]\right)} e^{-L^2/4Dt} \cos\left(\frac{g_e\mu_B}{\hbar}\left(B_{app,z} + \overline{B}_{\mathrm{ex,z}}\right)t\right) dt \tag{9-17}$$

For paramagnetic moments, $B_{ex,z}$ is described by the Brillouin function. Additionally, JB_{app}/22.32Tesla <<1, so that $B_{ex,z}$ can be represented by the low field approximation.

$$\overline{B}_{ex,z} = \frac{\eta_M A_{ex} J(J+1)}{3\mu_B}\left(\frac{B_{app,z}}{22.32\text{Tesla}}\right) \tag{9-18}$$

resulting in

$$R_{NL} = S\int_0^{\infty} \frac{1}{\sqrt{4\pi Dt}} e^{-t\left(\frac{1}{\tau^{so}}+\frac{\Gamma}{2}\left[1+\frac{\gamma^2}{B_{app,z}^2+\gamma^2}\right]\right)} e^{-L^2/4Dt} \times$$

$$\cos\left(\frac{g_e\mu_B}{\hbar}\left(B_{app,z}+\frac{\eta_M A_{ex} J(J+1)}{3\mu_B}\left(\frac{B_{app,z}}{22.32\text{Tesla}}\right)\right)t\right)dt \qquad (9\text{-}19)$$

which simplifies to,

$$R_{NL} = S\int_0^{\infty} \frac{1}{\sqrt{4\pi Dt}} e^{-t\left(\frac{1}{\tau^{so}}+\frac{\Gamma}{2}\left[1+\frac{\gamma^2}{B_{app,z}^2+\gamma^2}\right]\right)} e^{-L^2/4Dt} \cos\left(\frac{g_e^*\mu_B}{\hbar} B_{app,z} t\right)dt \qquad (9\text{-}20)$$

with,

$$g_e^* = g_e\left(1+\frac{\eta_M A_{ex} J(J+1)}{3\mu_B(22.32\text{Tesla})}\right) . \qquad (9\text{-}21)$$

In equation (9-20) $\Gamma = 2.73\times10^8$ s^{-1} and $\gamma = 8.32$ mT, as determined by analysis of non-local resistance, D=0.0029 m^2/s from the Einstein relation, and L=5.25 μm. Using the field dependent T_2^{total} (Fig. 9-4B) the measured precession data (red circles of Fig. 9-4C) is fit to equation (9-20). The resulting best fit (solid black line) yields a value of g_e*=7.13.

The correlation time (τ_c) and the rms fluctuations in exchange field (ΔB) are determined by comparing equations (9-8) and (9-9) to give

$$\tau_c = \frac{\hbar}{g_e^*\mu_B}\frac{1}{\gamma} \qquad (9\text{-}22)$$

$$(\Delta B)^2 = \gamma\left(\frac{g_e^*}{g_e}\right)\left(\frac{\hbar\Gamma}{g_e\mu_B}\right) \qquad (9\text{-}23)$$

Using g_e^*=7.13 from the Hanle fit and Γ = 2.73 ×10^8 s^{-1} and γ = 8.32 mT from the non-local fit, we obtain values of τ_c= 192 ps and $(\Delta B)^2$ =4.59×10^{-5} T^2 (or $(\Delta B)=\sqrt{\Delta B_{ex,x}{}^2+\Delta B_{ex,z}{}^2}$ = 6.78 mT).

For comparison, the dashed line in Fig 9-4C shows the Hanle curve in the absence of magnetic moments. The striking difference between the two curves demonstrates the presence of an exchange field whose physical effect is to greatly enhance the spin precession frequency. The dramatic narrowing of the Hanle peak combined with the emergence of a dip in R_{NL} provides direct and unambiguous evidence for the formation of magnetic moments in graphene due to the adsorption of atomic hydrogen.

We now turn our attention to lattice vacancy defects in graphene. Several theoretical works suggest the similarity of magnetism due to vacancies and hydrogen-doping (*1, 4*), as both should create magnetic moments in graphene due to the removal/hybridization of p_z orbitals. It is therefore reasonable to expect that similar effects will be observable in graphene spin transport following the introduction of lattice vacancies. To induce vacancies on pristine SLG spin valves, *in situ* Ar-sputtering is performed at a sample temperature of 15 K. Argon partial pressures of 1×10^{-6} torr and energies between 100 eV and 500 eV combined with short sputtering times (several seconds) produce dilute lattice vacancies. Prior to exposure to Ar-sputtering, the SLG device exhibits a ΔR_{NL} of 38.9 Ω at V_G-V_D=20 V and displays no dip in non-local resistance at zero applied field (Fig. 9-5A). Fitting of the corresponding precession data (inset of Fig. 9-5A) results in values of τ^{so}= 859 ps and D=0.023 m^2/s for the pristine SLG device. The black (red) curve

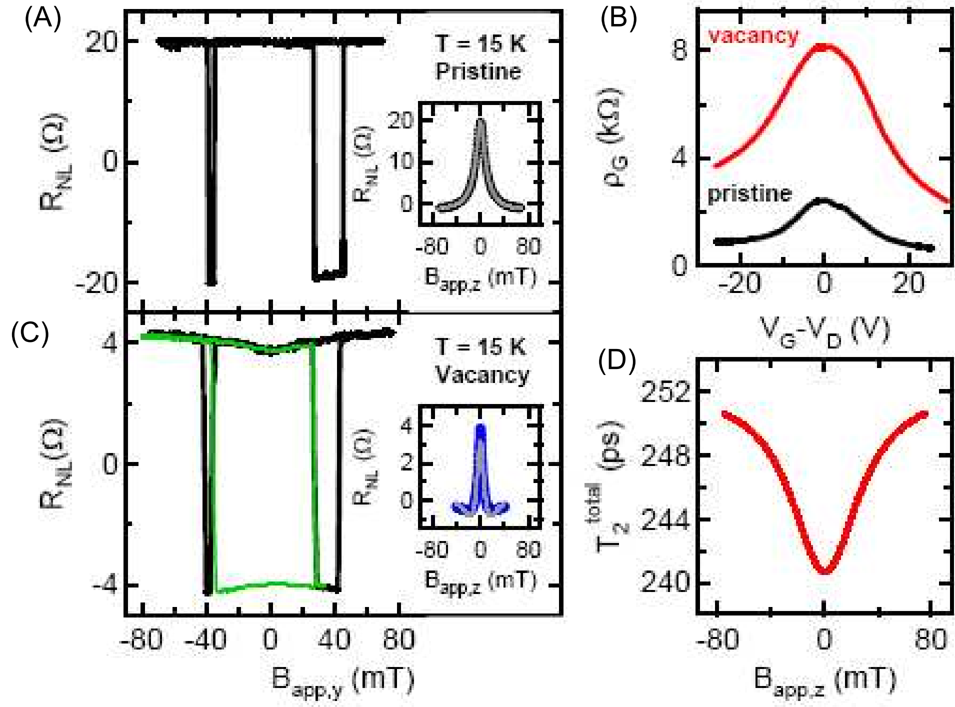

Fig 9-5 The effect of lattice vacancies on charge and spin transport in SLG at 15 K. (A) Non-local spin transport data in pristine graphene with R_{NL}=38.9 Ω. Hanle precession data (inset) yields values of τ^{so}= 859 ps and D=0.023 m^2/s. (B) Gate dependent ρ_G for pristine graphene (black) and following lattice vacancy formation via Ar-sputtering (red). (C) Non-local spin transport data in SLG containing vacancies. After Ar-sputtering, R_{NL} is decreased to 8.2 Ω and exhibits a dip at zero applied field. The minor loop (green) confirms the observed dip is a spin dependent effect, caused by paramagnetic moment formation. The best fit to the Hanle precession data (inset) yields ge*=5.86. (D) The field dependent T_2^{total} used to fit the Hanle data in (C).

presented in Fig. 9-5B displays ρ_G before (after) sputtering. After the introduction of vacancies, the resistivity is substantially increased and the mobility is reduced from 4945 cm^2/Vs to 949 cm^2/Vs. Ar-sputtering results in a large decrease in the magnitude of ΔR_{NL} as well as the emergence of a dip in R_{NL} at zero applied field (Fig. 9-5C). The minor loop, shown in green, indicates the observed dip is due to a decrease in the spin signal at low fields, signifying the formation of paramagnetic moments. The Hanle data (Fig. 9-5C inset) narrows following Ar-sputtering. The Hanle data combined with fitting the dip in

R_{NL} yields values of g_e*=5.86, ΔB = 13.9 mT, τ_c = 64.1 ps, and the field dependent T_2^{total} shown in Fig. 9-5D. Similar to hydrogen-doped graphene, the emergence of a dip in R_{NL} and narrowed Hanle curve following the introduction of lattice vacancies indicate the formation of paramagnetic moments in graphene.

9.3 Conclusion

The clear signatures of the presence of paramagnetic moments in both the non-local spin transport and Hanle precession data, which emerge only after exposure to atomic hydrogen or lattice vacancies, conclusively resolve the controversy regarding the possibility of magnetic moment formation in graphene. The novel spin relaxation technique introduced here provides a method to detect magnetism which is accessible to a broad range of scientists, and may be utilized in investigations of magnetic phenomena in graphene such as gate tunable magnetism, ferromagnetic ordering, edge-induced magnetism, and the Kondo effect.

References:

1. O. Yazyev, L. Helm, Defect-induced magnetism in graphene. *Phys. Rev. B* **75**, 125408 (2007).
2. D. W. Boukhvalov, M. I. Katsnelson, A. I. Lichtenstein, Hydrogen on graphene: Electronic structure, total energy, structural distortions and magnetism from first-principles calculations. *Phys. Rev. B* **77**, 035427 (2008).
3. J. Zhou *et al.*, Ferromagnetism in semihydrogenated graphene sheet. *Nano Lett.* **9**, 3867 (2009).
4. D. Soriano *et al.*, Magnetoresistance and magnetic ordering fingerprints in hydrogenated graphene. *Phys. Rev. Lett.* **107**, 016602 (2011).
5. B. Uchoa, V. N. Kotov, N. M. R. Peres, A. H. Castro Neto, Localized magnetic states in graphene. *Phys. Rev. Lett.* **101**, 026805 (2008).
6. M. A. H. Vozmediano, M. P. López-Sancho, T. Stauber, F. Guinea, Local defects and ferromagnetism in graphene layers. *Phys. Rev. B* **72**, 155121 (2005).
7. L. Pisani, J. A. Chan, B. Montanari, N. M. Harrison, Electronic structure and magnetic properties of graphitic ribbons. *Phys. Rev. B* **75**, 064418 (2007).
8. O. V. Yazyev, M. I. Katsnelson, Magnetic correlations at graphene edges: Basis for novel spintronics devices. *Phys. Rev. Lett.* **100**, 047209 (2008).
9. H. Lee, Y.-W. Son, N. Park, S. Han, J. Yu, Magnetic ordering at the edges of graphitic fragments: Magnetic tail interactions between the edge-localized states. *Phys. Rev. B* **72**, 174431 (2005).

10. R. R. Nair *et al.*, Spin-half paramagnetism in graphene induced by point defects. *Nat Phys*, doi: 10.1038/NPHYS2183 (2012).

11. O. Yazyev, Emergence of magnetism in graphene materials and nanostructures. *Rep. Prog. Phys.* **73**, 056501 (2010).

12. M. Sepioni *et al.*, Limits on intrinsic magnetism in graphene. *Phys. Rev. Lett.* **105**, 207205 (2010).

13. Y. Wang *et al.*, Room-temperature ferromagnetism of graphene. *Nano Lett.* **9**, 220 (2009).

14. H. S. S. Ramakrishna Matte, K. S. Subrahmanyam, C. N. R. Rao, Novel magnetic properties of graphene: Presence of both ferromagnetic and antiferromagnetic features and other aspects. *J. Phys. Chem. C* **113**, 9982 (2009).

15. L. Xie *et al.*, Room temperature ferromagnetism in partially hydrogenated epitaxial graphene. *Appl. Phys. Lett.* **98**, 193113 (2011).

16. P. Esquinazi *et al.*, Induced magnetic ordering by proton irradiation in graphite. *Phys. Rev. Lett.* **91**, 227201 (2003).

17. J. Cervenka, M. I. Katsnelson, C. F. J. Flipse, Room-temperature ferromagnetism in graphite driven by two-dimensional networks of point defects. *Nature Phys.* **5**, 840 (2009).

18. C. Tao *et al.*, Spatially resolving edge states of chiral graphene nanoribbons. *Nature Phys.* **7**, 616 (2011).

19. A. Candini, C. Alvino, W. Wernsdorfer, M. Affronte, Hysteresis loops of magnetoconductance in graphene devices. *Phys. Rev. B* **83**, 121401 (2011).

20. J.-H. Chen, L. Li, W. G. Cullen, E. D. Williams, M. S. Fuhrer, Tunable Kondo effect in graphene with defects. *Nature Phys.* **7**, 535 (2011).

21. X. Hong, S.-H. Cheng, C. Herding, J. Zhu, Colossal negative magnetoresistance in dilute fluorinated graphene. *Phys. Rev. B* **83**, 085410 (2011).

22. M. M. Ugeda, I. Brihuega, F. Guinea, J. M. Gómez-Rodríguez, Missing atom as a source of carbon magnetism. *Phys. Rev. Lett.* **104**, 096804 (2010).

23. Y.-W. Son, M. L. Cohen, S. G. Louie, Half-metallic graphene nanoribbons. *Nature* **444**, 347 (2006).

24. M. Johnson, R. H. Silsbee, Interfacial charge-spin coupling: injection and detection of spin magnetization in metals. *Phys. Rev. Lett.* **55**, 1790 (1985).

25. N. Tombros, C. Jozsa, M. Popinciuc, H. T. Jonkman, B. J. van Wees, Electronic spin transport and spin precession in single graphene layers at room temperature. *Nature* **448**, 571 (2007).

26. W. Han *et al.*, Spin transport and relaxation in graphene. *J. Magn. Magn. Mater.* **324**, 369 (2012).

27. K. Pi *et al.*, Electronic doping and scattering by transition metals on graphene. *Phys. Rev. B* **80**, 075406 (2009).

28. S. Takahashi, S. Maekawa, Spin injection and detection in magnetic nanostructures. *Phys. Rev. B* **67**, 052409 (2003).

29. W. Han *et al.*, Tunneling spin injection into single layer graphene. *Phys. Rev. Lett.* **105**, 167202 (2010).

30. J.-H. Chen, W. G. Cullen, C. Jang, M. S. Fuhrer, E. D. Williams, Defect scattering in graphene. *Phys. Rev. Lett.* **102**, 236805 (2009).

31. M. K. Chan *et al.*, Hyperfine interactions and spin transport in ferromagnet-semiconductor heterostructures. *Phys. Rev. B* **80**, 161206 (2009).

32. G. Salis, A. Fuhrer, S. F. Alvarado, Signatures of dynamically polarized nuclear spins in all-electrical lateral spin transport devices. *Phys. Rev. B* **80**, 115332 (2009).

33. T. D. Nguyen, Y. Sheng, M. Wohlgenannt, T. D. Anthopoulos, On the role of hydrogen in organic magnetoresistance: A study of C60 devices. *Synth. Met.* **157**, 930 (2007).

34. T. D. Nguyen *et al.*, Isotope effect in spin responce of pi-conjugated polymer films and devices. *Nature Mater.* **9**, 345 (2010).

35. D. Griffiths, *Introduction to quantum mechanics*. (Pearson Prentice Hall, Upper Saddle Riverer, NJ 07458, ed. 2, 2005).

36. J. Fabian, A. Matos-Abiague, C. Ertler, P. Stano, I. Zutic, Semiconductor spintronics. *Acta Phys. Slovaca* **57**, 565 (2007).

Appendix: Tight Binding Approximation

The tight binding approximation is a useful method to investigate electronic properties of materials when the atomic wavefunctions overlap enough so that the atoms can not be considered isolated, but at the same time the interaction is not so strong as to invalidate an atomic foundation. In the case of graphene, a nearest-neighbor tight binding model is very accurate at determining basic electronic properties, such as energy dispersion relation, and will be discussed in detail in the following.

The graphene lattice, as shown in Fig. A-1, is composed of a triangular bravais

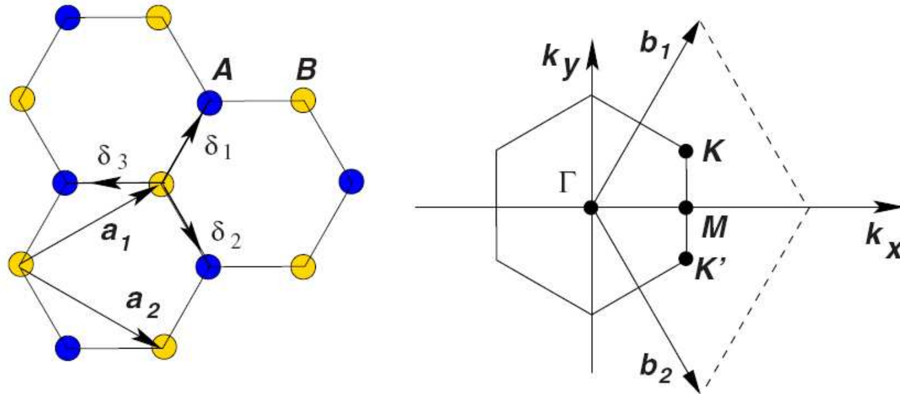

Fig A-1 The graphene lattice in real space and the first brilluion zone in reciprocal space

lattice containing a basis of 2 atoms in the unit cell (atoms A and B). The lattice vectors in real space are given by

$$\vec{a}_1 = \frac{a}{2}\left(3, \sqrt{3}\right) \quad \text{and} \quad \vec{a}_2 = \frac{a}{2}\left(3, -\sqrt{3}\right) \tag{A1}$$

The coefficient a= 1.42 Å is the distance between two neighboring carbon atoms. The nearest-neighbor vectors are given by

$$\vec{\delta}_1 = \frac{a}{2}\left(1, \sqrt{3}\right) \qquad \vec{\delta}_2 = \frac{a}{2}\left(1, -\sqrt{3}\right) \qquad \vec{\delta}_3 = a\left(-1, 0\right) \tag{A2}$$

The reciprocal lattice is also displayed in Fig A-1 The reciprocal lattice vectors must satisfy the relation $\vec{b}_i \cdot \vec{a}_j = 2\pi\delta_{ij}$ and are found to be

$$\vec{b}_1 = \frac{2\pi}{3a}\left(1, \sqrt{3}\right) \qquad b_2 = \frac{2\pi}{3a}\left(1, -\sqrt{3}\right) \tag{A3}$$

The K and K' points, positioned at the corners of the Brillouin zone, are referred to as the Dirac points. They are important in the derivation of the energy dispersion and will be discussed in more detail later. The Dirac points are located in reciprocal space at

$$\vec{K} = \left(\frac{2\pi}{3a}, \frac{2\pi}{3\sqrt{3}a}\right) \qquad \vec{K}' = \left(\frac{2\pi}{3a}, -\frac{2\pi}{3\sqrt{3}a}\right) \tag{A4}$$

To determine the Hamiltonian in the tight binding approximation, we first consider the Hamiltonian H_{at} of a single atom. Assuming the wavefunction is well localized around the atomic site, we will have

$$H_{at}\psi^i = E_i\psi^i \tag{A3}$$

This extreme case of isolated atoms must be modified to account for the interaction between electrons located on atoms of site A and B. The electrons can be viewed as "hopping" between nearest-neighbor sites. Higher order interactions can also be investigated in the tight-binding model, i.e. next-nearest neighbor hopping, but will not be derived here. The crystal Hamiltonian takes the form

$$H = H_{at} + \Delta U \tag{A4}$$

where the factor ΔU corrects the atomic potential in order to produce the full periodic potential of the graphene lattice. The eigenstate will be a linear combination atomic wavefunctions corresponding to the A and B sites

$$\Psi(\vec{r}) = c^A \psi^A(\vec{r}) + c^B \psi^B(\vec{r}) \tag{A5}$$

Using Bloch's theorem, this can also be written as

$$\Psi(\vec{r}) = \frac{1}{\sqrt{N}} \sum_j b^A(k) e^{i\vec{k}\cdot\vec{R}_j^A} \phi\left(\vec{r} - \vec{R}_j^A\right) + b^B(k) e^{i\vec{k}\cdot\vec{R}_j^B} \phi\left(\vec{r} - \vec{R}_j^B\right) \tag{A6}$$

where N is the number of unit cells.

Knowing that $H\Psi = E(k)\Psi$, evaluating $\left\langle \psi^A \middle| H \middle| \Psi \right\rangle$ and $\left\langle \psi^B \middle| H \middle| \Psi \right\rangle$ lead to the relations

$$c^A \left\langle \psi^A \middle| H \middle| \psi^A \right\rangle + c^B \left\langle \psi^A \middle| H \middle| \psi^B \right\rangle = E(k) c^A \left\langle \psi^A \middle| \psi^A \right\rangle + E(k) c^B \left\langle \psi^A \middle| \psi^B \right\rangle \tag{A7}$$

$$c^A \left\langle \psi^B \middle| H \middle| \psi^A \right\rangle + c^B \left\langle \psi^B \middle| H \middle| \psi^B \right\rangle = E(k) c^A \left\langle \psi^B \middle| \psi^A \right\rangle + E(k) c^B \left\langle \psi^B \middle| \psi^B \right\rangle \tag{A8}$$

The localized nature of ψ^A and ψ^B indicates the overlap matrices $\left\langle \psi^A \middle| \psi^B \right\rangle$ and $\left\langle \psi^B \middle| \psi^A \right\rangle$ will be small, and we neglect the contribution in this calculation. Additionally, $\left\langle \psi^A \middle| \psi^A \right\rangle = \left\langle \psi^B \middle| \psi^B \right\rangle = 1$ simplifying (A7) and (A8) to

$$c^A H_{AA} + c^B H_{AB} = E(k) c^A \tag{A9}$$

$$c^A H_{BA} + c^B H_{BB} = E(k) c^B \tag{A10}$$

where $H_{ij} \equiv \left\langle \psi^i \middle| H \middle| \psi^j \right\rangle$.

The elements H_{AA}=H_{BB}=E$_0$. To determine H_{AB} and H_{BA}, the form A6 is substituted, resulting in $\left\langle \psi^A \middle| H \middle| \psi^B \right\rangle = \left\langle \psi^B \middle| H \middle| \psi^A \right\rangle^* = \left(e^{i\vec{k}\cdot\vec{\delta}_1} + e^{i\vec{k}\cdot\vec{\delta}_2} + e^{i\vec{k}\cdot\vec{\delta}_3} \right) \left\langle \phi^A \middle| H \middle| \phi^B (\vec{r} - \vec{\delta}) \right\rangle$. The symmetry of the lattice and equidistance between the A and the 3 surrounding B sites indicates $\left\langle \phi^A \middle| H \middle| \phi^B (\vec{r} - \vec{\delta}) \right\rangle$ is the same for the three nearest-neighbor vectors. This transfer integral t= $\left\langle \psi^A \middle| H \middle| \psi^B (r - \delta) \right\rangle$ represents the nearest neighbor hopping energy, and has been found to be ≈2.8 eV in graphene. For simplicity, we define $f(k) = \left(e^{i\vec{k}\cdot\vec{\delta}_1} + e^{i\vec{k}\cdot\vec{\delta}_2} + e^{i\vec{k}\cdot\vec{\delta}_3} \right)$, allowing (A9) and (A10) to be written as.

$$c^A E_0 + c^B t f(k) = E(k) c^A \qquad \text{(A11)}$$

$$c^A t f(k)^* + c^B E_0 = E(k) c^B \qquad \text{(A12).}$$

In matrix from

$$\begin{pmatrix} E_0 - E(k) & t f(k) \\ t f(k)^* & E_0 - E(k) \end{pmatrix} \begin{pmatrix} c^A \\ c^B \end{pmatrix} = 0 \qquad \text{(A13)}$$

the determinant of the expression is easily evaluated

$$\left(E_0 - E(k) \right)^2 - t^2 \left| f(k) \right|^2 = 0 \qquad \text{(A14)}$$

$$E(k) = E_0 \pm t \left| f(k) \right| \qquad \text{(A15)}$$

Using the nearest neighbor vectors defined in (A2) and $\vec{k} = (k_x, k_y)$ we find

$$|f(k)| = \sqrt{\left(e^{i\vec{k}\cdot\vec{\delta}_1} + e^{i\vec{k}\cdot\vec{\delta}_2} + e^{i\vec{k}\cdot\vec{\delta}_3}\right)\left(e^{-i\vec{k}\cdot\vec{\delta}_1} + e^{-i\vec{k}\cdot\vec{\delta}_2} + e^{-i\vec{k}\cdot\vec{\delta}_3}\right)}$$

$$= \sqrt{3 + 2\cos\left(\sqrt{3}k_y a\right) + 4\cos\left(\frac{3}{2}k_x a\right)\cos\left(\frac{\sqrt{3}}{2}k_y a\right)} \qquad \text{(A16)}$$

Therefore the energy bands have the form

$$E(k) = E_0 \pm t\sqrt{3 + 2\cos\left(\sqrt{3}k_y a\right) + 4\cos\left(\frac{3}{2}k_x a\right)\cos\left(\frac{\sqrt{3}}{2}k_y a\right)} \qquad \text{(A17)}$$

with (+) corresponding to the π band and (-) the π* band. It is common to set E_0=0, as this term is independent of $\vec{k}$ and therefore provides an overall shift to both π and π* bands but does not affect of behavior. Simplifying in this way,

$$E(k) = \pm t\sqrt{3 + 2\cos\left(\sqrt{3}k_y a\right) + 4\cos\left(\frac{3}{2}k_x a\right)\cos\left(\frac{\sqrt{3}}{2}k_y a\right)} \qquad \text{(A18)}$$

Upon plugging the Dirac points into (A18), we find $E(k)$=0, indicating the energy bands meet at these particular points. Expanding about these points provides more information about the low energy relation near the Dirac points. By setting $\vec{k} = \vec{K} + \vec{q}$, for small $\vec{q}$ (i.e. $|\vec{q}| << |\vec{K}|$) we find

$$E(\vec{q}) = v_F|\vec{q}| \qquad \text{(A19)}$$

where $v_F = \frac{3ta}{2} \cong 1\times10^6$ m/s^2 and is referred to as the Fermi velocity.